6-19-2024

Copper-Based Electrocatalysts for Electrochemical Reduction of CO2 to C2 Products

Monsuru Olatunji Dauda
Louisiana State University

COPPER-BASED ELECTROCATALYSTS FOR ELECTROCHEMICAL REDUCTION OF CO_2 TO C_2 PRODUCTS

A Thesis

Submitted to the Graduate Faculty of the
Louisiana State University and
Agricultural and Mechanical College
in partial fulfillment of the
requirements for the degree of
Master of Science in Chemical Engineering

in

The Cain Department of Chemical Engineering

by
Monsuru Olatunji Dauda
B.Tech., Ladoke Akintola University of Technology, 2021
August 2024

ACKNOWLEDGMENTS

I am profoundly grateful to my advisor, Professor John Flake, for his invaluable mentorship, guidance, patience, and encouragement. I would also like to sincerely thank my group members, especially Mustapha Bello, John Hendershot, Junghyun Park, Ignace Agbadan and Soundarzo Tasnim for their extensive collaboration, thoughtful discussions, and willingness to share ideas that were crucial in shaping my own research directions and perspectives.

I wish to acknowledge Professor Plaisance and his research group for their assistance with DFT calculations, which provided critical mechanistic insights into my work. My thanks also go to Nicholas Lombardo for his exceptional design of the customized electrolyzer assembly utilized in my experiments. I am also thankful to Professor Orhan Kizilkaya and Professor Phillip Sprunger for generously lending their time and expertise to review and validate my datas, strengthening the quality of the analysis. Additionally, I am grateful to Professor Anthony Engler for his invaluable guidance, feedback, and recommendations during the writing of my manuscripts.

My research would not have been possible without the financial support from grants provided by the National Science Foundation (under Award Number 2119435) - their funding allowed me to fully pursue my graduate studies.

Finally, my deepest gratitude goes to my wife, friends and family for their unconditional love and support through this journey. This work is dedicated to them, as I could never have accomplished this monumental task without their unwavering faith in me.

TABLE OF CONTENTS

ABSTRACT

The electrochemical reduction of CO_2 using copper-based electrocatalysts has emerged as a promising approach for sustainable chemical production, offering a pathway to mitigate the rising atmospheric CO_2 levels while generating valuable fuels and chemicals. However, the selectivity and efficiency of copper-based catalysts towards specific C_2 products remain a major challenge, hindering their commercial viability. This thesis focuses on the development, characterization, and mechanistic understanding of three promising electrocatalyst systems for multi-carbon product generation from CO_2 reduction: copper-phosphide (Cu-P), copper-tin (Cu-Sn), and copper selenide (Cu_2Se). A comprehensive investigation of the electrocatalysts was conducted using advanced characterization techniques, including scanning electron microscopy (SEM), X-ray diffraction (XRD), X-ray photoelectron spectroscopy (XPS), and inductively coupled plasma optical emission spectrometry (ICP-OES). The electrochemical performance of the electrocatalysts was evaluated under various operating conditions in a zero-gap membrane electrode assembly (MEA) electrolyzer, which enables operation at industrially relevant current densities. The Cu-$P_{0.065}$ electrocatalyst demonstrated a remarkable enhancement in ethylene selectivity, achieving a Faradaic efficiency (FE) of 52% at a current density of 150 mA cm^{-2} in 0.1 M $KHCO_3$ electrolyte. The Cu-$Sn_{0.03}$ electrocatalyst exhibited a notable shift in selectivity towards ethanol, with an FE of 48% at 350 mA cm^{-2} in 1 M KOH electrolyte. The Cu_2Se electrocatalyst showcased a unique selectivity towards acetate production, achieving an FE of 32% at 350 mA cm^{-2} in 0.1 M $KHCO_3$ electrolyte, surpassing the performance of the pure Cu electrode and previously reported Cu-Se electrocatalysts. Durability studies revealed the stability of the electrocatalysts under prolonged CO_2 reduction conditions, with the Cu_2Se electrocatalyst demonstrating exceptional structural integrity. Thermodynamic considerations based on Pourbaix

diagrams highlighted the role of electronegative dopants in stabilizing the desired oxidation states of the electrocatalysts, contributing to their enhanced performance and stability. This thesis advances the understanding of CO_2 reduction mechanisms for multi-carbon products on Cu-based electrocatalysts and provides valuable insights into the rational design of efficient and selective electrocatalysts. The development of the Cu-$P_{0.065}$, Cu-$Sn_{0.03}$, and Cu_2Se electrocatalysts, with their remarkable selectivity, stability, and activity, represents a significant step forward in the field of electrochemical CO_2 reduction.

CHAPTER 1. INTRODUCTION

1.1. Motivation for sustainable Chemical Production through Electrocatalysis

Atmospheric CO_2 concentrations have increased by more than 50% relative to the preindustrial period (280 ppm) and drive acceleration of climate change. In December 2023, the concentration of atmospheric CO_2 concentration measured at Mauna Loa Observatory recorded at Mauna Loa, Hawaii was over 420 ppm (Figure 1.1), representing a record high over the last 650,000-800,000 years. (Boetcher et al., 2023; Lüthi et al., 2008; Neftel et al., 1988) Ice core and other proxy data suggest that current atmospheric CO_2 levels are the highest they have been in at least the past 14 million years.(Lüthi et al., 2008) That means the current climate represents a stark contrast to the environment that human societies developed in, and prolonging this trajectory risks disruptive impacts across natural and human systems worldwide.

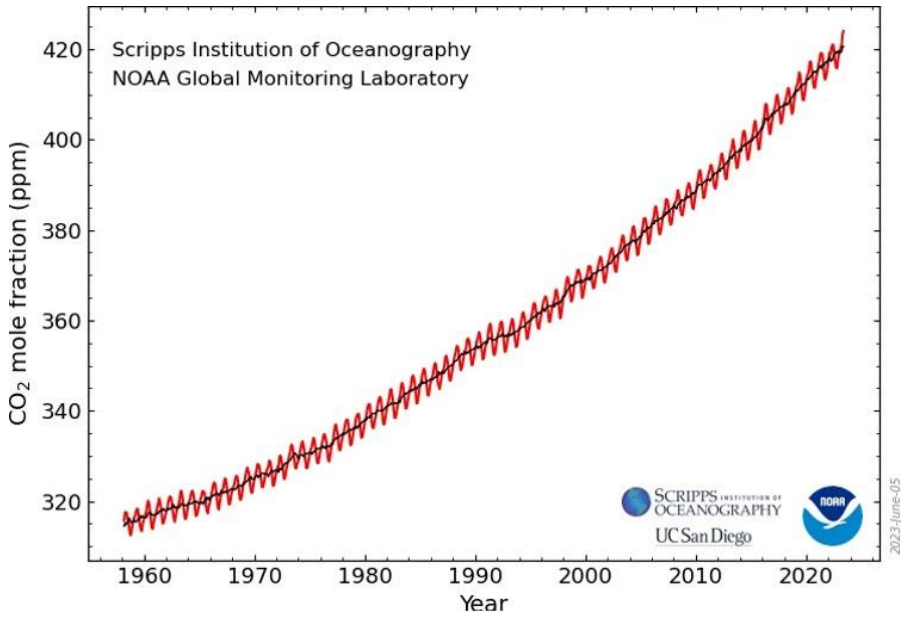

Figure 1.1. Atmospheric CO_2 concentrations from 1960 to present. The red curve represents monthly mean data, while the black curve represents the seasonally corrected data. All the data was measured at Mauna Loa Observatory, Hawaii.(Us Department of Commerce)

Although much CO_2 comes from burning fossil fuels for transport and power, chemical manufacturing, including production of carbon-based chemicals (such as ethylene, ethanol and

acetate), is responsible for approximately 2 billion metric tons of CO_2 per year (~ 5% of global emissions). (Gabrielli et al., 2023) Depending on future emissions and production processes, atmospheric CO_2 may surpass 800 ppm by 2100 (Figure 1.2).(Consortium*† et al., 2023; Fontela et al., 2020) Using CO_2 as a feedstock with renewable energy can sustainably produce carbon products with zero or negative emissions.

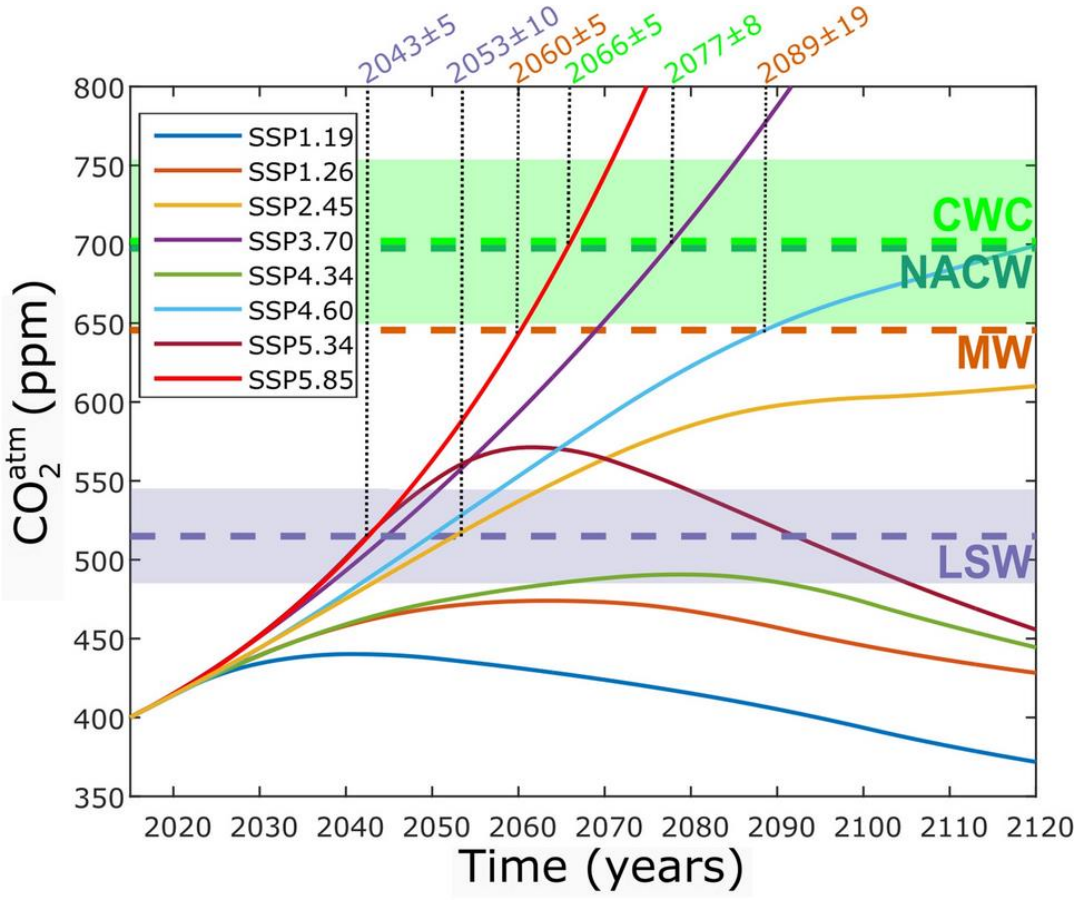

Figure 1.2. Projections of atmospheric CO_2 concentration (ppm) versus time (years) as modelled by the eight Shared Socioeconomic pathways (SSPs) considered. (Fontela et al., 2020)

Electrochemically converting CO_2 into fuels and chemicals using renewable electricity is a promising emissions mitigation strategy. In electrolysis cells, CO_2 is reduced to hydrocarbons and oxygenates at the cathode, while water is oxidized to oxygen at the anode, separated by ion-conducting membranes. This allows selective production of chemicals like formate, CO, ethanol,

ethylene, and acetate.(Dauda et al., 2024; Gabardo et al., 2019; Jeng et al., 2022; Lu et al., 2022; Merino-Garcia et al., 2019; Xiang et al., 2019; Xie et al., 2022; Zhang et al., 2019) Early CO_2 reduction studies by Hori et al. (Hori et al., 1989) in H-cells with aqueous 0.1 M $KHCO_3$ electrolyte (pH 8.5, 5 mA cm^{-2}) revealed distinct product distributions among metal electrodes Pb, Hg, Tl, In, Sn, Cd and Bi primarily produce formate; Au, Ag, Zn, Pd nd Ga mainly generate CO; Ni, Fe, Pt and Ti predominantly reduce water to H_2. Notably, Cu is the only pure metal that produces hydrocarbons and alcohols, primarily methane.

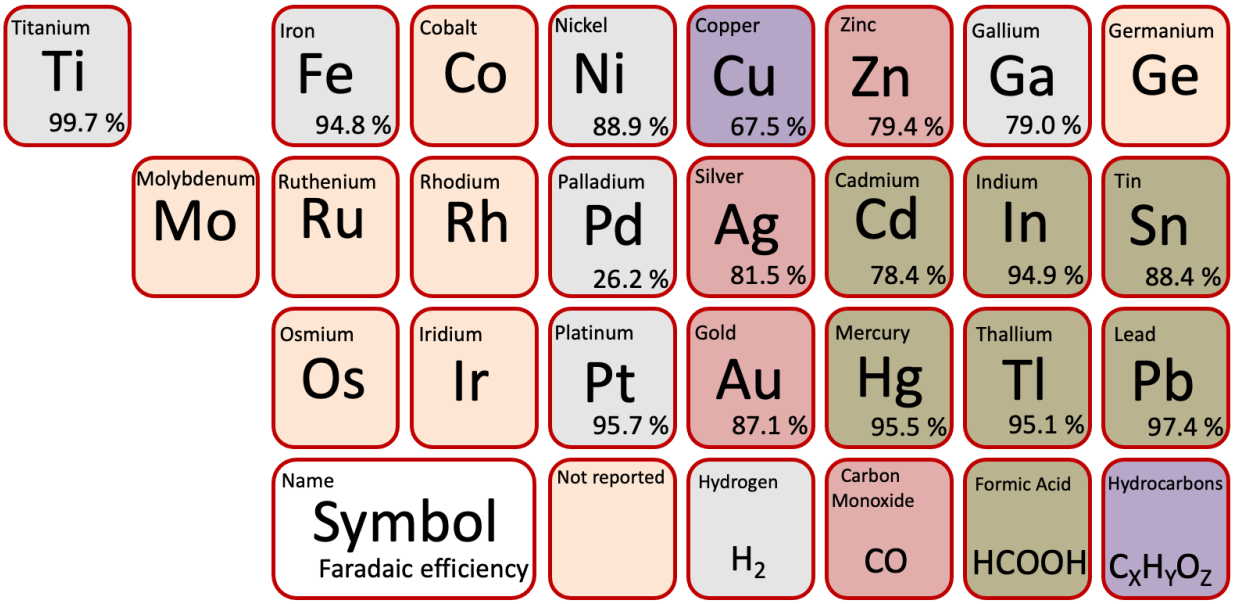

Figure 1.3. Faradaic efficiencies for major products from CO_2 reduction reaction experiments in aqueous solution using various metal electrodes.

H-type cells have limitations for CO_2 reduction due to low CO_2 solubility (~34 mM at 25°C (Carroll et al., 1991)) and slow diffusion kinetics (diffusion coefficient D =0.00194 mm^2s^{-1} at 25°C (Tamimi et al., 1994)). Recent advances using gas diffusion electrodes (GDE) and anion exchange membranes (AEMs) have overcome these issues by enabling the use of alkaline electrolytes like KOH. This suppresses the hydrogen evolution reaction (HER), and ethylene becomes the main CO_2 reduction product at copper electrocatalysts in alkaline solutions. (Gabardo

et al., 2019; Jeng et al., 2022; Xie et al., 2022) However, liquid electrolytes increase resistance and reduce energy efficiency. Eliminating them between electrodes can achieve current densities (up to 1 Acm^{-2}) and cell voltages suitable for industrial applications.(Z. Zhang et al., 2023) Membrane electrode assemblies (MEAs), or zero-gap electrolyzers, feature a sandwich structure with a polymer electrolyte membrane directly between the cathode and anode. This design promotes higher energy efficiency and allows for assembly into CO_2 electrolyzer stacks for industrially relevant processes.(Dauda et al., 2024; Jeng et al., 2022; Sassenburg et al., 2023; Wei et al., 2020; Weng et al., 2019)

Advancing CO_2 electrolysis to commercial viability requires meeting key criteria: high current densities and energetic efficiencies for cost-effective scale-up; high Faradaic and single-pass conversions to maximize product selectivity and yield while minimizing separation costs; high product concentrations to further control separation expenses; and high long-term stability for sustained reliable operation.(Álvarez-Gómez & Varela, 2023; Nwabara et al., 2020) Developing a high-performance CO_2 electrolyzer that simultaneously exhibits efficient and selective electrocatalysts while meeting all desired properties presents a significant challenge, requiring the overcoming of complex hurdles in system CO_2 reduction. This study aims to investigate the performance of Cu-based alloy electrocatalysts, synthesized using similar "one-pot" methods, under identical reaction conditions in a zero-gap MEA cell setup. It will explore the mechanisms governing the selective formation of ethylene, ethanol, or acetate based on the degree of partial positive charge ($\delta+$) of Cu reaction sites, examining how the partial positive charge on the surface of copper atoms influences the process of multi-carbon product formation.

1.2. Overview

Sustainable chemical production through the electrochemical reduction of CO_2 using copper-based electrocatalysts has emerged as a promising approach to address the global challenge of rising atmospheric CO_2 levels while producing valuable fuels and chemicals. This thesis focuses on the development and characterization of three promising electrocatalyst systems for multi-carbon product generation from CO_2 reduction: copper-phosphide (Cu-P), copper-tin (Cu-Sn), and copper selenide (Cu_2Se). The study aims to gain a comprehensive understanding of the CO_2 reduction mechanisms for multi-carbon products at the molecular level, with a focus on developing electrocatalysts with enhanced selectivity and yields.

Chapter 1 introduces the motivation for sustainable chemical production through electrocatalysis, highlighting the potential of electrochemical CO_2 reduction to mitigate greenhouse gas emissions and produce industrially relevant chemicals. It provides an overview of the current state of the technology and the challenges that need to be addressed for commercial viability. Chapter 2 presents a literature review on electrochemical CO_2 conversion, covering the various pathways, electrolyzers, and electrocatalysts employed in the process. It discusses the advantages and limitations of different cell configurations and highlights the unique ability of copper-based catalysts to generate multi-carbon products. Chapter 3 describes the experimental methods used in this study, including the synthesis and characterization techniques for the electrocatalysts, the design of the electrolyzer, and the product determination methods. The use of a zero-gap membrane electrode assembly (MEA) electrolyzer is emphasized for its ability to operate at industrially relevant current densities.

Chapters 4, 5, and 6 focus on the reduction of CO_2 at copper-phosphorus, copper-tin, and copper-selenide surfaces, respectively. Each chapter presents a comprehensive characterization of

the electrocatalysts using advanced techniques such as scanning electron microscopy (SEM), X-ray diffraction (XRD), X-ray photoelectron spectroscopy (XPS), and inductively coupled plasma optical emission spectrometry (ICP-OES). The electrochemical performance of the electrocatalysts is evaluated under various operating conditions, and the impact of heteroatom incorporation on the catalytic activity and selectivity is discussed. Comparisons with previously reported electrocatalysts are made to highlight the advancements achieved in this work. Chapter 7 investigates the durability of the Cu-P, Cu-Sn, and Cu_2Se electrocatalysts under prolonged CO_2 reduction conditions. The stability measurements, including electrochemical performance, morphological changes, and oxidation state evolution, are analyzed using advanced characterization techniques. Thermodynamic considerations based on Pourbaix diagrams are presented to elucidate the role of electronegative dopants in stabilizing the desired oxidation states of the electrocatalysts.

In summary, this thesis presents a multifaceted approach to the development and understanding of Cu-based electrocatalysts for efficient and selective CO_2 reduction to multi-carbon products. The insights gained from the experimental and computational studies contribute to the advancement of sustainable chemical production through electrocatalysis and pave the way for the practical implementation of this promising technology.

CHAPTER 2. LITERATURE REVIEW

2.1. Electrochemical CO_2 Conversion

Electrochemical CO_2 reduction research dates back several decades, with pioneering work by Hori et al. in the 1980s providing crucial insights into the influence of electrolyte nature, electrode material, and applied potential on CO_2 reduction. (Hori, 2008; Hori et al., 1989; Hori et al., 1987; Hori et al., 2003) The process involves applying a potential between two electrodes in an aqueous electrolyte. At the anode, water is oxidized to O_2 via the oxygen evolution reaction (OER).(Liu et al., 2017; Nitopi et al., 2019)The electrons and protons from the OER are consumed at the cathode through CO_2 reduction to various carbon-based products, competing with the hydrogen evolution reaction (HER). (Albo et al., 2015; Álvarez-Gómez & Varela, 2023; Chang et al., 2022; Ni et al., 2021; Nwabara et al., 2020; Zheng et al., 2019) The prevailing reaction pathway is highly dependent on the electrocatalyst material. Table 1.1 presents the cathode reactions for major CO_2 reduction products, including the associated number of electrons needed (z) and standard cell potential (E_0) versus reversible hydrogen electrode (RHE). Applying a tailored electrocatalyst allows the cathode product distribution between HER, formate, CO, and more energy dense C_{2+} species. Optimizing selectivity, stability, and activity remains an area requiring further research for commercially viable CO_2 electrolysis.(Ding et al., 2023; Y. Li et al., 2023; Ni et al., 2021; Timoshenko et al., 2022)

Table 2.1. CO_2 reduction products, required electrons, and reaction equations under acidic and alkaline conditions

Product	Formula		Acidic Conditions		Alkaline Conditions	
		Z	Equation	E (V vs SHE)	Equation	E(V vs SHE)
Hydrogen	H_2	2	$2H^+ + 2e^- \rightarrow H_2$	0	$2H_2O + 2e^- \rightarrow H2 + 2OH^-$	-0.828
Formic Acid	HCOOH	2	$CO_2 + 2H^+ + 2e^- \rightarrow HCOOH$	-0.171	$CO_2 + H_2O + 2e^- \rightarrow HCOO + OH^-$	-0.639
Carbon Monoxide	CO	2	$CO_2 + 2H^+ + 2e^- \rightarrow CO + H_2O$	-0.104	$CO_2 + H_2O + 2e^- \rightarrow CO + 2OH^-$	-0.932
Methanol	CH_3OH	6	$CO_2 + 6H^+ + 6e^- \rightarrow CH_3OH + H_2O$	0.016	$CO_2 + 5H_2O + 6e^- \rightarrow CH_3OH + 6OH^-$	-0.812
Methane	CH_4	8	$CO_2 + 8H^+ + 8e^- \rightarrow CH_4 + 2H_2O$	0.169	$CO_2 + 6H_2O + 8e^- \rightarrow CH_4 + 8OH^-$	-0.659
Acetic Acid	CH_3COOH	8	$2CO_2 + 8H^+ + 8e^- \rightarrow CH_3COOH + 2H_2O$	0.098	$2CO_2 + 5H_2O + 8e^- \rightarrow CH_3COO^- + 7OH^-$	-0.653
Ethanol	C_2H_5OH	12	$2CO_2 + 12H^+ + 12e^- \rightarrow C_2H_5OH + 3H_2O$	0.084	$2CO_2 + 9H_2O + 12e^- \rightarrow C_2H_5OH + 12OH^-$	-0.744
Ethylene	C_2H_4	12	$2CO_2 + 12H^+ + 12e^- \rightarrow C_2H_4 + 4H_2O$	0.085	$2CO_2 + 8H_2O + 12e^- \rightarrow C_2H_4 + 12OH^-$	-0.743
Ethane	C_2H_6	14	$2CO_2 + 14H^+ + 14e^- \rightarrow C_2H_6 + 4H_2O$	0.144	$2CO_2 + 10H_2O + 14e^- \rightarrow C_2H_6 + 14OH^-$	-0.685
Propanol	C_3H_7OH	18	$3CO_2 + 18H^+ + 18e^- \rightarrow C_3H_7OH + 5H_2O$	0.095	$3CO_2 + 13H_2O + 18e^- \rightarrow C_3H_7OH + 18OH^-$	-0.733
Oxygen	O_2	4	$2H_2O \quad 4H^+ + O_2 + 4e^-$	1.23	$4OH^- \rightarrow H_2O + O_2 + 4e^-$	0.401

Wang et al.(J. Wang et al., 2021) demonstrated that both the activity and selectivity of Cu electrocatalysts can be modified by introducing electropositive $Cu^{\delta+}$ sites through electronative dopants, while electronegative dopants enhance CO* intermediate stability. Incorporating dopants like B, N, and P into Cu catalysts enhances selectivity for C_{2+} products like ethylene by modulating the Cu lattice to form and stabilize $Cu^{\delta+}$ species that promote C-C coupling. (Chen et al., 2021; Kong et al., 2021; Liang et al., 2018; Yin et al., 2019; Zhou et al., 2018) By creating electropositive $Cu^{\delta+}$ reaction sites and promoting reactions with OH^-, the selectivity can shift from ethylene to ethanol. The presence of OH^- species at the Cu^+ boundary could induce attractive electrostatic interactions between surface-OH dipole and the dipole of carbonyl group of hydrocarbon intermediates, leading to the blocking of hydrogenation of coupled intermediates and preferential ethanol formation. (Chang et al., 2022; Karapinar et al., 2021; J. Wang et al., 2021; Zheng et al., 2019) More electronegative dopants in Cu lead to the formation of oxygenates, including acetate. Proposed mechanisms suggest Cu^+ species stabilize a ketene intermediate (ethenone) that yields either ethanol or acetate.(H. Wang et al., 2023; Zheng et al., 2019) In recent years, CO_2 reduction has garnered significant attention, with research spanning various areas including theoretical computational studies, fundamental mechanistic investigations, electrocatalyst development, and electrolyzer system design.

2.2. Electrolyzers

2.2.1. Cell Configuration

Realizing viable large-scale CO_2 electrolysis requires optimizing the electrochemical cell architecture to address inherent performance tradeoffs. CO_2 electrolyzers consist of key components such as a working electrode, counter electrode, electrolyte, and ion-exchange

membrane (IEM) that partitions the device into cathode and anode chambers.(Ge et al., 2022; Küngas, 2020; Sassenburg et al., 2023; Weng et al., 2019; Xiang & Jin, 2023; Zhang et al., 2018; Zheng et al., 2019) Comparing results between different research groups requires carefully considering the specifics of the electrolyzer setup used. The diverse CO_2 electrolyzer structures, arising from variations in gas mass transfer and electrolyte flow transport, profoundly impact performance metrics. Analyzing the structural features of different CO_2 electrolyzers and advancing their engineering design is crucial for scaling up applications while ensuring optimal performance. Several commonly employed CO_2 electrolyzer setups exist, each with distinct advantages and limitations.

One-compartment cells offer the simplest design but lack separation between cathodic and anodic regions, leading to product re-oxidation and electrode contamination. (Álvarez-Gómez & Varela, 2023; Chen et al., 2023; Ding et al., 2023) H-cells (Figure 2.1a) provide divided cathode and anode half-cells separated by an IEM, making them preferred in lab-scale CO_2 electrolysis. However, they suffer from low dissolved CO_2 concentrations, large interelectrode distances, and low selectivity at higher overpotentials. (Gawel et al., 2022; Liang et al., 2020; Lin et al., 2023; Xuan et al., 2020; Yu et al., 2019)

Flow cells (Figure 2.1b) employ gas diffusion electrodes (GDEs) to overcome CO_2 mass transfer limitations. The working electrode features a porous carbon fiber gas diffusion layer (GDL) coated with electrocatalyst materials, separated by an IEM.(Chen et al., 2020; Ma et al., 2014; Ma et al., 2014; Ma et al., 2016; Tornow et al., 2012; Whipple et al., 2010)Flow cells enhance CO_2 mass transfer and boost CO_2 concentration on the WE surface, enabling industrial-grade current density and electroreduction performance. However, preventing GDE flooding by

electrolyte infiltration remains a challenge. (Lees et al., 2022; Ma et al., 2021; Nitopi et al., 2019; Overa et al., 2022; Park et al., 2012; Z. Wang et al., 2023; Weekes et al., 2018; Yu et al., 2019)

Membrane electrode assemblies (MEAs) (Figure 2.1c) solve the electrolyte flooding issue by pressing GDEs on either side of an ion-conducting membrane, eliminating liquid catholyte and reducing electrolyte resistance. (Overa et al., 2022; Romiluyi et al., 2023; Weng et al., 2019) This design allows for industrially relevant current densities (> 1A cm^{-2}) while preserving selective CO_2 conversion.(García de Arquer et al., 2020; Jeng et al., 2022; Sassenburg et al., 2023; Weng et al., 2019) A modified MEA cell with a solid electrolyte channel has been used to address carbonate precipitation in alkaline MEAs and low Faradaic efficiency in acidic MEAs. (Lin et al., 2023)

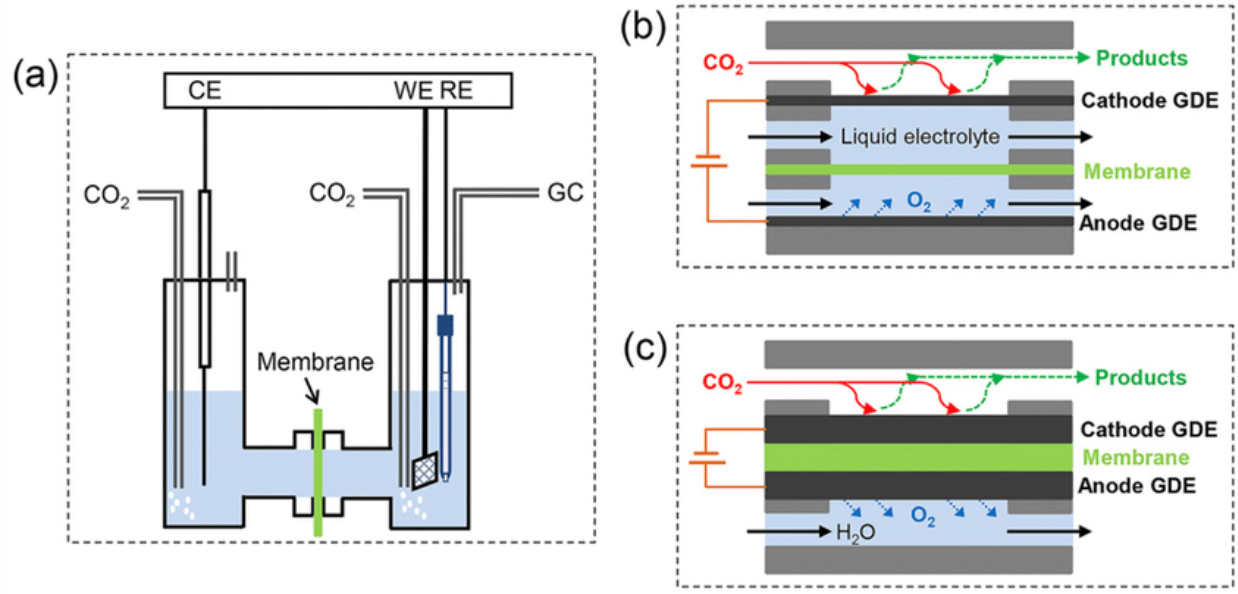

Figure 2.1. Schematic diagrams of different electrochemical cell used in CO_2RR (a) H-Cell; (b) Flow cell electrolyzer; (c) MEA electrolyzer; (Diagram inspiration from (Gao et al., 2021))

2.2.2. Components of membrane electrode assemblies

2.2.2.1. GDE composition and structure

Gas diffusion electrodes (GDEs) are a key component in membrane electrode assemblies (MEAs) for CO_2 electrocatalytic reduction. GDEs consist of a porous gas diffusion layer (GDL)

with an immobilized cathode catalyst layer. The electrocatalyst layer and its local microenvironment determine the products formed (discussed in section 2.3). Carbon-based GDLs, either single macroporous or dual-layer with a microporous layer, support the electrocatalyst and facilitate gas transport.(Baumgartner et al., 2022; Wakerley et al., 2022; Wood et al., 2006)Novel porous polytetrafluoroethylene (PTFE)-based GDLs have also shown excellent performance.(Dinh et al., 2018; Gabardo et al., 2019; García de Arquer et al., 2020; Higgins et al., 2019)

GDE performance relies on CO_2 permeability, crucial for reactant transport and avoiding HER dominance. Optimization involves factors like hydrophobicity, catalyst layer thickness, and structural parameters. Kim et al. (Kim et al., 2016) demonstrated that adjusting PTFE concentration in the microporous layer optimizes hydrophobicity, with 20 wt% PTFE achieving the best performance. Tan et al.(Tan et al., 2020) found that controlling electrocatalyst layer thickness modulates local CO_2 concentration, favoring C_{2+} chemical production. Vermaas et al.(Baumgartner et al., 2022) investigated GDE structural parameters, including substrate structure, thickness, and cracks, which influence the flow-by pressure window and catalytic performance

Optimizing GDEs is vital for high-performance CO2 reduction in MEAs. Key factors include GDL composition, microporous layer hydrophobicity, catalyst layer thickness, and structural parameters. Understanding these factors' influence on mass transport and reactions is crucial for efficient GDE design in CO_2 electrocatalysis.

2.2.2.2. Ion exchange membranes

MEAs for CO_2 reduction rely on specific ion exchange membranes to facilitate efficient ion transport and prevent electron crossover. These membranes' performance is determined by

parameters like ion exchange capacity, conductivity, water uptake, and mechanical strength, shaping the local reaction environment, including pH and reactant concentration.(Hasa et al., 2023; Salvatore et al., 2021; Ziv et al., 2018). Several types of membranes have been developed for CO_2 reduction in MEA electrolyzers, including cation exchange membranes (CEMs), anion exchange membranes (AEMs), bipolar membranes (BPMs) with reverse bias, and BPMs with forward bias. Additionally, solid polymer electrolytes have shown promise as membranes in MEA electrolyzers for CO_2 reduction applications.(Petrov et al., 2022; Salvatore et al., 2021; Weekes et al., 2018)

CEMs like Nafion™ are widely used in CO_2 reduction due to their high proton conductivity, reducing system losses. However, they can promote acidic conditions at the cathode, potentially favoring HER over product selectivity. (Habibzadeh et al., 2023; Weekes et al., 2018) To address this issue, a permeable CO_2 regeneration layer (PCRL) can be used to shield the cathode from protons and promote CO_2 regeneration from carbonate. This approach has been shown to achieve similar product distributions to AEM electrolyzers and enable high single-pass CO_2 conversion.(O'Brien et al., 2021) Huang et al. functionalized the Cu catalyst surface with a cationic perfluorosulfonic acid ionomer, which exchanges protons with K^+ from the catholyte, creating a high local K^+ concentration and slowing OH^- diffusion, thus facilitating C-C coupling. However, unintended cation crossover can be problematic in CEMs.(Huang et al., 2021)

AEMs, like Sustainion®, QAPPT, and PiperION, have been used in MEA electrolyzers.(Gawel et al., 2022) Sustainion® X37-50 offers low area-specific resistance and stability in alkaline conditions, making it popular among researchers. QAPPT membranes exhibit high OH^- conductivity and stability, while PiperION membranes have high carbonate-ion conductivity.(Habibzadeh et al., 2023; Salvatore et al., 2021; Wierzbicki et al., 2020; Zhang et al.) For example, Kutz et al. (Kutz et al., 2017) achieved a notable milestone in continuous CO_2

electrocatalysis, utilizing an MEA-based electrolyzer with high-performance Sustainion membranes. With an Ag cathode and IrO_2 anode, they achieved 95% Faradaic efficiency for CO at 50 mA cm^{-2} for 6 months (4380 hours), and >90% FE at 200 mA cm^{-2} for 1000 hours, with the incorporation of ionomer into the cathode catalyst layer. Sargent and colleagues demonstrated ~50% Faradaic efficiency for ethylene with a Cu GDE cathode and AEM, maintaining stable cell voltages for over 100 hours of continuous operation (Gabardo et al., 2019) with secondary products including ethanol (15% FE) and acetate (7% FE). Despite their advantages, AEMs face challenges like CO_2 consumption by hydroxide, cation diffusion leading to precipitate formation, CO_2 feed loss, and membrane degradation.(Wierzbicki et al., 2020) AEMs are commonly utilized for CO_2 reduction due to their ability to transport anions from cathode to anode. The strongly alkaline environment can degrade the cationic groups and polymer backbone of the membrane, while also inhibiting the HER by reducing H^+ concentration at the cathode interface. AEMs also encounter difficulties including the loss of CO_2 feed caused by the transfer of carbonate/bicarbonate from the cathode to the anode, as well as membrane degradation.(Alerte et al., 2021; Habibzadeh et al., 2023; McCallum et al., 2021; Sassenburg et al., 2023; Zhang et al.)

BPMs offer an alternative approach comprising a cation exchange layer and an anion exchange layer, present promising alternatives to overcome the limitations of both CEMs and AEMs.(Habibzadeh et al., 2023; Vermaas & Smith, 2016) Operating in reverse bias mode, BPMs can maintain distinct pH conditions at the cathode and anode, thereby minimizing carbonate formation and product crossover. (Li et al., 2018) However, they often incur higher voltage losses due to water dissociation at the membrane interface and may experience mechanical degradation and delamination. Xie et al. developed a CO_2 electrolyzer incorporating a bipolar membrane (BPM) with a stationary catholyte layer (SC-layer) to achieve high single-pass CO_2 utilization and

conversion to multicarbon products. The BPM architecture, comprising a cation exchange layer (CEL) and an anion exchange layer (AEL) with Cu nanoparticle at the cathode, demonstrated effective CO_2 crossover prevention. Notably, the SC-BPM electrolyzer achieved 78% single-pass CO2 utilization, outperforming conventional limits. It exhibited operational stability over 50 hours at 200 mA cm^{-2}, highlighting its potential for sustainable CO_2 electroreduction.(Xie et al., 2022)

The selection of ion exchange membranes plays a critical role in determining the performance and efficiency of MEA electrolyzers for CO_2 reduction. Each type - AEMs, CEMs, and BPMs - presents distinct advantages and challenges, with the choice dependent on factors such as the desired reaction environment, product distribution, and overall system performance. Ongoing research and development in membrane materials and architectures are vital for furthering the commercial viability of MEA electrolyzers in CO_2 reduction applications.

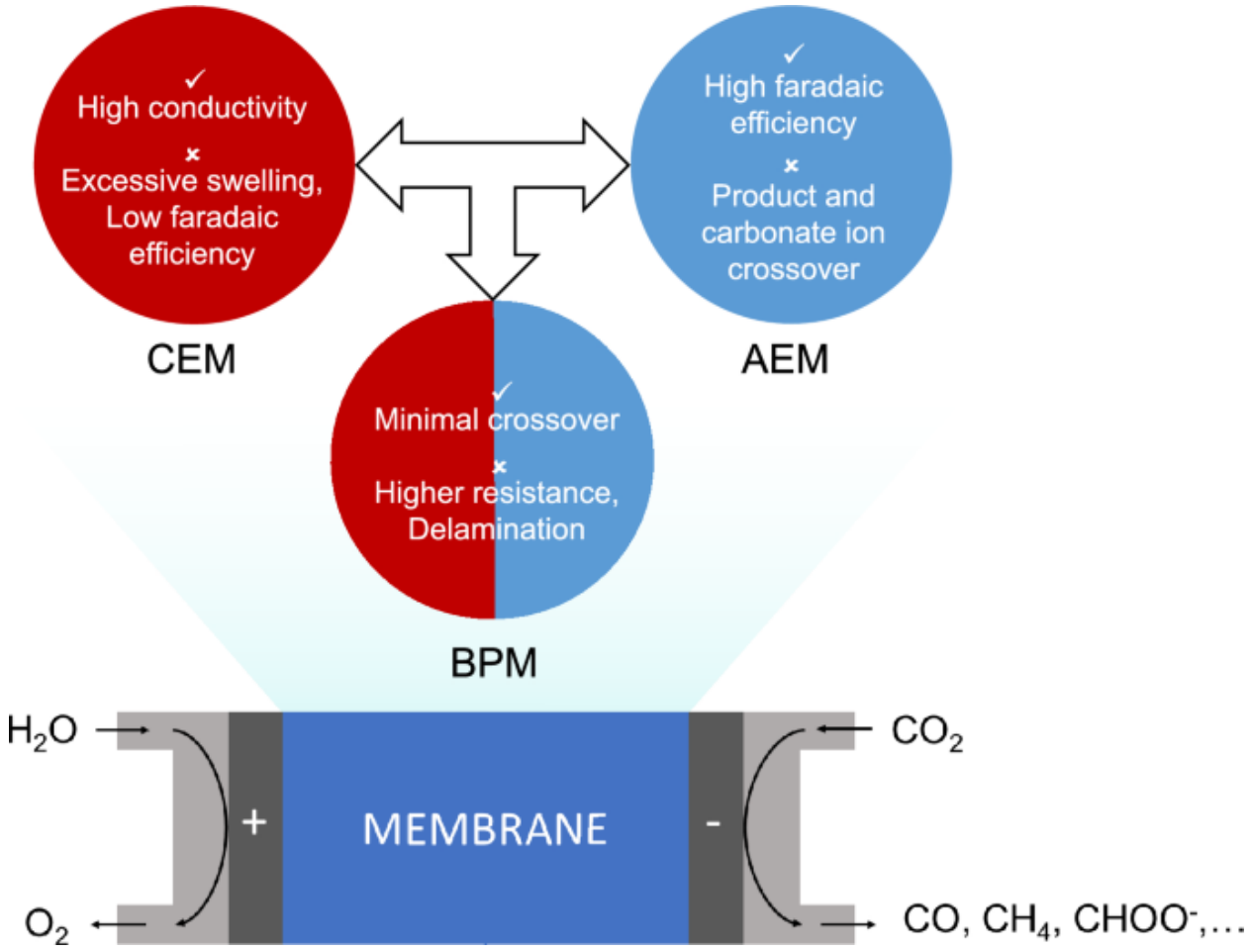

Figure 2.2. Membranes (Habibzadeh et al., 2023)

2.3. Electrocatalysts

Metal electrodes such as Cu, Au, and Sn have been extensively studied for their ability to catalyze the electrochemical reduction of CO_2.(Barcelos et al., 2024; Zhang et al., 2018) These metals can be grouped based on how they interact with key reaction intermediates, which influences the products formed. (Barcelos et al., 2024; Jones et al., 2014) The first group (Pb, Hg, Tl, In, Sn, Cd, Bi) mainly produces formate or formic acid due to weak intermediate binding. The second group (Au, Ag, Zn, Pd, Ga) binds certain intermediates strongly but releases CO easily, leading to its predominant formation. Competitive HER occurs on Pt, Ti, Fe, and Ni. Tuning binding energies is crucial for selectivity and efficiency. Cu uniquely converts CO intermediates

into valuable hydrocarbons and alcohols, making it the sole metal efficient in producing such high-value products from CO2.(Feaster et al., 2017; Hori et al., 1985; Hori et al., 1989; Roduner, 2014; Schouten et al., 2012; Yang et al., 2023)

Despite its unique electronic properties, Cu faces intrinsic limitations due to scaling relations between binding energies of reaction intermediates on metallic surfaces, resulting in broad product distributions and unwanted hydrogen evolution. Achieving selective CO2 reduction to industrially significant C_{2+} species remains a persistent challenge, but introducing a second metal into copper-based catalysts addresses issues of slow reaction kinetics, low selectivity, and poor stability associated with single metallic Cu electrocatalysts.(Chen et al., 2021; Liu et al., 2017; Nitopi et al., 2019) Various methods have been explored to enhance the efficiency of CO2 electroreduction on copper, including controlling morphology,(Wang et al., 2019) modifying the surface,(Jiang et al., 2020) utilizing oxide-derived copper,(Lum et al., 2017; Mandal et al., 2018; X. Wang et al., 2021) incorporating single atoms,(Xia et al., 2023; H. Yang et al., 2019) doping with heteroatoms(Chen et al., 2021; Kong et al., 2021; Liang et al., 2018; Yin et al., 2019; Zhou et al., 2018) and employing copper-based bimetallic electrocatalysts.(Kim et al., 2014)

Early observations by Lee's group indicated that during cathodic CO_2 reduction, the presence of a Cu_2O layer on the catalyst surface enhanced the selectivity for C_2H_4 production compared to metallic Cu electrodes.(Kim et al., 2015; Lee et al., 2015) This highlighted the crucial role of $Cu^{\delta+}$ in guiding the CO_2 reduction pathway towards efficient C_{2+} product generation.(Wu et al., 2021; Zhang et al., 2020) Although it is generally believed that Cu^+ species on oxide-derived Cu catalysts are easily reduced to metallic Cu under cathodic potentials according, a significant portion of these Cu^+ species has been found to be surprisingly resistant to electrochemical reduction during CO_2 reduction.(Mistry et al., 2016) In situ X-ray absorption spectroscopy (XAS) measurements on an

O_2-plasma-activated Cu catalyst during CO_2 reduction revealed that Cu^+ species could persist for at least 15 minutes at -1.2 V vs. RHE. The initial 84% Cu^+ on the surface decreased to 77% after 10 minutes and 23% after 1 hour at the same potential, highlighting the unexpected stability of these oxidized species under reducing conditions.(De Luna et al., 2018) However, the instability of $Cu^{\delta+}$ active sites during CO_2 reduction and their susceptibility to in situ self-reduction present challenges in maintaining high CO_2 reduction activity, particularly under high current densities.(Fang et al., 2023)

To address this issue, researchers have made significant progress by introducing nonmetal heteroatoms such as P,(Chen et al., 2021; Kong et al., 2021; Li et al., 2019) B,(Chen et al., 2018; J.-S. Wang et al., 2021) S,(Zhuang et al., 2018) and N(Karapinar et al., 2019; Liang et al., 2018) to modify the electronic structure of copper surfaces and fine-tune their binding strength. The doping strategy takes advantage of the different electronegativities of the dopants compared to copper (Cu: 1.9). Gallium (Ga: 1.81), boron (B: 2.04), sulfur (S: 2.58), and nitrogen (N: 3.04) are among the dopants considered.

CHAPTER 3. GENERAL EXPERIMENTAL METHODS

3.1. Chemicals and Materials

Copper chloride dihydrate ($CuCl_2 \cdot 2H_2O$, 99%), selenium powder (Se, 99.5%), stannous chloride ($SnCl_2$, 98%), potassium bicarbonate ($KHCO_3$, 99%), potassium hydroxide (KOH, 99.95%), sodium hydroxide (NaOH), hydrazine hydrate aqueous solution ($N_2H_4 \cdot H_2O$, 85%), and hydrochloric acid (36–38%) were all procured from ThermoFisher Scientific. Sodium hypophosphite (NaH_2PO_2, 99%) and iridium (IV) chloride hydrate ($IrCl_4 \cdot XH_2O$, 99.9%) were obtained from Sinopharm Chemical Reagent Co., Ltd. Sodium hypophosphite serves as a reducing agent in the synthesis of nanoparticles, while iridium (IV) chloride hydrate is a precursor for the preparation of iridium-based catalysts. In addition to the chemical reagents, several specialized materials were purchased from Fuel Cell Store. These materials include Sustainion membranes (X37-50 Grade RT), which have a dry thickness of above 50 microns. Carbon black vulcan, a conductive carbon material, titanium (Ti) felt and polyvinylidene fluoride (PVDF) with a pore size of 0.45 μm, which serves as a binder in electrode fabrication, were also sourced from Fuel Cell Store. All deionized (DI) water used in the experiments was of Milli-Q grade, with a resistivity of 18.2 MΩ·cm, ensuring that the water was free from ionic impurities that could interfere with the synthesis or electrochemical measurements.

3.2. Electrolyzer Design

The experiments were conducted using a custom-made MEA electrolyzer cell designed to optimize CO_2 transport and allow for adjustable clamping pressure on the anode and cathode end plates. The cathode flow field, made from 2205 stainless steel, features a serpentine flow channel (3.33 mm wide, 0.2 mm deep) to promote efficient CO_2 transport across the gas diffusion electrode

(GDE). The anode flow field, milled from grade 2 titanium, has a serpentine flow channel (0.79 mm wide and deep) to facilitate electrolyte flow and maintain consistent mass transport. The key feature is the ability to independently adjust the clamping pressure on the anode and cathode end plates, allowing for the removal of gaskets and the use of varying anode/cathode thicknesses, providing flexibility in cell configuration, and optimizing the membrane and electrode stack sealing.

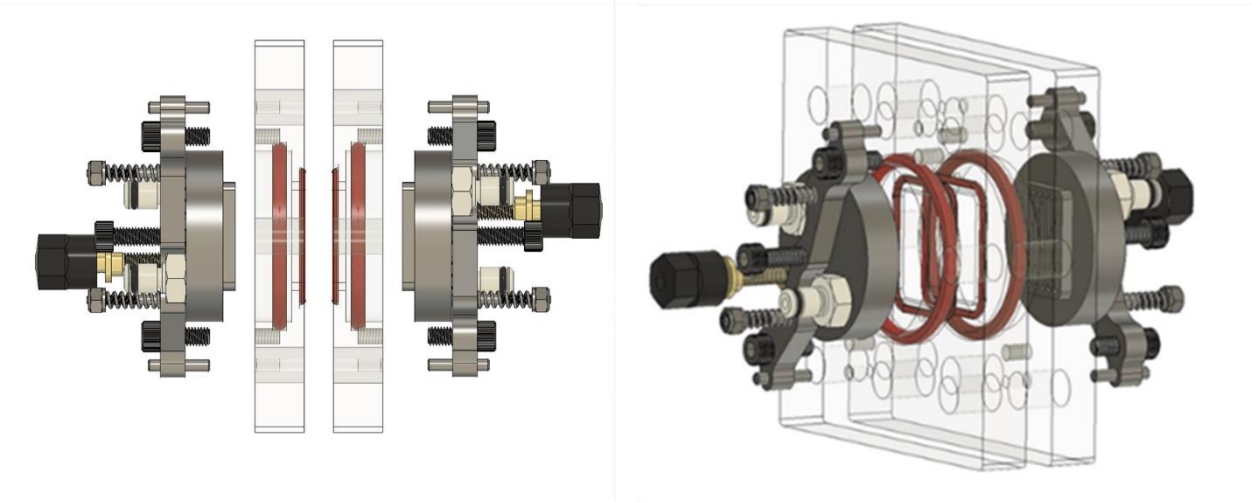

Figure 3.1. 3D CAD drawing of electrolyzer, side view (left); CAD drawing of electrolyzer, isometric view (right); (CAD drawings courtesy of Nicholas Lombardo)

3.3. Electrolyzer Testing

During the experiments, CO_2 was supplied to the cathode side of the electrolyzer at a flow rate of 20 sccm, while an aqueous 0.1 M $KHCO_3$ electrolyte was fed to the anode at a flow rate of 10 mL min-1 using a peristaltic pump (CHEM-TECH). The flow rates of both the cathode and anode were precisely controlled and monitored using mass flow controllers (Alicat MC-500SCCM) and Flow Vision 2.0 software, ensuring consistent and accurate control of the reactant and electrolyte flow throughout the experiments. The electrolyzer was powered by a constant current supplied via a 30V/5A DC power supply (Triplett), and the cell potential was logged using

a voltage data logger (MadgeTech Volt101). To mitigate the potential effects of liquid product accumulation on the system's performance, the anolyte was not recycled. Dry CO_2 (Airgas) flow to the electrolyzer was maintained using a mass flow controller (Alicat MC-500SCCM), while an altered model of the same mass flow controller maintained a backpressure of 110.32 kPa (16 psia) on the cathode of the reactor. The outlet flow rate of the reactor was monitored using a mass flow meter (Alicat M-500SCCM). Figure 3.3 provides a schematic representation of the electrolyzer testing setup. To evaluate the performance of the electrolyzer and the selectivity of the catalysts, Faradaic efficiencies were determined based on the outlet flow rates and product concentrations. Gas chromatography (GC) and nuclear magnetic resonance (NMR) analyses were employed to quantify the gaseous and liquid products, respectively. The GC and NMR instruments were calibrated to ensure accurate measurements of the product concentrations. The use of a zero-gap configuration in the MEA electrolyzer cell minimizes the distance between the cathode and anode, reducing ohmic losses and improving the overall performance of the electrolyzer.

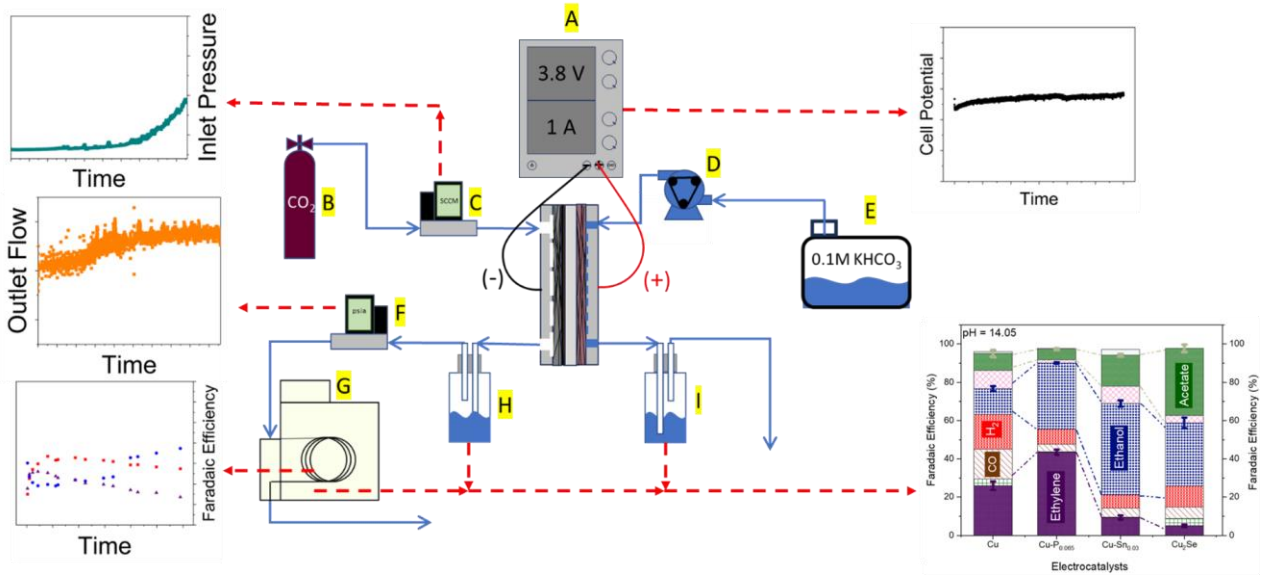

Figure 3.2. The equipment used for MEA electrolyzer testing includes: A) Power supply and loggers for measurements B) CO_2 cylinder C) Mass flow controller for CO flow and pressure D) Peristaltic pump for electrolyte flow E) Electrolyte reservoir F) Backpressure control unit for cathode pressure and flow rate G) In-line gas chromatograph for gas products H) Liquid trap for cathode outlet products I) Liquid trap for anode outlet products

3.4. Product Determination

The CO_2 reduction reaction gas products were analyzed using gas chromatography. The gas samples were directly injected into a Shimadzu gas chromatograph (GC-2030) equipped with a twelve-stream inlet port and auto-injector, as well as thermal conductivity and flame ionization detectors. The gas chromatograph was further equipped with a Molecular Sieve 5A Capillary Column and a packed Carboxen-1000 Column, with Helium used as the carrier gas. To determine the Faradaic Efficiency (FE) of each gas product, Equation (1) was used:

$$FE_i = x_i \times \frac{P_o V}{RT} \times \frac{Z_i F}{I_{Total}} \times 100\%. \qquad (1)$$

Where $\mathbf{x_i}$ is the volume fraction of the gas product **i, V** is the outlet gas flow rate in m^3s^{-1}, $\mathbf{P_o}$ is atmosphere pressure 101.325 kPa**, R** is the ideal gas constant 8.314 J mol^{-1} K^{-1}, T is

temperature in **K, Z_i**is the number of electrons required to produce one molecule of product F is Faraday's Constant 96485 C mol^{-1}, and $\mathbf{I_{Total}}$ is the total current in A.

Liquid products were collected from both the anode and cathode sides of the MEA. At the cathode, liquid collection was achieved by bubbling the CO_2 through a 50 mL midget bubbler containing 10 mL of deionized water in an ice bath maintained at 0 °C. The quantification of liquid products was carried out using proton nuclear magnetic resonance spectroscopy (^{1}H-NMR) on an Agilent DD2 500 spectrometer or a Bruker 400 NMR spectrometer in a mixture of 90% H_2O and 10% D_2O using water suppression mode. Dimethyl sulfoxide (DMSO) was used as the internal standard. Fresh anolyte was used for each plot of liquid product quantification, and the duration of the collection was set at 30 minutes. To calculate the Faradaic Efficiency (FE) of each liquid product, Equation (2) was used:

$$FE_i = n_i \times \frac{Z_i F}{I_{Total} t} \times 100\% \qquad (2)$$

Where $\mathbf{n_i}$ i is the quantity of the liquid product **i** in mole, **t** is the duration of product collection.

CHAPTER 4. REDUCTION OF CO_2 AT COPPER-PHOSPHORUS SURFACES

4.1. Introduction

The electrochemical reduction of CO_2 is a promising approach to mitigate greenhouse gas emissions and produce valuable chemicals. Cu has demonstrated unique capabilities in facilitating the formation of multi-carbon products.(Nitopi et al., 2019) Recent works in electrochemical CO_2 reduction have leveraged Cu electrocatalysts, gas diffusion electrodes (GDE) and anion exchange membranes (AEMs), in zero-gap membrane electrode assembly (MEA) cell configurations, with ethylene commonly reported as the primary CO_2 reduction products when using alkaline anolytes.(Gabardo et al., 2019; Jeng et al., 2022; Xie et al., 2022) However, the selectivity and efficiency of Cu electrocatalysts towards desired products, such as C_{2+} hydrocarbons and oxygenates, remain challenging. Oxide-derived copper electrocatalysts in gas diffusion electrode (GDE) architectures have shown improved C_2 product selectivity, but prolonged exposure to reducing potentials leads to their transformation into pure Cu, resulting in performance degradation. (Kim et al., 2015; Lee et al., 2015; Mistry et al., 2016; Wu et al., 2021; Zhang et al., 2020).

Researchers have explored doping Cu with metalloid components such as Cu-B,(Chen et al., 2018) Cu-S,(Deng et al., 2018; Phillips et al., 2018) and Cu-N,(Liang et al., 2018) to modify its electronic structure and surface properties. Phosphorus-doped copper electrocatalysts have garnered attention for their potential in enhancing CO_2 reduction performance. The variance in electronegativity between P (2.19) and Cu (1.9) facilitates the creation of favorable $Cu^{\delta+}$ sites upon P-doping, crucial for promoting C−C coupling reactions and forming multi-carbon products such as ethylene (C_2H_4) and ethanol (C_2H_5OH).(Chen et al., 2021) P-doping has also demonstrated effectiveness in suppressing the competing hydrogen evolution reaction (HER).

Several studies have investigated the performance of phosphorus-doped copper electrocatalysts for CO_2 reduction. Chen et al.(Chen et al., 2021) achieved a Faradaic efficiency (FE) of 44.9% for ethylene on a $P_{0.075}$-Cu catalyst at -1.6 V vs. RHE. Kong et al (Kong et al., 2021) evaluated CO2 reduction in a flow cell using Cu electrocatalyst with 8.3% P, exhibiting a twofold increase in ethylene FE (25% to 46%) and a threefold increase in ethanol FE (5% to 15%) compared to undoped Cu at 210 mA cm^{-2} in 1 M KOH electrolyte. This study addresses a notable research gap by examining the application of phosphorus-doped copper electrocatalysts in CO_2 reduction. By harnessing the distinctive electronic and structural characteristics facilitated by phosphorus integration, the aim is to improve selectivity, efficiency, and stability in generating valuable C_{2+} products within Zero-gap MEA electrolyzer.

4.2. Experimental

4.2.1. Synthesis of electrocatalyst

The synthesis of copper-phosphorus (Cu-$P_{0.065}$) nanoparticles with a molar ratio of 1:0.065 was carried out using a one-pot approach. $CuCl_2 \cdot 2H_2O$ was dissolved in deionized water with poly(vinylpyrrolidone) (PVP) as a stabilizing agent. The pH was adjusted using NaOH, and the mixture was stirred at 80 °C for 2 hours. NaH_2PO_2 solution was then added as the phosphorus source, followed by $N_2H_4 \cdot H_2O$ as a reducing agent. The reaction mixture was heated and stirred for an additional 3 hours. The synthesized Cu-$P_{0.065}$ nanoparticles were collected by centrifugation, washed with deionized water, ethanol, and acetone, and finally dried at 60 °C for 12 hours. This comprehensive synthesis approach ensures the formation of high-quality Cu-$P_{0.065}$ nanoparticles with the desired composition and properties for further applications.

4.2.2. Characterization

Crystal structures of the synthesized Cu-$P_{0.065}$ nanoparticles were analyzed using a PANanalytical X-ray diffractometer (XRD) operating at 40 kV and 40 mA. Data collection was performed from 20° to 100° angles, and the obtained XRD patterns were compared with standard reference data to determine phase composition and crystallinity. The average crystallite size was calculated using the Scherrer equation.

X-ray photoelectron spectroscopy (XPS) analysis was conducted using a ScientaOmicron XPS system to study the surface elemental composition and oxidation states of the nanoparticles. XPS measurements were performed under ultra-high vacuum conditions, and the obtained spectra were analyzed to determine the atomic percentages of copper and phosphorus on the surface. High-resolution XPS scans of the Cu 2p and P 2p regions were conducted to investigate the oxidation states and bonding characteristics.

The morphology and grain size information of the Cu-$P_{0.065}$ nanoparticles were examined using a field emission scanning electron microscope (SEM) equipped with an energy dispersive X-ray spectrometer (EDS). The ThermoFisher PFIBSEM system provided high-resolution imaging of the nanoparticle morphology, including shape, size distribution, and surface features. SEM-EDS analysis provided information about the elemental composition and spatial distribution of copper and phosphorus within the nanoparticles, confirming homogeneous incorporation of phosphorus throughout the material.

4.2.3. Electrode preparation

The cathode electrode, consisting of the synthesized Cu-$P_{0.065}$ electrocatalyst, was fabricated using a spray-coating technique. The electrocatalyst slurry was prepared by mixing approximately 100 mg of Cu-$P_{0.065}$ nanoparticles, 5 mg of Vulcan Carbon, and 5.53 mg of polyvinylidene fluoride

(PVDF) powder in 20 mL of a 1:1 H_2O-isopropanol solution. The mixture was subjected to sonication for 1 hour to ensure a homogeneous dispersion of the components, resulting in a stable and well-mixed electrocatalyst ink. The prepared slurry was then sprayed onto a 50 cm^2 microporous hydrophobic side of a gas diffusion carbon paper (Sigracet 39BB) using a Sonaer Inc. NS130K/130KHz Ultrasonic Atomizer Nozzle and Sonaer Inc. Atomizer Ultrasonic Generator. The atomizer nozzle was supplied with electrocatalyst ink at a controlled rate of 20 mL hour-1 using a Masterflex syringe pump and a 10 mL syringe. The gas flow to the nozzle was provided by an airbrush pump with an outlet flow pressure of 6.89 kPa (1 psig), ensuring a fine and uniform spray pattern. During the spray-coating process, the Sigracet 39BB was securely taped by the edges to a hot plate maintained at 100 ºC, with the microporous layer facing outward. The applied heat facilitated the evaporation of H_2O and isopropanol, preventing the ink from bleeding or pooling on the gas diffusion electrode (GDE) surface. The spray-coating was performed in a tight serpentine pattern to achieve an even distribution of the electrocatalyst layer. The coating process was continued until an electrocatalyst loading of 1 mg cm^{-2} was achieved, which was precisely determined by weighing the GDE before and after the coating process.

The anode electrode was prepared by dip-coating iridium chloride onto a titanium felt substrate, followed by thermal decomposition to form a stable and active IrO_2 catalyst layer. Prior to the coating process, the titanium felt, covering an area of 6.64 cm^2, was etched in boiling 0.5 M oxalic acid for 30 minutes. This etching step aimed to increase the surface area of the titanium felt and improve the adhesion of the subsequent catalyst layer. After etching, the titanium felt was thoroughly rinsed with deionized water and dried. The pretreated titanium felt was then dip-coated in a solution containing 75 mg of $IrCl_4 \cdot xH_2O$ dissolved in 6.76 ml of 37% HCl and 18.24 ml of isopropanol. The dip-coating process ensured a uniform coverage of the iridium precursor on the

titanium felt surface. Following the dip-coating step, the coated titanium felt was dried in an oven at 100 °C for 20 minutes to remove the solvent and allow for the initial formation of the catalyst layer. Subsequently, the dried titanium felt was subjected to calcination at 500 °C for 20 minutes in an air atmosphere. During this high-temperature treatment, the $IrCl_4$ precursor underwent thermal decomposition, resulting in the formation of a stable and active IrO_2 catalyst layer on the titanium felt surface. To achieve the desired catalyst loading of 3 mg cm^{-2}, the dipping, drying, and calcination process was repeated multiple times, with careful monitoring of the mass gain after each cycle.

Before assembling the MEA electrolyzer cell, the Cu-$P_{0.065}$ cathode was left overnight at room temperature to ensure complete drying, while the IrO_2 anode was allowed to cool down after the final calcination step. The conditioned electrodes were carefully assembled into the custom-made MEA electrolyzer cell, ensuring precise alignment and proper contact. The cell was sealed using an adjustable clamping pressure feature, which allowed for optimal sealing without additional gaskets, promoting excellent electrical contact and minimizing ohmic losses. The well-sealed and conditioned MEA electrolyzer cell was then ready for electrochemical CO_2 reduction experiments.

4.3. Results

4.3.1. Electrocatalyst characterization

4.3.1.1. Scanning Electron Microscope (SEM)

To investigate the morphology, size, and elemental composition of the synthesized Cu-$P_{0.065}$ nanoparticles, a scanning electron microscope (SEM) equipped with an energy dispersive X-ray spectrometer (EDS) was employed. The SEM image in Figure 4.1a reveals the presence of spherical nanoparticles with diameters near 100 nm, similar to the undoped Cu electrocatalyst. The spherical morphology and uniform size distribution can be attributed to the controlled nucleation

and growth processes facilitated by the one-pot synthesis method, which employs hydrazine as a reducing agent and PVP as a capping agent.

EDS elemental mapping was performed to gain insights into the elemental composition and distribution within the Cu-$P_{0.065}$ nanoparticles. Figures 4.1b and 4.1c present the EDS elemental maps of copper and phosphorus, respectively, revealing a uniform distribution of both elements throughout the nanoparticles. This indicates the homogeneous incorporation of phosphorus into the copper lattice, suggesting the formation of a true alloy structure with phosphorus atoms substituting copper atoms in the lattice.

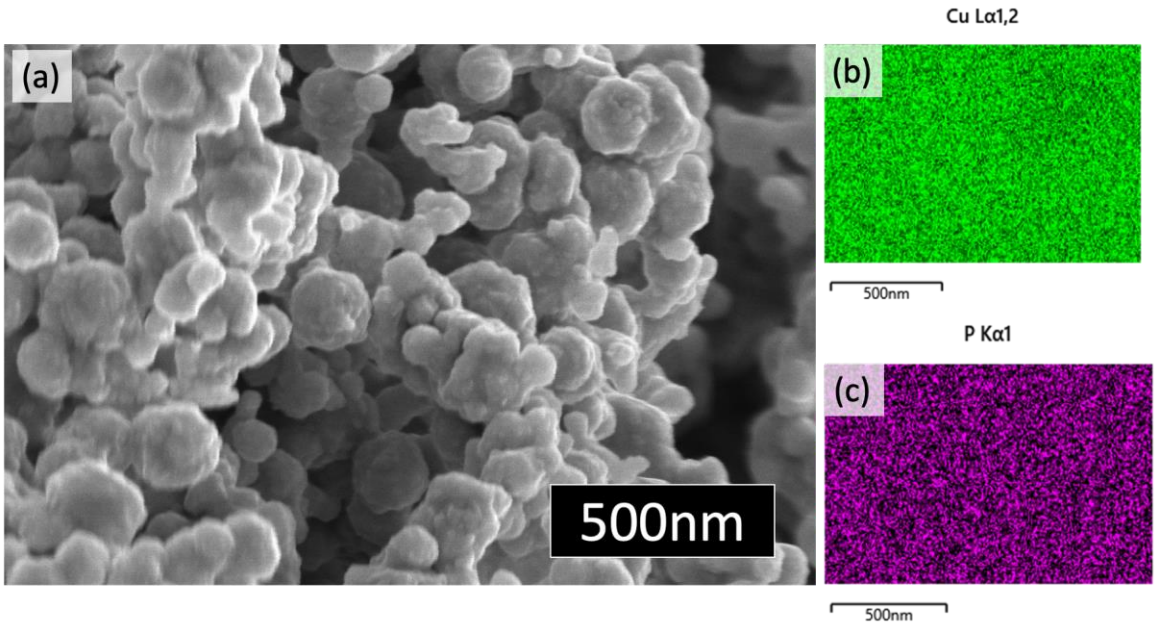

Figure 4.1. (a) Scanning electron microscopy (SEM) images of the synthesized Cu-$P_{0.065}$ with 100 nm average particle size. (b) Energy dispersive X-ray spectroscopy (EDS) elemental mapping of Cu (c) Energy dispersive X-ray spectroscopy (EDS) elemental mapping of P

4.3.1.2. X-ray diffraction (XRD) Analysis

X-ray diffraction (XRD) is a powerful technique for investigating the crystal structure, phase composition, and lattice parameters of materials. In this study, XRD analyses were conducted to examine the structural phases of the Cu-$P_{0.065}$ electrocatalyst before and after its use in the

electrochemical reduction of CO_2. Figure 4.3a presents the XRD patterns of the Cu-$P_{0.065}$ electrocatalyst and undoped Cu, revealing the impact of phosphorus incorporation on the crystal structure of Cu. Both the Cu-$P_{0.065}$ electrocatalyst and undoped Cu exhibited characteristic peaks corresponding to the (111), (200), (220), (311), and (222) planes of face-centered cubic (fcc) Cu, confirming the primary crystalline phase of the material. However, a closer inspection of the XRD patterns reveals subtle differences between the two samples, particularly in the peak positions.

A notable observation from the XRD analysis is the shift of the characteristic Cu peaks to lower 2θ values in the Cu-$P_{0.065}$ electrocatalyst compared to undoped Cu. This shift indicates an expansion of the Cu crystal lattice upon the incorporation of phosphorus atoms.(Chen et al., 2021; Kong et al., 2021) The lattice expansion can be attributed to the larger atomic radius of phosphorus compared to copper, which induces a distortion in the crystal structure when phosphorus atoms substitute copper atoms in the lattice. To better visualize this shift, Figure 4.3b provides a zoomed-in view of the (111) and (200) peaks, clearly demonstrating the displacement of the peaks towards lower 2θ values in the Cu-$P_{0.065}$ electrocatalyst. The gradual peak displacements and increased interplanar spacings (d-spacings) with increasing phosphorus content confirm a monotonic increase in the Cu-Cu interatomic distances, further supporting the lattice expansion induced by phosphorus incorporation.

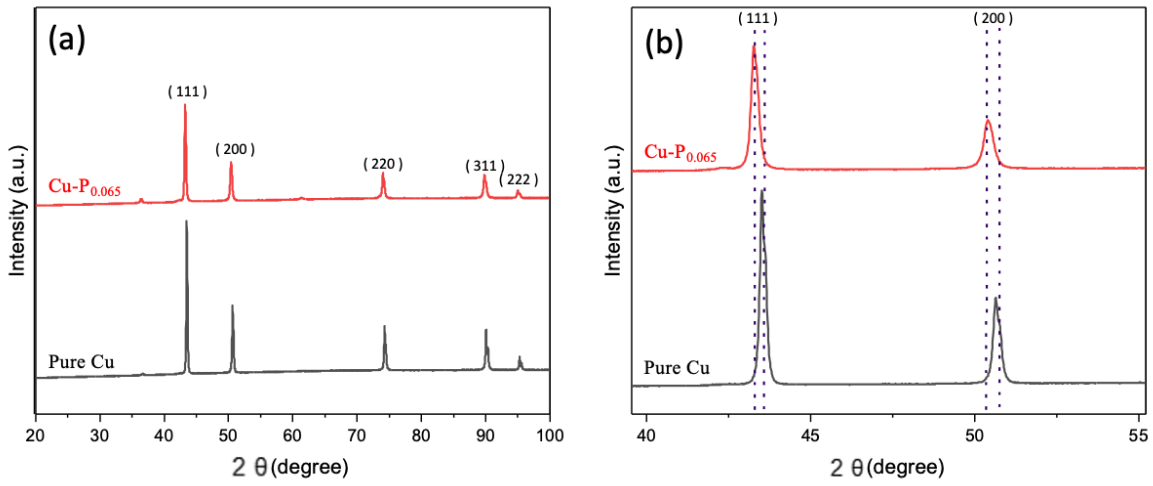

Figure 4.2. (a) XRD pattern of Cu and Cu-$P_{0.065}$ showing shifted peaks to lower 2θ values for Cu-$P_{0.065}$. (b) Zoom-in of the (111) and (200) peaks.

4.3.1.3. X-ray Photoelectron Spectroscopy (XPS) Analysis

X-ray photoelectron spectroscopy (XPS) is a powerful surface-sensitive technique that provides valuable information about the electronic structure, oxidation states, and chemical composition of materials. In this study, XPS analyses were conducted to investigate the electronic properties of the Cu-$P_{0.065}$ electrocatalyst and gain insights into the oxidation states of the Cu species and the presence of phosphorus. Figure 4.4(a) presents the XPS survey spectrum of the synthesized Cu-$P_{0.065}$ electrocatalyst, which provides an overview of the elements present on the surface of the material. The survey spectrum confirms the presence of Cu and P, along with other elements such as O and C, which may arise from surface adsorption, or the presence of the capping agent used during the synthesis.

To further elucidate the oxidation states of the Cu species in the Cu-$P_{0.065}$ electrocatalyst, high-resolution XPS spectra of the Cu 2p region were acquired. As shown in Figure 4.4(b), the Cu 2p core photoemission levels for all samples resided at near 932 eV (Cu 2p3/2) and 952 eV (Cu 2p1/2) binding energies, which are characteristic of Cu oxidation states. The Cu 2p3/2 core levels of the

Cu-$P_{0.065}$ electrocatalyst were deconvoluted into two peaks: one corresponding to the ~932 eV Cu^0/Cu^+ states, which differ by less than 0.2 eV in binding energy (only distinguished by inspecting their respective Cu LLM Auger parameter), and a second shoulder peak at ~934 eV corresponding to the Cu^{2+} oxidation state.

To confirm the successful incorporation of phosphorus into the Cu lattice, high-resolution XPS spectra of the P 2p region were collected. Figure 4.4(c) presents the XPS P 2p spectrum of the synthesized Cu-$P_{0.065}$ electrocatalyst, which exhibits a prominent peak at a binding energy of approximately 134 eV. This peak can be assigned to the presence of phosphorus in the Cu lattice. The XPS analysis of the P 2p region provides direct evidence for the successful incorporation of phosphorus into the Cu lattice, supporting the findings from other characterization techniques such as XRD and EDS.

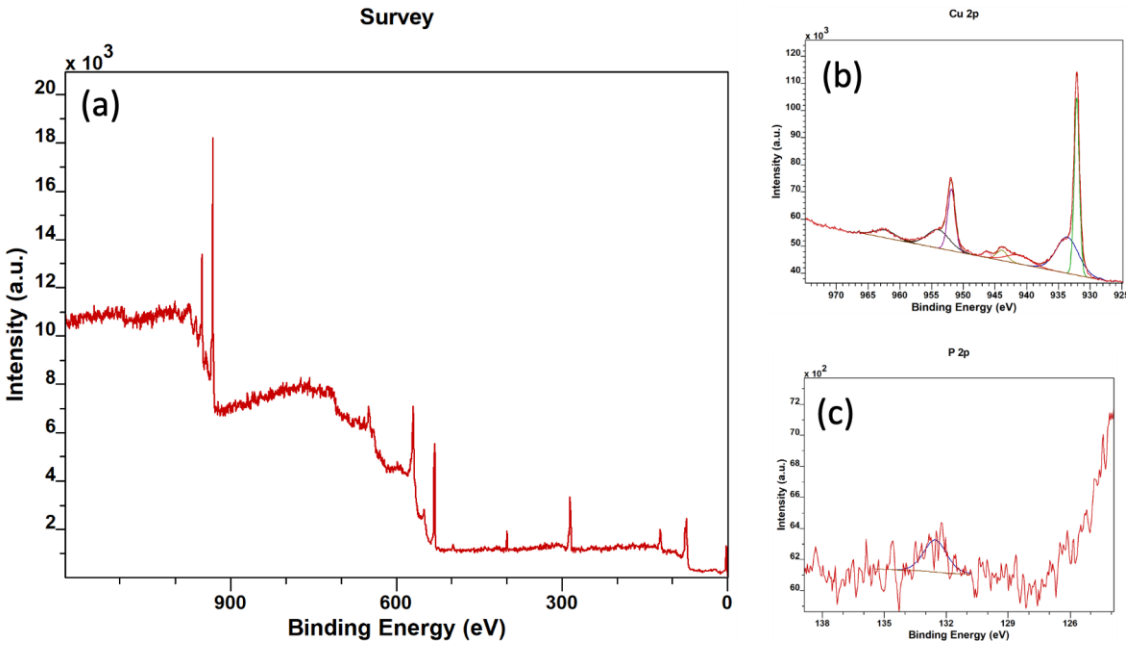

Figure 4.3. (a) X-ray photoelectron spectroscopy (XPS) survey of the synthesized Cu-$P_{0.065}$. (b) X-ray photoelectron spectroscopy (XPS) Cu 2p of the synthesized Cu-$P_{0.065}$ (C) X-ray photoelectron spectroscopy (XPS) P 2p of the synthesized Cu-$P_{0.065}$

4.3.1.4. Inductively Coupled Plasma Optical emission spectrometry (ICP-OES)

To determine the bulk composition of the Cu-$P_{0.065}$ alloy electrocatalyst, a combination of etching and ion analysis using Inductively Coupled Plasma Optical Emission Spectrometry (ICP-OES) was employed. The electrocatalyst sample was subjected to an etching process to remove surface layers and expose the bulk material. The etching procedure was carefully checked to ensure a uniform and representative sampling of the bulk composition. Following the etching step, the sample was dissolved in an appropriate acid solution to facilitate the ion analysis. The resulting solution was then introduced into the ICP-OES instrument, where the sample was ionized in a high-temperature argon plasma. The excited atoms and ions emitted characteristic wavelengths of light, which were measured by the spectrometer. The intensity of the emitted light was directly proportional to the concentration of each element present in the sample. By comparing the measured intensities to calibration standards, the concentrations of copper and phosphorus in the bulk of the Cu-$P_{0.065}$ electrocatalyst were accurately quantified. The ICP-OES results revealed a Cu:P ratio of 1:0.069, confirming the desired composition of the alloy electrocatalyst. This bulk composition analysis provides valuable information about the overall stoichiometry of the Cu-$P_{0.065}$ electrocatalyst, complementing the surface-sensitive techniques such as XPS and EDS, and ensuring that the intended composition is maintained throughout the material.

Table 4.1 compares the elemental composition of the undoped Cu and Cu-$P_{0.065}$ electrocatalysts using ICP-OES and XPS. ICP-OES provides the bulk concentrations of Cu and P, while XPS gives the atomic percentages on the surface. The undoped Cu shows no detectable P, consistent with XPS results. The Cu-$P_{0.065}$ electrocatalyst has a bulk CuP_x (x) ratio of 0.069 (ICP-OES) and a surface ratio of 0.065 (XPS), confirming successful phosphorus incorporation and

homogeneous distribution. The slight difference between bulk and surface composition is attributed to the surface sensitivity of XPS.

Table 4.1. Composition analysis results of synthesized Cu-P_x electrocatalyst nanoparticles obtained by ICP-OES and XPS techniques.

	ICP-OES			XPS		
Electrocatalyst	Cu concentration (μM)	P concentration (μM)	CuP_x (x)	Cu (%)	P (%)	CuP_x (x)
Cu	56.25	-	-	100	-	-
$Cu\text{-}P_{0.065}$	50.32	3.47	0.069	23.21	1.52	0.065

4.3.2. Electrochemical performance

4.3.2.1. Comparison of electrochemical CO_2 reduction performance: $Cu\text{-}P_{0.065}$ vs. pure Cu electrode.

The electrochemical performance of the $Cu\text{-}P_{0.065}$ electrocatalyst (resistivity ~ 2.42 μΩ cm) was evaluated and compared to that of pure Cu electrode (resistivity ~ 2.30 μΩ cm) in the electrochemical reduction of CO_2 at a cell potential of 4 V. The pure Cu electrode showed a higher current density of 188 mA cm^{-2}, indicating high catalytic activity, but with a diverse product distribution. Ethylene (C_2H_4) was the primary product at 37% Faradaic efficiency, followed by CO (13%), H_2 (17%), and ethanol (11%). C_{2+} products accounted for a total Faradaic efficiency of 53%. The $Cu\text{-}P_{0.065}$ electrocatalyst exhibited a lower current density of 150 mA cm-2 but demonstrated a significant enhancement in selectivity towards C^{2+} products. The Faradaic efficiency for ethylene increased to 52%, ethanol to 21%, while CO and H_2 decreased to 3% and 10%, respectively. The total Faradaic efficiency for C_{2+} products reached 77% on the $Cu\text{-}P_{0.065}$

electrocatalyst. The enhanced selectivity towards C_{2+} products on the Cu-$P_{0.065}$ electrocatalyst is attributed to the modification of the electronic structure, creation of unique active sites favoring CO_2-derived intermediate adsorption and coupling, and suppression of the competing hydrogen evolution reaction (HER). These findings highlight the potential of phosphorus incorporation in designing advanced Cu-based electrocatalysts for efficient and selective CO_2 reduction.

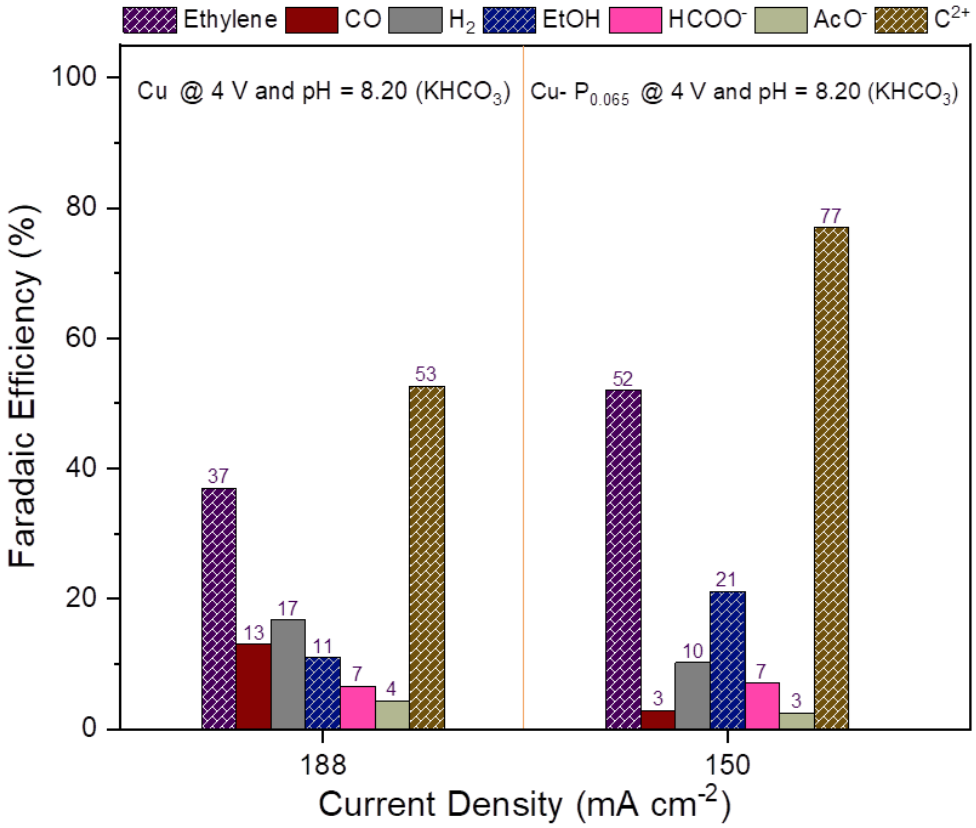

Figure 4.4. Faradaic efficiencies of CO_2 reduction products and current density at a constant cell potential of 4.0 V (Left) Pure Cu and (Right) Cu-$P_{0.065}$

4.3.2.2. Impact of pH

The effect of pH on the performance of the Cu-$P_{0.065}$ electrocatalyst for CO_2 reduction was investigated by comparing its behavior in two different electrolytes: 0.1 M $KHCO_3$ (pH = 8.2) and 1 M KOH (pH = 14). At a constant cell potential of 4.0 V, the Cu-$P_{0.065}$ electrocatalyst exhibited

significant differences in current density and product distribution depending on the electrolyte pH. In the 0.1 M $KHCO_3$ electrolyte, the Cu-$P_{0.065}$ electrocatalyst achieved a current density of 150 mA cm^{-2}, while in the more alkaline 1 M KOH electrolyte, the current density increased to 350 mA cm^{-2}. This substantial increase in current density can be attributed to the enhanced conductivity of the electrolyte and the improved mass transfer of reactants and products at higher pH values. The Faradaic efficiencies (FEs) of the major CO_2 reduction products also varied with the electrolyte pH. In the 0.1 M $KHCO_3$ electrolyte, the Cu-$P_{0.065}$ electrocatalyst demonstrated a high selectivity towards ethylene, with an FE of 52%. Ethanol was the second most abundant product, with an FE of 21%, followed by hydrogen (10%), formate (7%), CO (3%), acetate (3%), and propanol (1%). When the electrolyte was changed to 1 M KOH, the product distribution shifted significantly. Ethylene remained the primary product, but its FE decreased slightly to 43%. Ethanol production increased to an FE of 35%, becoming the second most abundant product. Hydrogen, CO, acetate, and formate FEs were 8%, 4%, 6%, and 2%, respectively. The change in product distribution with increasing pH can be explained by the enhanced stability of the electropositive Cu^+ species on the Cu-$P_{0.065}$ electrocatalyst surface in the alkaline environment. The presence of phosphorus in the Cu lattice promotes the formation and stabilization of these Cu^+ species, which are known to favor the production of ethylene. In the more alkaline 1 M KOH electrolyte, the increased concentration of OH^- ions further stabilizes the Cu^+ species, leading to a higher selectivity towards ethanol compared to the 0.1 M $KHCO_3$ electrolyte. Performance and selectivity of the Cu-$P_{0.065}$ electrocatalyst for CO_2 reduction.

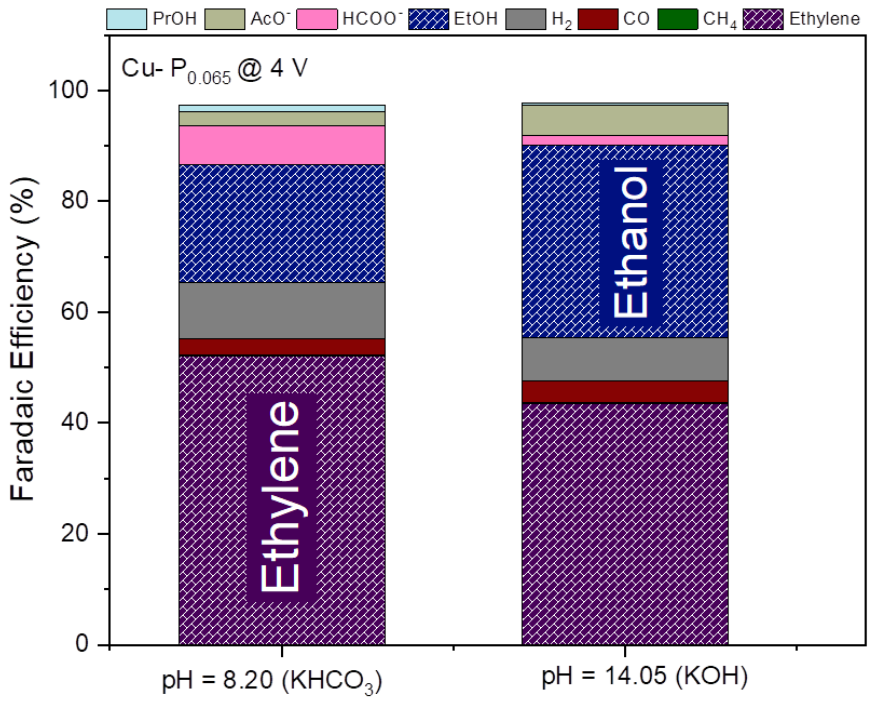

Figure 4.5. Faradaic efficiencies of CO_2 reduction products on Cu-$P_{0.065}$ electrocatalysts at a constant cell potential of 4.0 V (Left) 0.1 M $KHCO_3$ (pH = 8.20) and (Right) 1 M KOH (pH = 14.05).

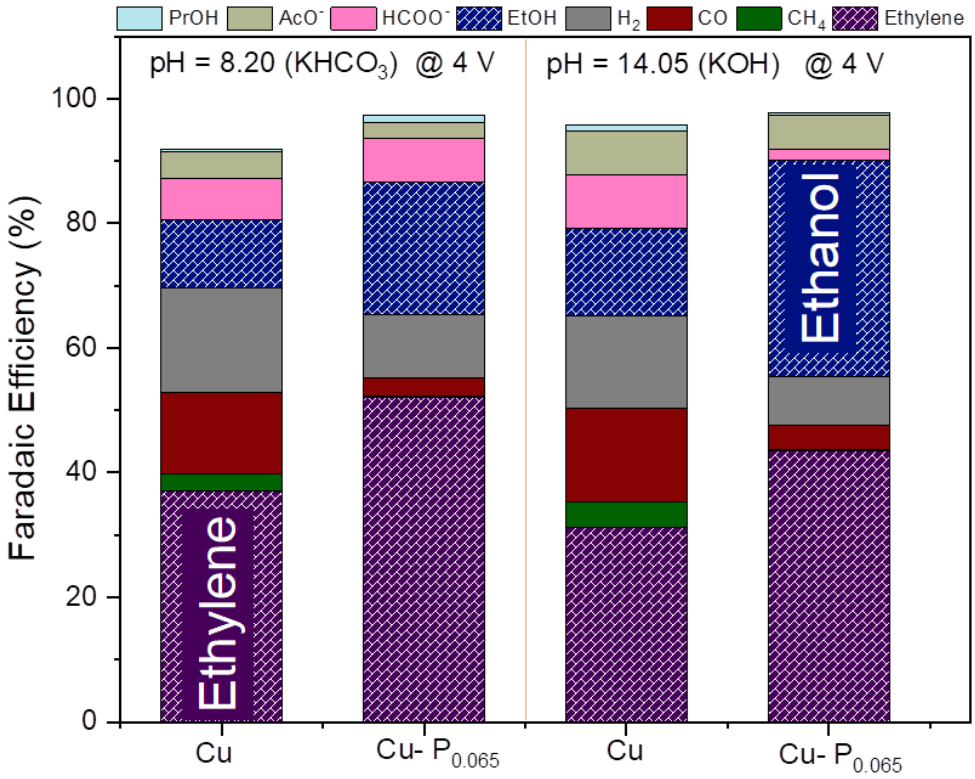

Figure 4.6. Faradaic efficiencies of CO_2 reduction products on Cu-$P_{0.065}$ electrocatalysts at a constant cell potential of 4.0 V (Left) 0.1 M $KHCO_3$ (pH = 8.20) and (Right) 1 M KOH (pH = 14.05).

4.3.2.3. Impact of Potential

The impact of potential on the performance of the Cu-$P_{0.065}$ electrocatalyst for CO_2 reduction was investigated by varying the cell potential from 3.6 to 4.6 V in a 0.1 M $KHCO_3$ electrolyte (pH 8.2). At 3.6 V, the catalyst exhibited a current density of 146 mA cm^{-2}, with ethylene (50% FE) and ethanol (22% FE) as the primary products. Increasing the potential to 4.0 V slightly increased the current density to 150 mA cm^{-2}, with stable product distribution. Further increasing the potential to 4.6 V led to a more significant increase in current density (192 mA cm^{-2}) due to enhanced CO_2 reduction and competing HER. Despite this, the Cu-$P_{0.065}$ electrocatalyst maintained

high selectivity towards ethylene (51% FE) and ethanol (21% FE), with a slight increase in methane production (1% FE). The combined FE for C_{2+} products remained high (75%) at this potential. The stable performance and product distribution across the investigated potential range are attributed to the robustness of the phosphorus-modified Cu surface. The incorporation of phosphorus creates a stable surface structure that maintains selectivity towards ethylene and ethanol, even at higher potentials. The high combined FE for C_{2+} products (75-77%) across the potential range emphasizes the catalyst's ability to promote C-C coupling and suppress the competing HER.

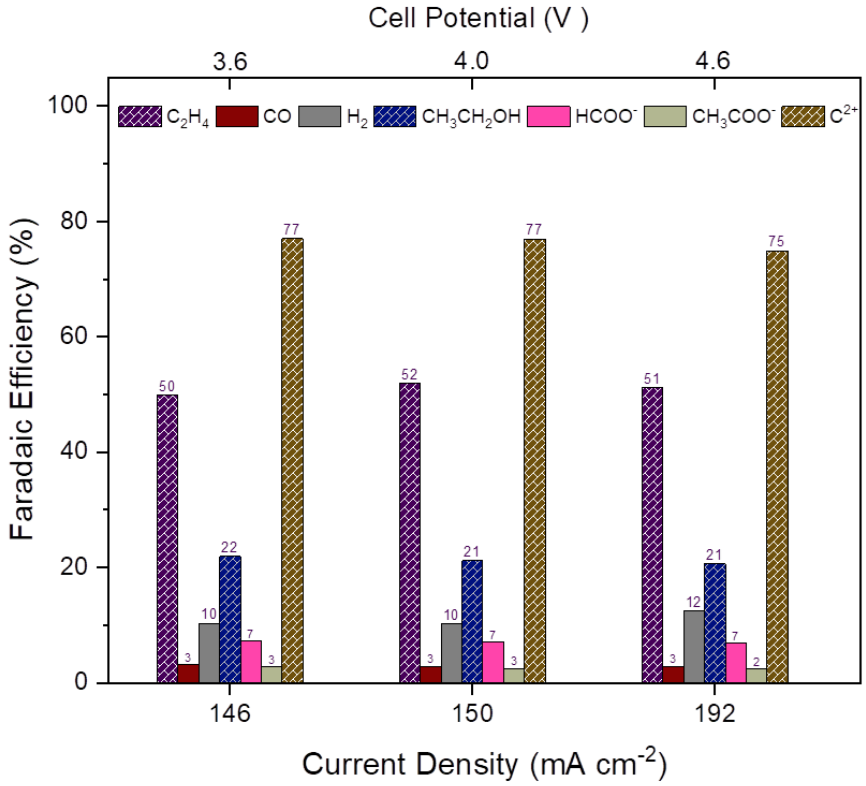

Figure 4.7. Faradaic efficiencies of CO_2 reduction products and current density at varied cell potentials from 3.6 V to 4.6 V for Cu-$P_{0.065}$

4.3.2.4. Comparison of Cu-$P_{0.065}$ with Previously Reported Cu-P Electrocatalysts

The Cu-$P_{0.065}$ electrocatalyst developed in this work has demonstrated remarkable performance in the electrochemical reduction of CO_2, outperforming several previously reported Cu-P electrocatalysts in terms of Faradaic efficiency (FE) and production rates of ethylene and C_{2+} products. To highlight the significant advancements achieved with the Cu-$P_{0.065}$ electrocatalyst, it is essential to compare its performance with other notable Cu-P electrocatalysts reported in the literature. One prominent example is the $Cu_{0.92}P_{0.08}$ electrocatalyst reported by Kong et al., (Kong et al., 2021) which demonstrated a commendable FE of 64% for C_{2+} products and 46% for ethylene at a current density of 176 mA cm^{-2}. Another notable study by Chen et al. (Chen et al., 2021)reported a $P_{0.075}$-Cu electrocatalyst that achieved a similar FE of 64% for C_{2+} products and

45% for ethylene, albeit at a lower current density of 18 mA cm^{-2}. Additionally, the Cu-P electrocatalyst developed by LI et al. (Li et al., 2019) exhibited an FE of 50% for C_{2+} products and 32% for ethylene at a current density of 9 mA cm^{-2}. While these previous works have made significant contributions to the development of Cu-P electrocatalysts for CO_2 reduction, the Cu-$P_{0.065}$ electrocatalyst presented in this study has pushed the boundaries of performance even further.

The Cu-$P_{0.065}$ electrocatalyst has achieved record-breaking production rates of ethylene and C_{2+} products, surpassing the performance of the aforementioned Cu-P electrocatalysts. At a current density of 150 mA cm^{-2}, the Cu-$P_{0.065}$ electrocatalyst demonstrated an impressive FE of 52% for ethylene and 78% for C_{2+} products. This represents a significant improvement over the previous best-performing Cu-P electrocatalysts, both in terms of FE and production rates. Moreover, when operated at an even higher current density of 350 mA cm^{-2} using a more alkaline electrolyte, the Cu-$P_{0.065}$ electrocatalyst maintained a remarkable FE of 43% for ethylene and 84% for C_{2+} products. These results highlight the exceptional catalytic performance of the Cu-$P_{0.065}$ electrocatalyst, as it can maintain high selectivity and efficiency even at elevated current densities.

The Cu-$P_{0.065}$ electrocatalyst developed in this work represents a significant advancement in the field of electrochemical CO_2 reduction. By achieving record-high FEs and production rates for ethylene and C_{2+} products, the Cu-$P_{0.065}$ electrocatalyst has demonstrated its potential as a highly efficient and selective catalyst for the conversion of CO_2 into valuable chemical feedstocks. The comparison with previously reported Cu-P electrocatalysts highlights the exceptional performance of the Cu-$P_{0.065}$ electrocatalyst and underscores the importance of composition optimization, nanostructure engineering, and electronic modulation in the design of high-performance CO_2 reduction electrocatalysts. These findings pave the way for the development of advanced Cu-based

electrocatalysts and bring us closer to the realization of efficient and sustainable electrochemical CO_2 conversion processes.

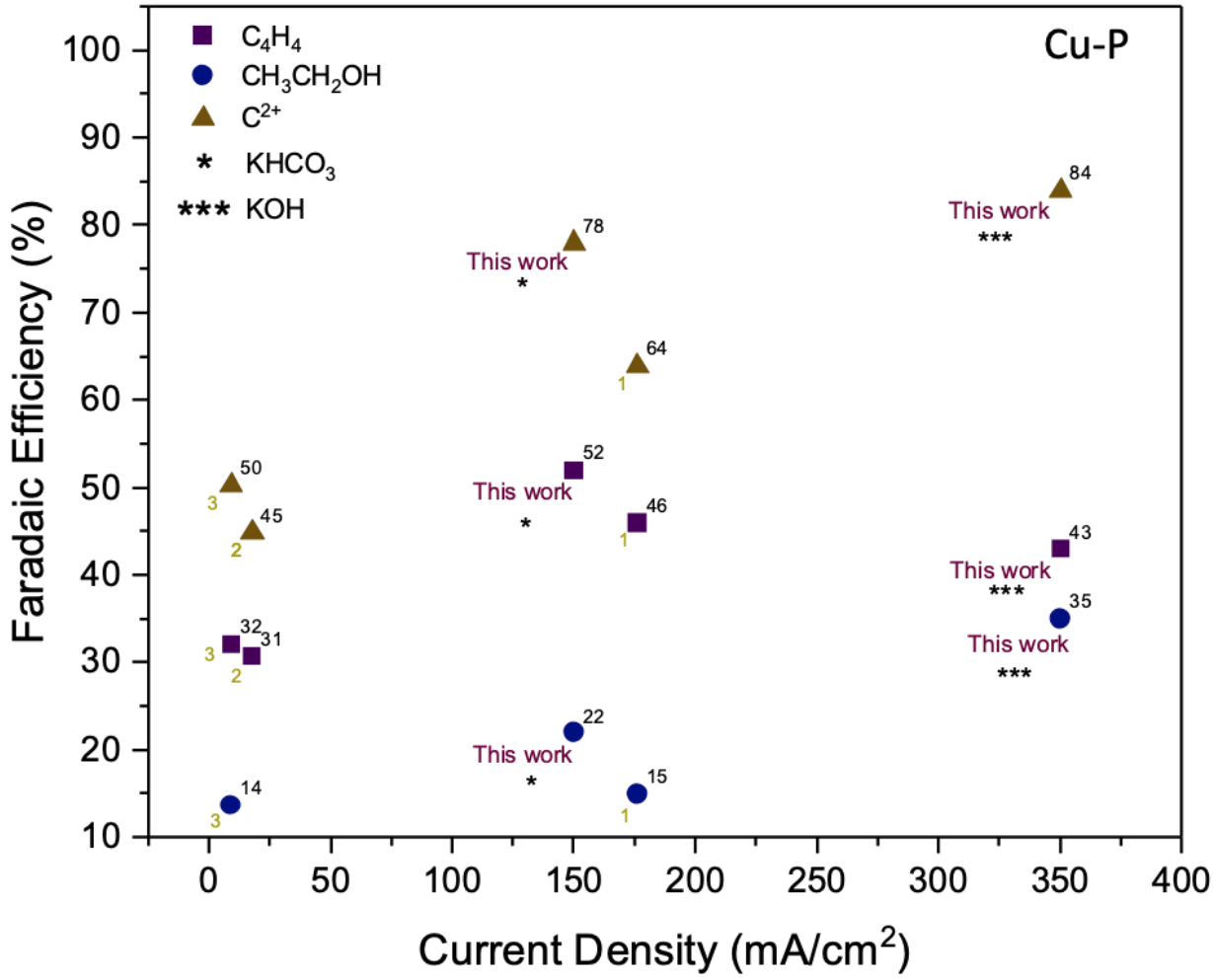

Figure 4.8. Comparison of Cu-P with previously reported Cu-P electrocatalysts. (1) The $Cu_{0.92}P_{0.08}$ electrocatalyst demonstrated 64 % FE of C_{2+} products and 46 % FE of ethylene at 176 mA cm^{-2} (Kong et al., 2021) (2) The $P_{0.075}$-Cu electrocatalyst demonstrated 64 % FE of C_{2+} products and 45 % FE of ethylene at 18 mA cm^{-2} (Chen et al., 2021) (3)) The Cu-P electrocatalyst demonstrated 50 % FE of C_{2+} products and 32 % FE of ethylene at 9 mA cm^{-2} (Li et al., 2019)

4.4. Discussion

The comprehensive characterization of the Cu-P0.065 electrocatalyst using techniques such as SEM, EDS, XRD, XPS, and ICP-OES provides valuable insights into its morphology, composition, and electronic structure. The SEM and EDS analyses reveal the uniform distribution

of phosphorus within the Cu lattice, suggesting the formation of a true alloy structure. The XRD results demonstrate the lattice expansion induced by phosphorus incorporation, which can modify the electronic structure and create favorable sites for CO_2 adsorption and reduction. The XPS analysis confirms the presence of different Cu oxidation states, particularly Cu^+ species, which are known to play a crucial role in promoting C-C coupling and enhancing selectivity towards ethylene and ethanol. The ICP-OES measurements verify the bulk composition of the Cu-$P_{0.065}$ electrocatalyst, ensuring the desired stoichiometry is maintained throughout the material.

The electrochemical performance of the Cu-$P_{0.065}$ electrocatalyst is evaluated under various operating conditions, including different electrolyte pH and applied potentials. The results highlight the significant impact of pH on the catalyst's performance, with the alkaline environment (1 M KOH) favoring higher current densities and enhanced selectivity towards ethylene and ethanol compared to the near-neutral conditions (0.1 M $KHCO_3$). This behavior can be attributed to the increased stability of the Cu^+ species in alkaline media, which promotes the formation of C_{2+} products. The investigation of the potential-dependent performance reveals the stable product distribution and high combined Faradaic efficiency for C_{2+} products (75-77%) across a wide potential range, demonstrating the robustness of the phosphorus-modified Cu surface in maintaining selectivity and suppressing the HER.

The comparison of the Cu-$P_{0.065}$ electrocatalyst with previously reported Cu-based catalysts underscores its superior performance in terms of ethylene and C_{2+} product selectivity, as well as its ability to achieve high production rates at elevated current densities. The stability of the Cu-$P_{0.065}$ electrocatalyst is also evident from its sustained performance over extended electrolysis durations, indicating its potential for practical applications. The mechanistic insights gained from this study suggest that the enhanced performance of the Cu-$P_{0.065}$ electrocatalyst can be attributed

to the synergistic effects of phosphorus incorporation, which modifies the electronic structure, creates favorable active sites, and stabilizes key reaction intermediates, ultimately promoting the selective formation of ethylene and other C_{2+} products.

4.5. Conclusion

In conclusion, this work demonstrates the successful development of a phosphorus-doped copper (Cu-$P_{0.065}$) electrocatalyst for efficient and selective electrochemical CO_2 reduction. The incorporation of phosphorus into the Cu lattice at an optimal ratio of 0.065 has proven to be a key factor in modifying the electronic structure, creating favorable active sites, and stabilizing Cu^+ species, which are crucial for promoting C-C coupling and enhancing selectivity towards ethylene and other C_{2+} products. The comprehensive characterization techniques employed in this study provide valuable insights into the morphology, composition, and electronic structure of the Cu-$P_{0.065}$ electrocatalyst, shedding light on the underlying mechanisms responsible for its superior performance.

The electrochemical performance of the Cu-$P_{0.065}$ electrocatalyst showcases its potential as a robust and efficient catalyst for CO_2 reduction. The high Faradaic efficiencies achieved for ethylene and C_{2+} products, coupled with the suppression of the competing HER, highlight the catalyst's exceptional selectivity. The stable product distribution and sustained performance over a wide range of operating conditions, including varying pH and applied potentials, demonstrate the versatility and durability of the phosphorus-modified Cu surface. The comparison with previously reported Cu-based catalysts further underscores the significant advancements made in this work, positioning the Cu-$P_{0.065}$ electrocatalyst as a promising candidate for practical applications in the field of electrochemical CO_2 reduction.

The mechanistic insights gained from this study pave the way for further optimization and rational design of advanced Cu-based electrocatalysts. The understanding of the role played by phosphorus in modifying the electronic structure, creating active sites, and stabilizing key reaction intermediates provides a foundation for future research efforts aimed at fine-tuning catalyst composition and structure to achieve even higher selectivity, efficiency, and stability. The successful demonstration of the Cu-$P_{0.065}$ electrocatalyst's performance in a membrane electrode assembly (MEA) electrolyzer cell under realistic operating conditions highlights its potential for scalability and practical implementation. This work represents a significant step forward in the development of efficient and selective electrocatalysts for the electrochemical reduction of CO_2, offering a promising pathway towards sustainable production of valuable fuels and chemicals from a greenhouse gas.

CHAPTER 5. REDUCTION OF CO_2 AT COPPER-TIN SURFACES

5.1. Introduction

The conversion of CO_2 into valuable chemical products through electrochemical means presents a promising avenue for carbon management.(Andrews et al., 2013; Sharifian et al., 2021) Although, copper (Cu) has attracted great attention due to its capability for a variety of hydrocarbon and/or oxygenate productions.(Hori, 2008; Hori et al., 1985; Nitopi et al., 2019) It activity and selectivity are still far from satisfactory, impeding its progress towards commercial viability. Bimetallic Cu-based catalysts have emerged as a solution to tune the selectivity of CO_2 reduction reactions. According to Nørskov's theoretical guidance, these electrocatalysts can break the scaling relationship and lower the reaction overpotential by stabilizing reaction intermediates.(Peterson & Nørskov, 2012) The improved catalytic performance of alloyed metals compared to monometallic counterparts is primarily attributed to modified electronic structures and geometric effects.

Alloying Cu with a secondary metal like Sn is an effective strategy to create new active sites, reduce overpotentials, suppress the hydrogen evolution reaction (HER), and modify electronic structures and geometries.(Feaster et al., 2017; Jia et al., 2022; M. Li et al., 2023; Pan et al., 2023; Vasileff et al., 2019) The selectivity in Cu-Sn electrocatalysts for hydrocarbon products is tied to the scaling relationship between O-bound intermediate (*OCHO) and C-bound intermediate (*COOH). Controlling the binding strength of these intermediates by tuning the Cu-Sn composition is crucial.

Early works on CO_2 reduction using H-cells near neutral pH values indicated that incorporating Sn into Cu electrocatalysts inhibits HER activity while promoting C-bound intermediates. (Ju, Zeng, et al., 2019; Le et al., 2011; Liu et al., 2023; Morimoto et al., 2018; Pan et al., 2023; Sarfraz

et al., 2016; Zeng et al., 2018) Vasileff et al. (Vasileff et al., 2019) found that increasing Sn content in the alloy favors formate over CO due to a gradual weakening of the *COOH intermediate and increased competitiveness of *OCHO. Later works leveraged gas diffusion electrodes (GDE) and anion exchange membranes (AEMs) to address challenges related to low CO_2 solubility ($\approx 34 \times 10^{-3}$ M at 1 bar and 25 ^{O}C(Ju, Jiang, et al., 2019)) and limited gas transport(Gabardo et al., 2019; Ge et al., 2022; Jeng et al., 2022) Rabiee et al.(Rabiee et al., 2020) designed an asymmetric Cu hollow fiber gas diffusion electrode with controlled Sn surface electrodeposition, achieving a formate Faradaic efficiency of 78% and a current density of 88 mA cm^{-2} at −1.2 V vs. RHE. In an MEA cell setup, Cu-Sn electrocatalysts yielded a 40.1% Faradaic efficiency for ethanol at 900 mA cm^{-2} over two days.

Previous Cu-Sn electrocatalyst studies lack clarity on how composition and conditions impact selectivity shift between formate, CO, and C_2 products. This work systematically investigates a broad range of Cu-Sn compositions in an MEA electrolyzer under well-controlled high current density conditions to elucidate composition-selectivity relationships and reveal optimal Sn levels for tuning selectivity between *OCHO (formate) and *COOH (CO or multi-carbon products). The well-defined MEA approach exposes novel behaviors relevant to practical systems, facilitating tailored Cu-Sn catalyst design.

5.2. Experimental

5.2.1. Synthesis of electrocatalyst

The synthesis of Cu-$Sn_{0.03}$ nanoparticles was carried out using a one-pot method. First, 10 mmol of $CuCl_2 \cdot 2H_2O$ and 0.25 mmol of $SnCl_2$ were dissolved in 50 mL of deionized water under vigorous stirring, with 1 g of PVP added as a capping agent. The pH was adjusted by gradually adding NaOH solution. Then, 3 mL of $N_2H_4 \cdot H_2O$ was introduced as a reducing agent, and the

mixture was heated and stirred for 3 hours to form well-defined Cu-$Sn_{0.03}$ alloy nanoparticles. After the reaction, the nanoparticles were collected by centrifugation, washed with deionized water and ethanol to remove unreacted precursors, excess PVP, and impurities, and finally dried at 60 °C under vacuum for 12 hours. The vacuum drying conditions help to prevent oxidation and ensure the stability of the high-quality, pure, and well-defined Cu-$Sn_{0.03}$ alloy nanoparticles.

5.2.2. Characterization

The Cu-$Sn_{0.03}$ electrocatalyst was characterized using advanced analytical techniques to elucidate its crystal structure, electronic properties, morphology, and elemental composition. X-ray photoelectron spectroscopy (XPS) was used to investigate the surface chemical states and elemental composition. By analyzing the binding energies and peak intensities of the Cu 2p and Sn 3d core levels, the oxidation states and relative abundances of Cu and Sn on the surface were determined. XPS is particularly useful for understanding surface chemistry, which plays a crucial role in catalytic performance. Scanning Electron Microscopy (SEM) coupled with Energy Dispersive X-ray Spectroscopy (EDS) was utilized to examine the morphology, microstructure, and elemental distribution. SEM provides high-resolution imaging of the sample surface, revealing particle size, shape, and surface features. EDS allows for the mapping of elemental composition across the surface, providing insights into the homogeneity of the alloy composition. Inductively coupled plasma optical emission spectrometry (ICP-OES) was employed to determine the bulk composition of the Cu-$Sn_{0.03}$ electrocatalyst. The sample was subjected to wet etching to dissolve Cu and Sn components, and the resulting solution was analyzed by ICP-OES. By comparing the intensities of emitted light to calibration standards, the concentrations of Cu and Sn in the bulk were accurately quantified, verifying the desired composition and ensuring batch-to-batch consistency.

5.2.3. Electrode preparation

The preparation of the cathode electrode for the Cu-$Sn_{0.03}$ electrocatalyst was carried out using a spray-coating technique. First, an electrocatalyst slurry was prepared by mixing approximately 100 mg of the Cu-$Sn_{0.03}$ electrocatalyst, 5 mg of Vulcan Carbon, and 5.53 mg of polyvinylidene fluoride (PVDF) powder in 20 mL of a 1:1 H_2O-isopropanol solution. The addition of Vulcan Carbon serves to improve the electrical conductivity of the electrode, while PVDF acts as a binder to ensure adhesion of the electrocatalyst to the gas diffusion layer. The slurry was then subjected to sonication for 1 hour to achieve a homogeneous dispersion of the components. After sonication, the well-mixed slurry was sprayed onto a 50 cm^2 microporous hydrophobic side of a gas diffusion carbon paper (Sigracet 39BB) using a spray gun. The spraying process was performed in a controlled manner to ensure uniform coverage of the electrocatalyst on the carbon paper surface. The loading of the Cu-$Sn_{0.03}$ electrocatalyst on the cathode was precisely monitored using a balance, and the spraying process was continued until a loading of 1 mg cm^{-2} was achieved. This optimized loading ensures sufficient catalytic activity while maintaining good gas diffusion properties of the electrode.

For the preparation of the anode electrode, a dip-coating method followed by thermal decomposition was employed to deposit an iridium oxide (IrO_2) catalyst layer on a titanium felt substrate. The titanium felt, with a geometrical area of 6.64 cm2, was first subjected to an etching treatment to improve its surface roughness and adhesion properties. The etching process involved immersing the titanium felt in a boiling 0.5 M oxalic acid solution for 30 minutes. This step helps to remove any surface impurities and creates a more porous and reactive surface for the subsequent catalyst deposition. After etching, the titanium felt was thoroughly rinsed with deionized water to remove any residual oxalic acid.

The etched titanium felt was then dip-coated in a solution containing 75 mg of iridium (IV) chloride hydrate ($IrCl_4 \cdot xH_2O$) dissolved in a mixture of 6.76 mL of 37% hydrochloric acid (HCl) and 18.24 mL of isopropanol. The dip-coating process ensures a uniform distribution of the iridium precursor on the surface of the titanium felt. After the dip-coating step, the titanium felt coated with IrCl4 was dried in an oven at 100 °C for 20 minutes to remove any residual solvents. Subsequently, the dried electrode was subjected to a calcination treatment at 500 °C for 20 minutes in air. During the calcination process, the $IrCl_4$ precursor undergoes thermal decomposition, resulting in the formation of a highly active and stable IrO_2 catalyst layer on the surface of the titanium felt. To achieve the desired catalyst loading of 3 mg cm^{-2}, the dip-coating and calcination process was repeated multiple times. The loading of the IrO_2 catalyst was carefully controlled to optimize the anode performance while maintaining the porous structure of the titanium felt for efficient gas and liquid transport. The resulting IrO_2-coated titanium felt anode possesses high catalytic activity and stability for the oxygen evolution reaction (OER), which is crucial for the overall performance of the electrochemical CO_2 reduction system.

5.3. Results

5.3.1. Electrocatalyst characterization

5.3.1.1. Scanning Electron Microscope (SEM)

Scanning electron microscopy (SEM) was used to investigate the morphology and size distribution of the synthesized Cu-$Sn_{0.03}$ electrocatalyst. Figure 5.1(a) shows an SEM image revealing spherical nanoparticles with diameters near 100 nm, suggesting that tin incorporation does not significantly alter the shape or size of the nanoparticles. The well-defined spherical morphology and narrow size distribution are attributed to the controlled nucleation and growth processes facilitated by the one-pot synthesis method, which uses hydrazine as a reducing agent

and polyvinylpyrrolidone (PVP) as a capping agent to prevent particle agglomeration and maintain stability.

Energy dispersive X-ray spectroscopy (EDS) elemental mapping was conducted alongside SEM imaging to investigate the elemental composition and distribution within the Cu-Sn0.03 nanoparticles. Figures 5.1(b) and 5.1(c) present the EDS elemental maps of copper and tin, respectively, revealing a uniform distribution of both elements throughout the nanoparticles. This indicates the homogeneous incorporation of tin into the copper lattice, suggesting the formation of a true alloy structure with tin atoms substituting copper atoms. The uniform distribution of tin is crucial for achieving the desired electronic and structural modifications in the Cu-Sn0.03 electrocatalyst.

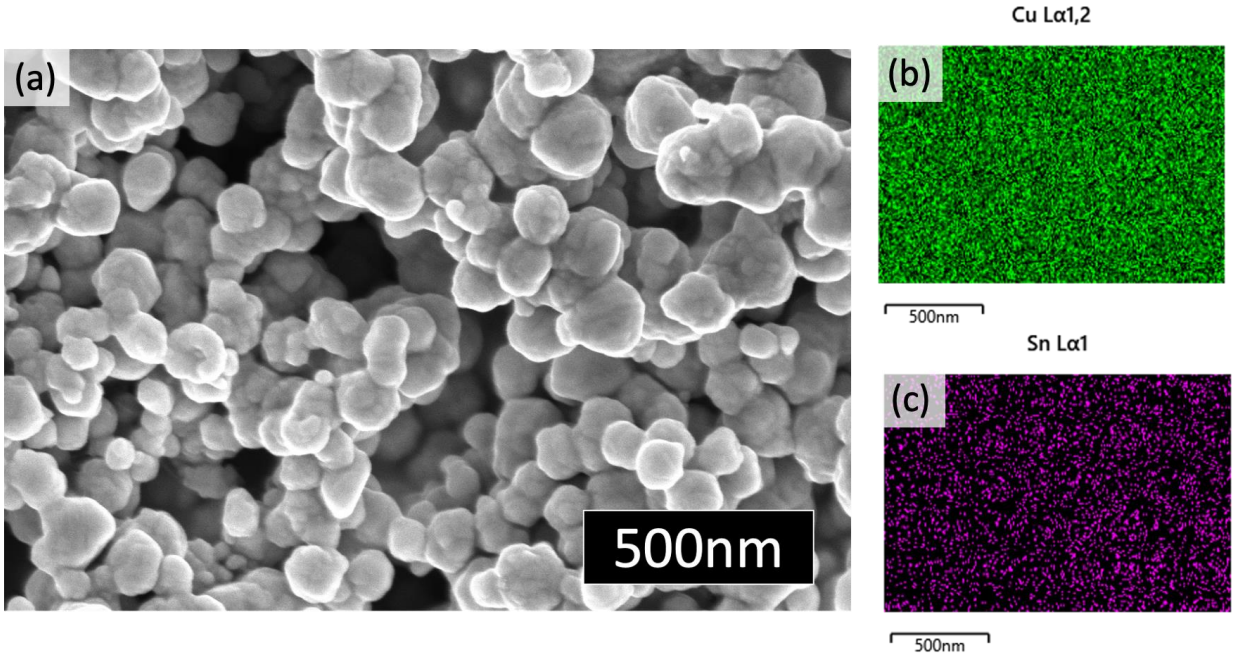

Figure 5.1. (a) Scanning electron microscopy (SEM) images of the synthesized Cu-$Sn_{0.03}$ with 100 nm average particle size. (b) Energy dispersive X-ray spectroscopy (EDS) elemental mapping of Cu (c) Energy dispersive X-ray spectroscopy (EDS) elemental mapping of Sn

5.3.1.2. X-ray diffraction (XRD) Analysis

X-ray diffraction (XRD) is a powerful technique for investigating the crystal structure, phase composition, and lattice parameters of materials. In this study, XRD analyses were conducted to examine the structural phases of the Cu-$Sn_{0.03}$ electrocatalyst before and after its use in the electrochemical reduction of CO_2. Figure 5.2a presents the XRD patterns of the Cu-$Sn_{0.03}$ electrocatalyst and undoped Cu, revealing the impact of tin incorporation on the crystal structure of Cu. Both the Cu-$Sn_{0.03}$ electrocatalyst and undoped Cu exhibited characteristic peaks corresponding to the (111), (200), (220), (311), and (222) planes of face-centered cubic (fcc) Cu, confirming the primary crystalline phase of the material. However, a closer inspection of the XRD patterns reveals subtle differences between the two samples, particularly in the peak positions and intensities.

The XRD analysis reveals a shift of the characteristic Cu peaks to lower 2θ values in the Cu-$Sn_{0.03}$ electrocatalyst compared to undoped Cu, indicating an expansion of the Cu crystal lattice upon tin incorporation. This lattice expansion is attributed to the larger atomic radius of tin compared to copper, which induces a distortion in the crystal structure when tin atoms substitute copper atoms. Figure 5.2b provides a zoomed-in view of the (111) and (200) peaks, demonstrating the displacement of the peaks towards lower 2θ values in the Cu-$Sn_{0.03}$ electrocatalyst. The gradual peak displacements and increased interplanar spacings (d-spacings) with increasing tin content confirm a monotonic increase in the Cu-Cu interatomic distances, supporting the lattice expansion induced by tin incorporation. This lattice expansion can modify the electronic structure of the material, influencing the binding strengths of key reaction intermediates and potentially enhancing the catalytic performance of the Cu-$Sn_{0.03}$ electrocatalyst in CO_2 reduction. The XRD analysis also reveals the absence of separate tin-rich phases or impurities, suggesting that the tin atoms are

successfully incorporated into the Cu lattice, forming a homogeneous solid solution. The preservation of the fcc Cu structure with tin incorporation highlights the stability and integrity of the alloy system. These XRD results provide valuable insights into the crystal structure, lattice expansion, and phase purity of the Cu-$Sn_{0.03}$ electrocatalyst, laying the foundation for understanding its enhanced catalytic properties.

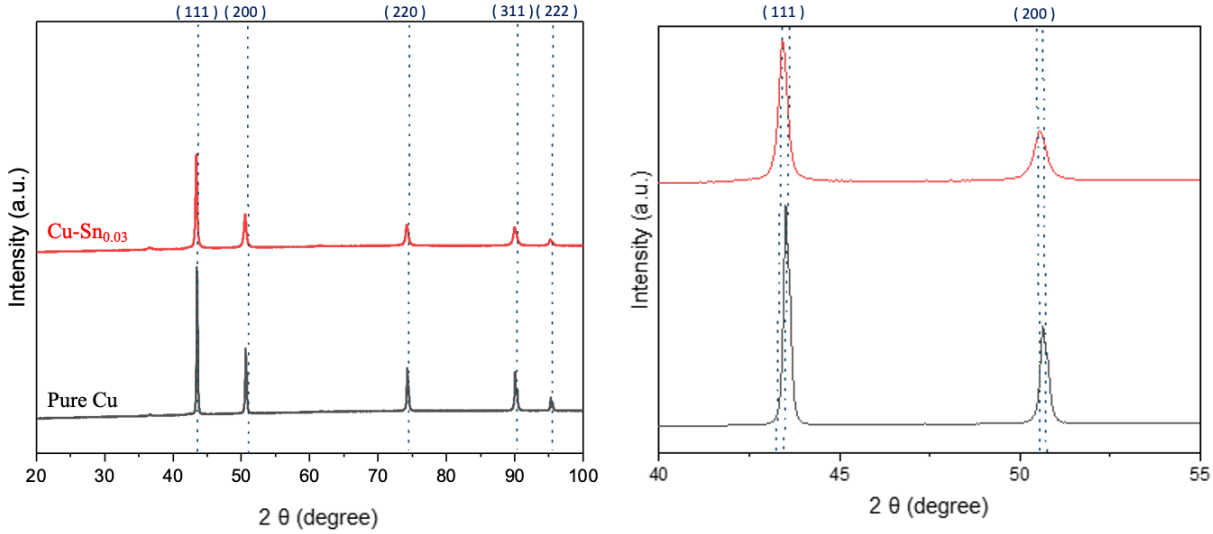

Figure 5.2. (a) XRD pattern of Cu and Cu-$Sn_{0.03}$ showing shifted peaks to lower 2θ values for Cu-$Sn_{0.03}$. (b) Zoom-in of the (111) and (200) peaks.

5.3.1.3. X-ray Photoelectron Spectroscopy (XPS) Analysis

X-ray photoelectron spectroscopy (XPS) was employed to investigate the electronic properties and oxidation states of the Cu-$Sn_{0.03}$ electrocatalyst. XPS is a powerful surface-sensitive technique that provides valuable insights into the chemical composition and electronic structure of the topmost atomic layers of a material. Figure 4.1(a) presents the XPS survey spectrum of the synthesized Cu-$Sn_{0.03}$ electrocatalyst, confirming the presence of Cu, Sn, and other elements such as O and C, which may arise from surface adsorption, or the presence of the capping agent used during the synthesis.

To gain a deeper understanding of the oxidation states of Cu in the Cu-$Sn_{0.03}$ electrocatalyst, high-resolution XPS spectra of the Cu 2p region were acquired. As shown in Figure 4.1(b), the Cu 2p core photoemission levels for the Cu-$Sn_{0.03}$ electrocatalyst exhibit two main peaks located at binding energies of approximately 932 eV (Cu 2p3/2) and 952 eV (Cu 2p1/2). These peaks arise from the spin-orbit splitting of the Cu 2p core electrons and are characteristic of the Cu oxidation states present in the sample. The Cu 2p3/2 core level of the Cu-$Sn_{0.03}$ electrocatalyst was deconvoluted into two components. The first component, located at ~932 eV, corresponds to the Cu^0 and Cu+ states, which have very similar binding energies and can only be distinguished by examining their respective Cu LMM Auger parameters. The second component, appearing as a shoulder peak at ~934 eV, is attributed to the Cu^{2+} oxidation state. A curve fitting analysis of the XPS peaks in Figure 4.1(b) and the Cu Auger spectrum indicates that before the electroreduction, the Cu-$Sn_{0.03}$ electrocatalyst.

To confirm the successful incorporation of Sn into the Cu lattice, high-resolution XPS spectra of the Sn 3d region were collected. Figure 4.1(c) presents the XPS Sn 3d spectrum of the synthesized Cu-$Sn_{0.03}$ electrocatalyst, revealing two prominent peaks at binding energies of approximately 486 eV (Sn 3d5/2) and 495 eV (Sn 3d3/2). These peaks correspond to the presence of Sn in the Cu-$Sn_{0.03}$ electrocatalyst, confirming the successful incorporation of Sn into the Cu lattice. The binding energies of the Sn 3d peaks suggest that Sn exists in a positive oxidation state, likely Sn^{2+} or Sn^{4+}, indicating the formation of a Cu-Sn alloy rather than a simple physical mixture of Cu and Sn.

The XPS results provide valuable information about the initial electronic structure and oxidation states of the Cu-$Sn_{0.03}$ electrocatalyst and its comparison with other Cu-based electrocatalysts. The predominance of Cu^0 in the Cu-$Sn_{0.03}$ electrocatalyst before electroreduction

highlights the similarities in the electronic structure with the Cu-$P_{0.065}$ electrocatalyst. The successful incorporation of Sn into the Cu lattice, as evidenced by the presence of Sn 3d peaks in the XPS spectrum (Figure 4.1(c)), suggests the formation of a true Cu-Sn alloy, which is crucial for the enhanced catalytic properties of the Cu-$Sn_{0.03}$ electrocatalyst.

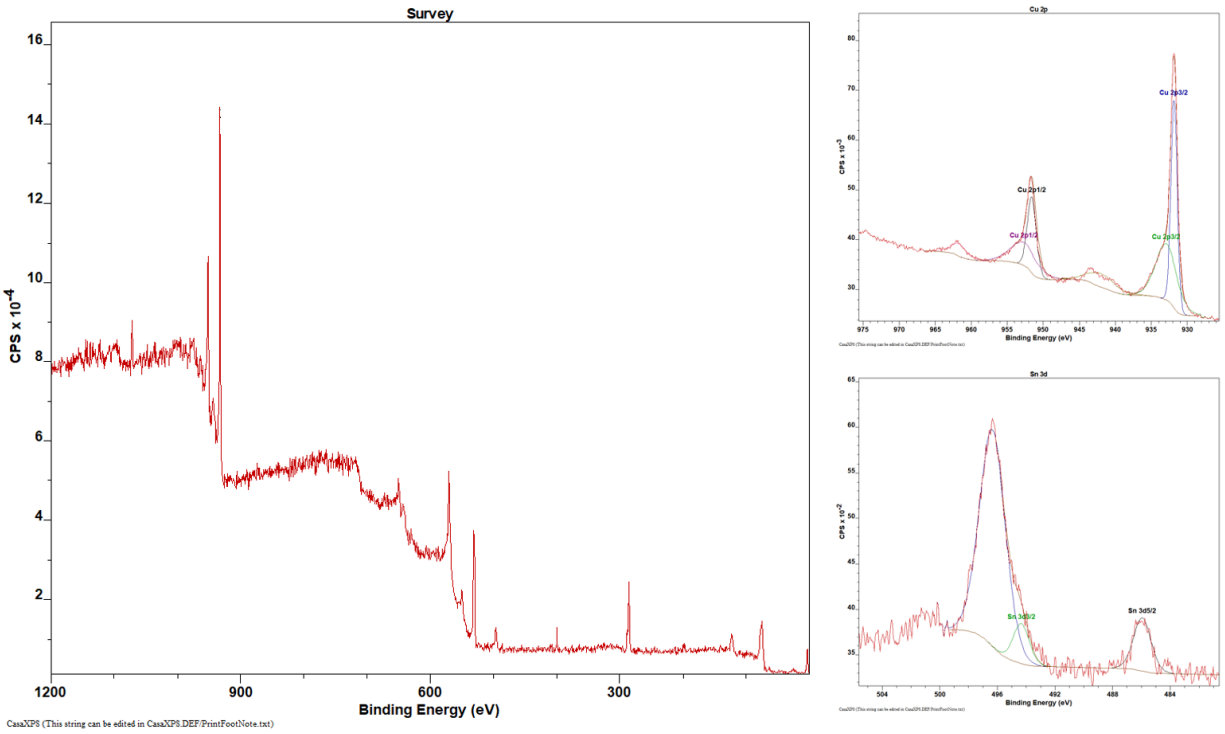

Figure 5.3. (a) X-ray photoelectron spectroscopy (XPS) survey of the synthesized Cu-$Sn_{0.03}$. (b) X-ray photoelectron spectroscopy (XPS) Cu 2p of the synthesized Cu-$Sn_{0.03}$ (C) X-ray photoelectron spectroscopy (XPS) Sn 3d of the synthesized Cu-$Sn_{0.03}$

5.3.1.4. Inductively Coupled Plasma Optical emission spectrometry (ICP-OES)

To determine the bulk composition of the Cu-$Sn_{0.03}$ alloy electrocatalyst, a combination of etching and ion analysis using Inductively Coupled Plasma Optical Emission Spectrometry (ICP-OES) was employed. The electrocatalyst sample was subjected to an etching process to remove surface layers and expose the bulk material, followed by dissolution in an appropriate acid solution. The resulting solution was introduced into the ICP-OES instrument, where the sample was atomized and ionized in a high-temperature argon plasma. By comparing the measured

intensities of emitted light to calibration standards, the concentrations of copper and tin in the bulk of the Cu-$Sn_{0.03}$ electrocatalyst were accurately quantified. The ICP-OES results revealed a Cu:Sn ratio of 1:0.028, confirming the desired composition of the alloy electrocatalyst. This bulk composition analysis provides valuable information about the overall stoichiometry of the Cu-$Sn_{0.03}$ electrocatalyst, complementing the surface-sensitive techniques such as XPS and EDS.

Table 5.1 presents the composition analysis results of the synthesized Cu-Snx electrocatalyst nanoparticles obtained by ICP-OES and XPS techniques, comparing the elemental composition of the undoped Cu electrocatalyst and the Cu-$Sn_{0.03}$ electrocatalyst. The ICP-OES results show a Cu concentration of 56.25 ppm for the undoped Cu electrocatalyst, with no detectable Sn, consistent with the XPS results. For the Cu-$Sn_{0.03}$ electrocatalyst, the ICP-OES analysis reveals a Cu concentration of 40.94 ppm and a Sn concentration of 1.16 ppm, resulting in a $CuSn_x$ (x) ratio of 0.028, in close agreement with the intended Cu:Sn ratio of 1:0.03. The XPS results for the Cu-$Sn_{0.03}$ electrocatalyst show an atomic percentage of 50.96% for Cu and 1.64% for Sn, corresponding to a $CuSn_x$ (x) ratio of 0.032. The agreement between the ICP-OES and XPS results for the Cu-$Sn_{0.03}$ electrocatalyst confirms the successful incorporation of tin into the Cu lattice and the homogeneous distribution of the elements throughout the material.

Table 5.1. Composition analysis results of synthesized Cu-Sn_x electrocatalyst nanoparticles obtained by ICP-OES and XPS techniques.

	ICP-OES			XPS		
Electrocatalyst	Cu concentration (μM)	Sn concentration (μM)	$CuSn_x$ (x)	Cu (%)	Sn (%)	$CuSn_x$ (x)
Cu	56.25	-	-	100	-	-
Cu-$Sn_{0.03}$	40.94	1.16	0.028	50.96	1.64	0.032

5.3.2. Electrochemical performance

5.3.2.1. Comparison of electrochemical CO_2 reduction performance: Cu-$Sn_{0.03}$ vs. pure Cu electrode.

The electrochemical performance of the Cu-$Sn_{0.03}$ electrocatalyst (resistivity ~ 2.37 μΩ cm) was evaluated and compared to that of the pure Cu electrode (resistivity ~ 2.30 μΩ cm) in the electrochemical reduction of CO_2 at a cell potential of 4 V. The pure Cu electrode exhibited a current density of 188 mA cm^{-2}, with a diverse product distribution. Ethylene (C_2H_4) was the primary product at 37% Faradaic efficiency, followed by CO (13%), H_2 (17%), and ethanol (11%). The formation of C_{2+} products (ethylene, ethanol, and acetate) accounted for a total Faradaic efficiency of 53%.

In comparison, the Cu-$Sn_{0.03}$ electrocatalyst exhibited a slightly lower current density of 171 mA cm^{-2} but demonstrated a notable shift in product distribution, with increased selectivity towards ethanol (24% Faradaic efficiency) and suppressed ethylene formation (24% Faradaic efficiency). The Faradaic efficiencies for CO and H_2 showed slight changes, with CO increasing to 18% and H_2 decreasing to 9%. The total Faradaic efficiency for C_{2+} products on the Cu-$Sn_{0.03}$ electrocatalyst reached 56%. The enhanced selectivity towards ethanol on the Cu-$Sn_{0.03}$ electrocatalyst is attributed to the modulation of the electronic structure and binding strengths of key reaction intermediates upon tin incorporation, favoring the formation of oxygenated products while hindering the competing hydrogen evolution reaction (HER). These findings highlight the potential of the Cu-$Sn_{0.03}$ electrocatalyst as an efficient and selective catalyst for the production of ethanol from CO_2 reduction and provide insights into the design of advanced Cu-based electrocatalysts.

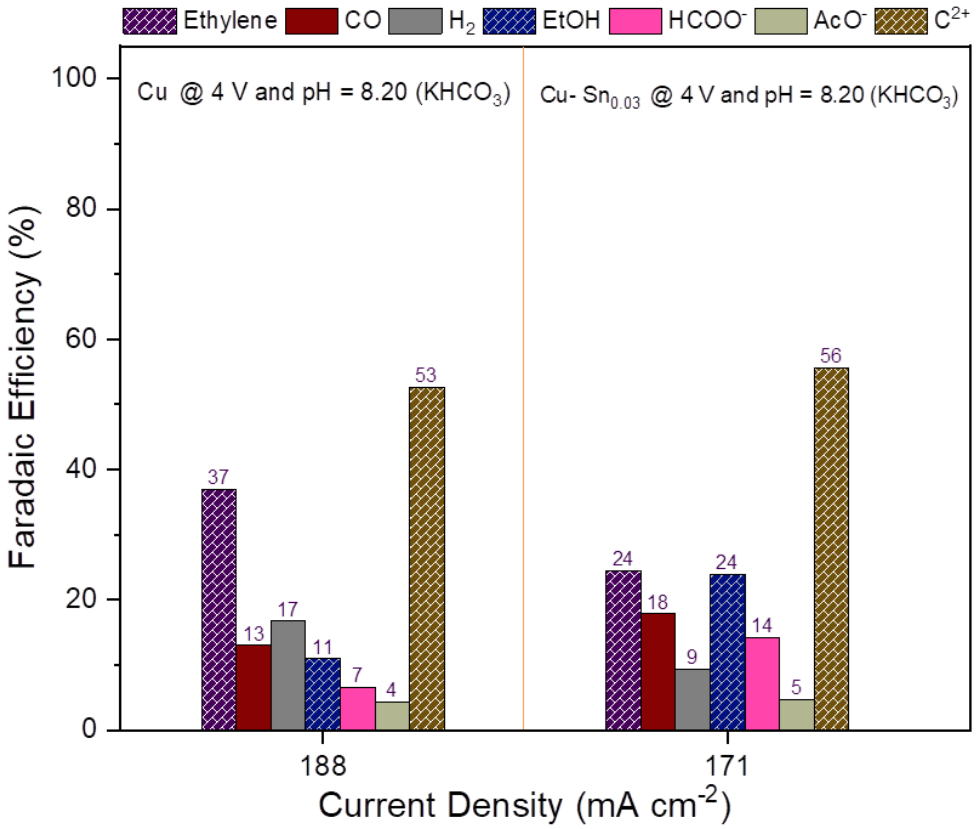

Figure 5.4. Faradaic efficiencies of CO_2 reduction products and current density at a constant cell potential of 4.0 V (Left) Pure Cu and (Right) Cu-$Sn_{0.03}$

5.3.2.2. Impact of pH

The Cu-$Sn_{0.03}$ electrocatalyst demonstrates a notable shift in product selectivity towards ethanol compared to the undoped Cu electrocatalyst, with the effect being more pronounced in alkaline electrolytes. The incorporation of tin into the copper lattice modifies the electronic structure and binding energies of key reaction intermediates, favoring the formation of ethanol over other products. The impact of electrolyte pH on the performance of the Cu-$Sn_{0.03}$ electrocatalyst was investigated by comparing its behavior in weak alkaline (0.1 M $KHCO_3$, pH 8.2) and strong alkaline (1 M KOH, pH 14) electrolytes at a constant cell potential of 4.0 V. In

weak alkaline 0.1 M $KHCO_3$ electrolyte, the Cu-$Sn_{0.03}$ electrocatalyst achieved an ethanol Faradaic efficiency (FE) of 24%, which was 2.2 times higher than that of the undoped Cu electrocatalyst. When the electrolyte was changed to the more alkaline 1 M KOH, the Cu-$Sn_{0.03}$ electrocatalyst exhibited a remarkable increase in ethanol selectivity, achieving an impressive ethanol FE of 48% at a cell potential of 4.0 V, making it the primary product under these conditions. The alkaline medium also promotes the formation of oxygenated products, as the increased concentration of OH- ions facilitates the protonation of adsorbed intermediates and the formation of C-O bonds. The pronounced selectivity shift towards ethanol in the alkaline electrolyte highlights the synergistic effect of tin incorporation and electrolyte pH on the performance of the Cu-$Sn_{0.03}$ electrocatalyst.

The combination of the modified electronic structure induced by tin and the favorable reaction environment provided by the alkaline medium creates optimal conditions for the selective formation of ethanol from CO_2 reduction. The increased stability of the Cu^+ species and the enhanced stabilization of key intermediates in the alkaline electrolyte work in tandem with the catalytic properties of the Cu-$Sn_{0.03}$ electrocatalyst to promote the efficient and selective production of ethanol. The Cu-$Sn_{0.03}$ electrocatalyst demonstrates a remarkable sensitivity to electrolyte pH, with alkaline conditions greatly enhancing its selectivity towards ethanol production. While the Cu-$Sn_{0.03}$ electrocatalyst shows improved ethanol selectivity compared to the undoped Cu electrocatalyst in both neutral and alkaline media, the effect is most pronounced in the 1 M KOH electrolyte, where ethanol becomes the primary product with an FE of 48%. These findings underscore the importance of considering both catalyst composition and electrolyte conditions when designing efficient and selective CO_2 reduction systems. The Cu-$Sn_{0.03}$ electrocatalyst, in combination with an alkaline electrolyte, represents a promising approach for

the selective production of ethanol from CO_2, paving the way for the development of sustainable processes for the valorization of this abundant greenhouse gas.

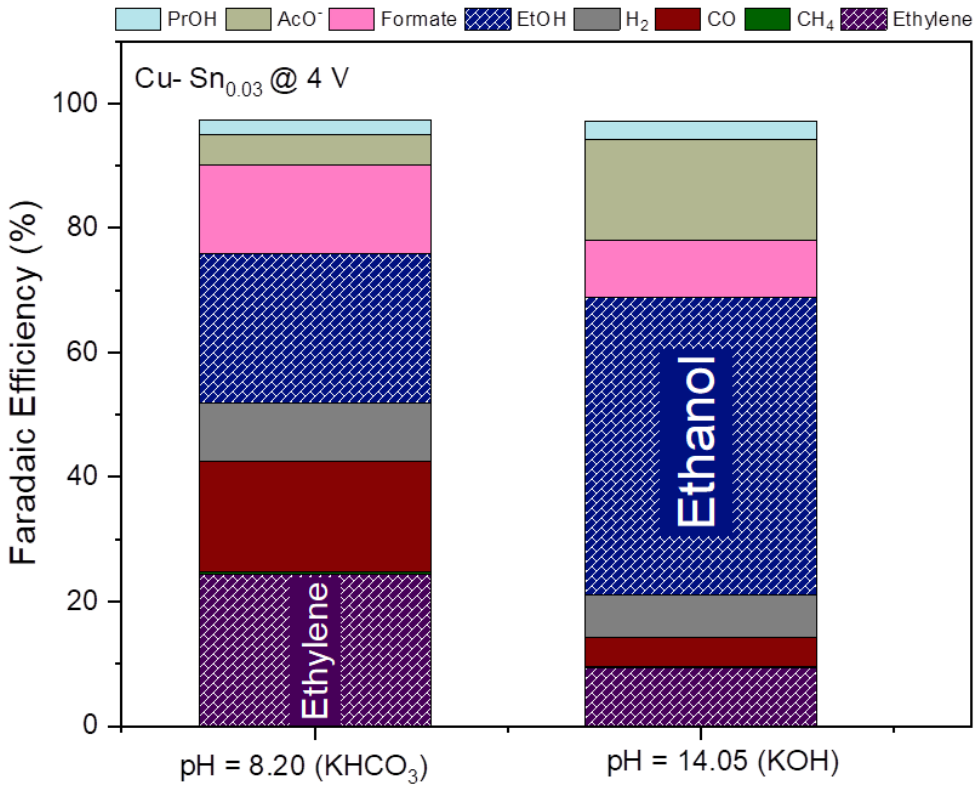

Figure 5.5. Faradaic efficiencies of CO_2 reduction products on Cu-$Sn_{0.03}$ electrocatalysts at a constant cell potential of 4.0 V (Left) 0.1 M $KHCO_3$ (pH = 8.20) and (Right) 1 M KOH (pH = 14.05).

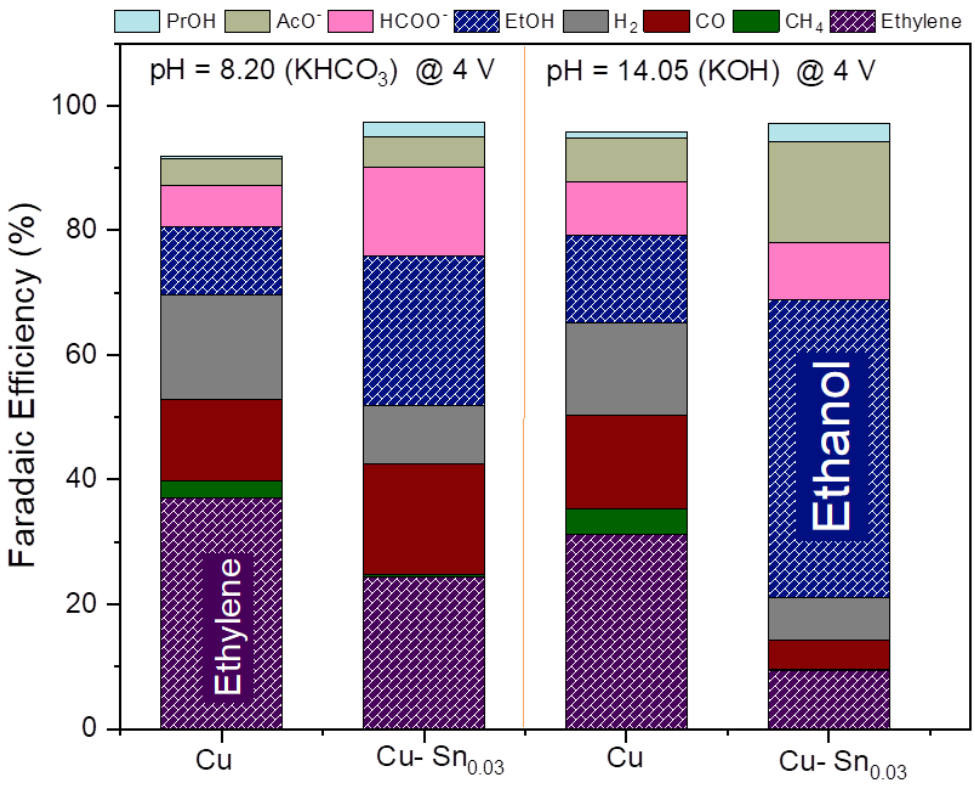

Figure 5.6. Faradaic efficiencies of CO_2 reduction products on pure Cu and Cu-$Sn_{0.03}$ electrocatalysts at a constant cell potential of 4.0 V (Left) 0.1 M $KHCO_3$ (pH = 8.20) and (Right) 1 M KOH (pH = 14.05).

5.3.2.3. Impact of Potential

The impact of potential on the performance of the Cu-$Sn_{0.03}$ electrocatalyst for CO_2 reduction was investigated by varying the cell potential from 3.6 to 4.6 V vs RHE in a 0.1 M $KHCO_3$ electrolyte (pH 8.2). At a cell potential of 3.6 V, the Cu-$Sn_{0.03}$ electrocatalyst exhibited a current density of 150 mA cm^{-2}. The primary products were CO (30% FE), ethylene (24% FE), and ethanol (13% FE), followed by formate (13% FE), hydrogen (8% FE), acetate (3% FE), propanol (3% FE), and methane (2% FE). As the cell potential was increased to 4.0 V, the current

density increased to 171 mA cm^{-2}. The product distribution showed a notable shift, with ethanol becoming the primary product (24% FE), followed by ethylene (24% FE), CO (18% FE), formate (14% FE), hydrogen (9% FE), acetate (5% FE), and propanol (2% FE). Methane production was not observed at this potential.

Further increasing the cell potential to 4.6 V led to a higher current density of 201 mA cm^{-2}. The product distribution remained relatively stable compared to 4.0 V, with ethylene (25% FE) and ethanol (21% FE) being the primary products. The FEs of CO (19% FE), formate (18% FE), and hydrogen (10% FE) showed slight changes, while acetate (2% FE) and propanol (1% FE) decreased. Methane production was observed at this potential with an FE of 1%. The stable performance and product distribution of the Cu-$Sn_{0.03}$ electrocatalyst across the investigated potential range can be attributed to the robustness of the tin-modified Cu surface. The incorporation of tin into the Cu lattice creates a stable surface structure that maintains its selectivity towards ethylene and ethanol production, even at higher potentials. The slight increase in hydrogen evolution at 4.6 V can be explained by the increased rate of the competing HER at more negative potentials.

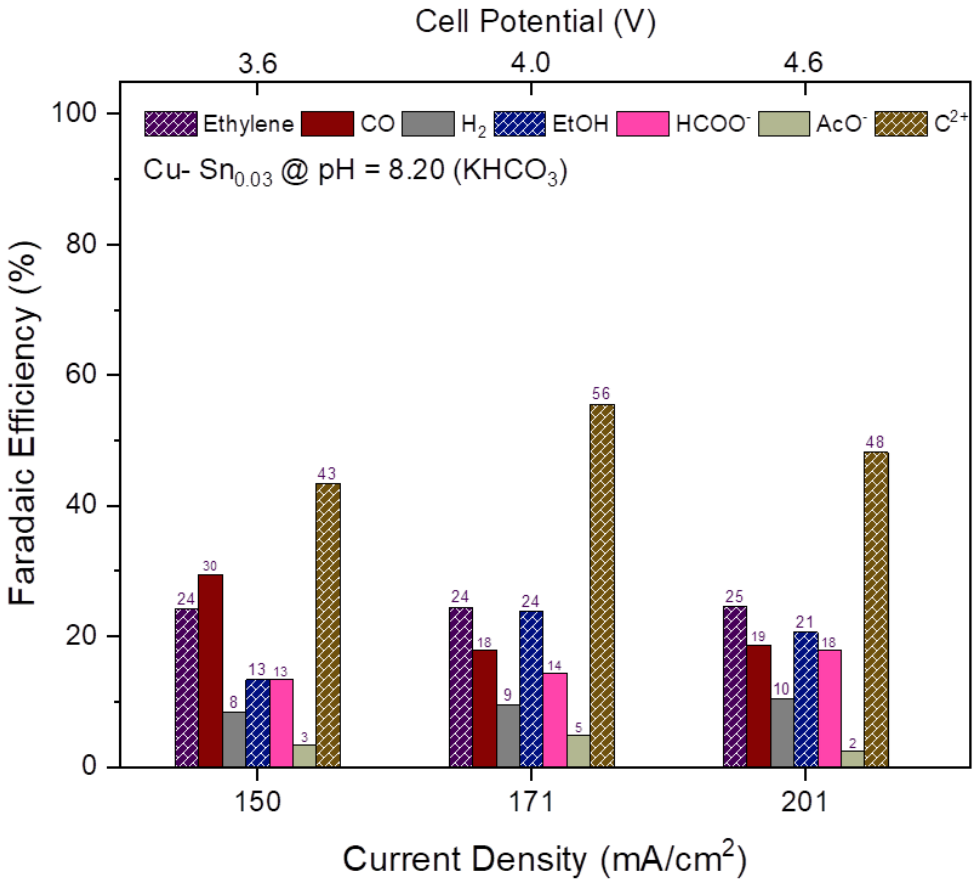

Figure 5.7. Faradaic efficiencies of CO_2 reduction products and current density at varied cell potentials from 3.6 V to 4.6 V for Cu-$Sn_{0.03}$

5.3.2.4. Comparison of Cu-$Sn_{0.03}$ with Previously Reported Cu-Sn Electrocatalysts

The Cu-$Sn_{0.03}$ electrocatalyst developed in this work has demonstrated remarkable performance in the selective electrochemical reduction of CO_2 to ethanol, surpassing the achievements of previously reported Cu-Sn_x electrocatalysts. To highlight the significant advancements made with the Cu-$Sn_{0.03}$ electrocatalyst, it is essential to compare its performance with other notable Cu-Sn_x electrocatalysts reported in the literature.

One prominent example is the Cu_3Sn electrocatalyst, which has shown high selectivity and activity towards ethanol production. In a study by Li et al.(M. Li et al., 2023) the Cu_3Sn

electrocatalyst achieved a faradaic efficiency of 64% for ethanol at a current density of 6 mA cm^{-2}. This impressive selectivity towards ethanol highlights the potential of Cu-Sn alloy catalysts for the efficient conversion of CO_2 to valuable oxygenated products. Furthermore, the same Cu3Sn electrocatalyst demonstrated a faradaic efficiency of 40% for ethanol at a remarkably high current density of 900 mA cm^{-2}, indicating its ability to maintain good selectivity even at elevated reaction rates. These results underscore the effectiveness of the Cu_3Sn electrocatalyst in promoting the formation of ethanol from CO_2 reduction.

In comparison to these previously reported Cu-Sn_x catalysts, the Cu-$Sn_{0.03}$ electrocatalyst developed in this work has achieved a new record in terms of ethanol selectivity and current density. At a cell potential of 4.0 V and in a neutral 0.1 M $KHCO_3$ electrolyte, the Cu-$Sn_{0.03}$ electrocatalyst reached a faradaic efficiency of 23% for ethanol at a current density of 150 mA cm^{-2}. This result surpasses the performance of the $CuSn_{0.025}$ electrocatalyst, demonstrating the Cu-$Sn_{0.03}$ electrocatalyst's ability to achieve high ethanol selectivity at a significantly higher current density. Moreover, when the electrolyte was changed to the more alkaline 1 M KOH, the Cu-Sn0.03 electrocatalyst's performance was further enhanced, achieving a remarkable faradaic efficiency of 48% for ethanol at an even higher current density of 350 mA cm^{-2}. This exceptional performance in alkaline media highlights the synergistic effect of the Cu-$Sn_{0.03}$ composition and the favorable reaction environment provided by the alkaline electrolyte. The Cu-$Sn_{0.03}$ electrocatalyst's ability to maintain high ethanol selectivity at such high current densities sets a new benchmark for Cu-Sn_x electrocatalysts and demonstrates its potential for efficient and scalable CO_2 electroreduction to ethanol.

The comparison of the Cu-$Sn_{0.03}$ electrocatalyst with previously reported Cu-Sn_x electrocatalysts highlights the significant advancements made in this work. The Cu-$Sn_{0.03}$

electrocatalyst's record-breaking performance, achieving high ethanol selectivity at elevated current densities, surpasses the achievements of other notable Cu-Sn_x electrocatalysts. This breakthrough in ethanol production from CO_2 reduction can be attributed to the optimal composition of the Cu-$Sn_{0.03}$ electrocatalyst, the favorable reaction environment provided by the alkaline electrolyte, and the synergistic effects of these factors on the catalytic properties. These findings underscore the importance of catalyst design and electrolyte engineering in developing efficient and selective CO_2 reduction systems and pave the way for the scalable production of ethanol from CO_2, contributing to the development of sustainable technologies for the valorization of this abundant greenhouse gas.

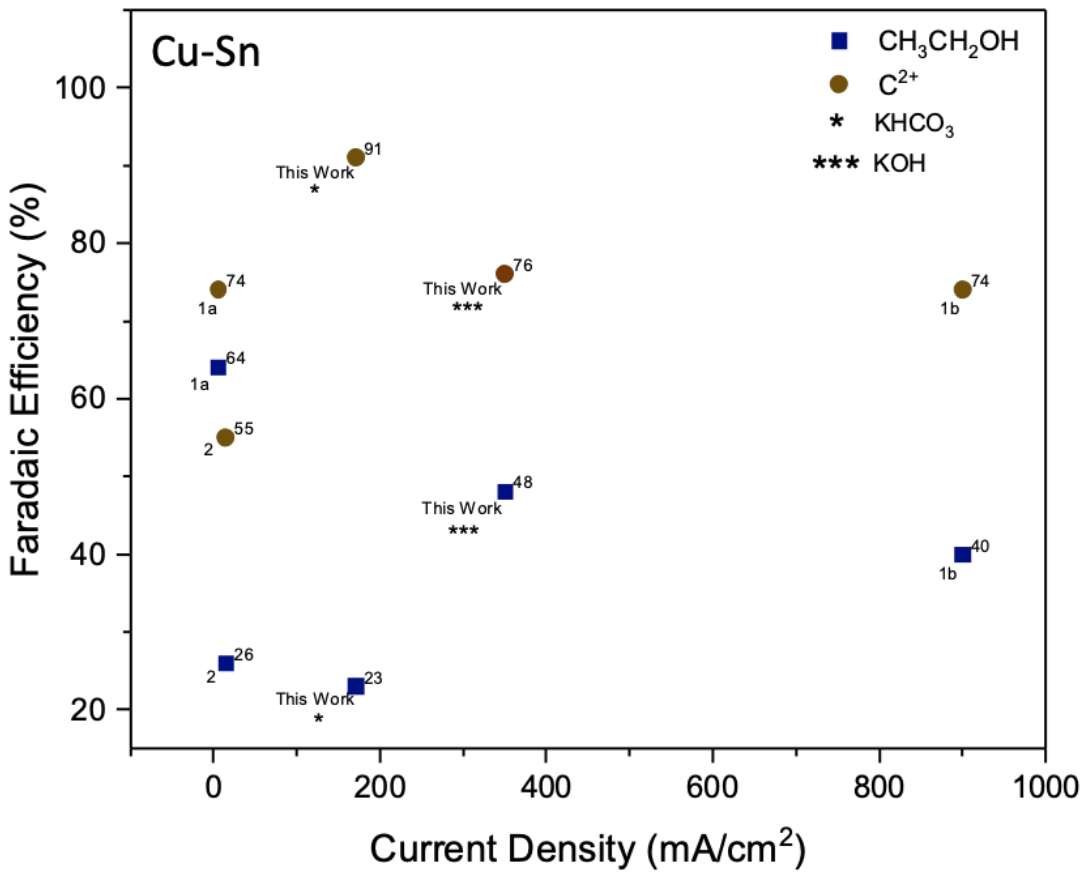

Figure 5.8. Comparison of Cu-Sn_x with previously reported Cu-Sn_x catalysts. (1) Cu_3Sn electrocatalyst exhibits high selectivity and activity towards ethanol production, with a faradaic efficiency of (1a) 64% at a current density of 6 mA cm^{-2} and (1b) 40% at a current density of -900 mA cm^{-2}.(Shang et al., 2022) (2) The $CuSn_{0.025}$ catalyst achieved the highest faradaic efficiency for ethanol, reaching 25.93% at -1.4 V RHE, accompanied by a substantial partial current density of 15.05 mA cm^{-2}. (M. Li et al., 2023)

5.4. Discussion

The Cu-$Sn_{0.03}$ electrocatalyst developed in this work has demonstrated remarkable performance in the selective electrochemical reduction of CO_2 to ethanol, surpassing the achievements of previously reported Cu-Sn_x electrocatalysts. The comprehensive characterization of the Cu-$Sn_{0.03}$ electrocatalyst using advanced techniques such as SEM, EDS, XRD, XPS, and ICP-OES has provided valuable insights into its structural, compositional, and electronic properties. The SEM and EDS analyses revealed the spherical morphology and uniform

distribution of Cu and Sn in the Cu-$Sn_{0.03}$ nanoparticles, while the XRD results confirmed the expansion of the Cu lattice upon Sn incorporation. The XPS and ICP-OES studies elucidated the electronic structure, oxidation states, and bulk composition of the Cu-$Sn_{0.03}$ electrocatalyst, highlighting the successful incorporation of Sn into the Cu lattice.

The electrochemical performance of the Cu-$Sn_{0.03}$ electrocatalyst was evaluated and compared to that of the pure Cu electrode, demonstrating the impact of Sn incorporation on the catalytic activity and selectivity. The Cu-$Sn_{0.03}$ electrocatalyst exhibited a notable shift in product distribution, with increased selectivity towards ethanol and suppressed ethylene formation. The enhanced ethanol selectivity was attributed to the modulation of the electronic structure and binding energies of key reaction intermediates upon Sn incorporation. The impact of electrolyte pH on the Cu-$Sn_{0.03}$ electrocatalyst's performance was also investigated, revealing a remarkable sensitivity to alkaline conditions. In 1 M KOH electrolyte, the Cu-$Sn_{0.03}$ electrocatalyst achieved an impressive ethanol Faradaic efficiency of 48% at a high current density of 350 mA cm^{-2}, surpassing the performance of previously reported Cu-Sn_x electrocatalysts.

The comparison of the Cu-$Sn_{0.03}$ electrocatalyst with other notable Cu-Sn_x electrocatalysts, such as Cu_3Sn and $CuSn_{0.025}$, highlights the significant advancements made in this work. The Cu-$Sn_{0.03}$ electrocatalyst's ability to achieve high ethanol selectivity at elevated current densities sets a new benchmark for Cu-Sn_x electrocatalysts and demonstrates its potential for efficient and scalable CO_2 electroreduction to ethanol. The breakthrough performance of the Cu-$Sn_{0.03}$ electrocatalyst can be attributed to the optimal composition, favorable reaction environment provided by the alkaline electrolyte, and the synergistic effects of these factors on the catalytic properties. These findings underscore the importance of catalyst design and electrolyte engineering in developing efficient and selective CO_2 reduction systems.

5.5. Conclusion

In conclusion, this work presents the development and comprehensive characterization of a novel Cu-$Sn_{0.03}$ electrocatalyst for the selective electrochemical reduction of CO_2 to ethanol. The Cu-$Sn_{0.03}$ electrocatalyst, synthesized through a facile one-pot method, exhibits a spherical morphology, uniform distribution of Cu and Sn, and an expanded Cu lattice due to Sn incorporation. The electrochemical performance of the Cu-$Sn_{0.03}$ electrocatalyst surpasses that of the pure Cu electrode and previously reported Cu-Sn_x electrocatalysts, achieving a remarkable ethanol Faradaic efficiency of 48% at a high current density of 350 mA cm^{-2} in an alkaline electrolyte.

The enhanced selectivity towards ethanol on the Cu-$Sn_{0.03}$ electrocatalyst is attributed to the modulation of the electronic structure and binding energies of key reaction intermediates upon Sn incorporation. The synergistic effect of the Cu-$Sn_{0.03}$ composition and the favorable reaction environment provided by the alkaline electrolyte creates optimal conditions for the selective formation of ethanol from CO_2 reduction. The Cu-$Sn_{0.03}$ electrocatalyst's ability to maintain high ethanol selectivity at elevated current densities demonstrates its potential for efficient and scalable CO_2 electroreduction to ethanol.

This work highlights the importance of catalyst design and electrolyte engineering in developing efficient and selective CO_2 reduction systems. The Cu-$Sn_{0.03}$ electrocatalyst represents a promising approach for the valorization of CO_2 into value-added chemicals and fuels, contributing to the development of sustainable technologies for carbon utilization. Further research on the fundamental understanding of the reaction mechanisms, optimization of the catalyst composition and structure, and exploration of advanced electrolyte systems will pave the way for the industrial-scale production of ethanol from CO_2 electroreduction.

CHAPTER 6. REDUCTION OF CO_2 AT COPPER-SELENIDE

6.1. Introduction

The electrochemical reduction of CO_2 is a promising approach to mitigate rising atmospheric CO_2 levels and produce value-added chemicals and fuels. Cu has been widely investigated as an electrocatalyst for CO_2 reduction due to its ability to generate a wide range of products, including hydrocarbons and oxygenated compounds. However, the selectivity and efficiency of Cu electrocatalysts towards desired products, such as C_{2+} hydrocarbons and alcohols, remain challenging. (Costentin et al., 2013; Feaster et al., 2017)

Oxide-derived copper (OD-Cu) catalysts have gained significant attention due to their highly selective production of C_2 products and their simple preparation methods. Lee et al. .(Kim et al., 2015; Lee et al., 2015) observed that the presence of a Cu_2O layer on the catalyst surface enhanced the selectivity for C_2H_4 production compared to metallic Cu electrodes during cathodic CO_2 reduction. This finding highlighted the crucial role of $Cu^{\delta+}$ in guiding the CO_2 reduction pathway towards efficient C_{2+} product generation. (Wu et al., 2021; Zhang et al., 2020) Although Cu^+ species on OD-Cu catalysts are generally believed to be easily reduced to metallic Cu under cathodic potentials, recent studies have shown that a significant portion of these Cu^+ species can be surprisingly resistant to electrochemical reduction during CO_2 reduction.(Mistry et al., 2016)

In situ X-ray absorption spectroscopy (XAS) measurements on an O2-plasma-activated Cu catalyst during CO_2 reduction revealed that Cu^+ species could persist for at least 15 minutes after applying a potential of -1.2 V vs. RHE.(De Luna et al., 2018) These in situ XAS studies quantified the time-dependent reduction behavior, showing that the initial 84% Cu^+ on the electrocatalyst surface decreased to 77% Cu^+ after 10 minutes of CO_2 reduction at -1.2 V vs. RHE. Remarkably, approximately 23% of Cu^+ remained even after 1 hour at the same cathodic potential,(De Luna et

al., 2018) highlighting the unexpected stability of these oxidized species under reducing conditions. However, the instability of $Cu^{\delta+}$ active sites during CO_2 reduction and their susceptibility to in situ self-reduction after a few hours present significant challenges in maintaining high CO_2 reduction activity, particularly under high current densities. (Fang et al., 2023)

To address the limitations of OD-Cu catalysts, we propose the use of copper selenide (Cu_2Se) as an alternative electrocatalyst for CO_2 reduction. Selenide's higher electronegativity compared to sulfur and greater electron-withdrawing ability relative to boron, along with its larger atomic radius, facilitate effective alloying and stabilization of Cu^+ species.(D. Yang et al., 2019) Copper selenide nanocatalysts have demonstrated outstanding performance in CO_2 reduction to methanol and selective generation of carbon-rich C_2 products. (Ding et al., 2022; Saxena et al., 2021)

In this work, we investigate the electrocatalytic performance of Cu_2Se nanoparticles for CO_2 reduction, aiming to unravel the underlying mechanisms and identify key factors that govern catalytic performance. The development of stable and selective Cu_2Se electrocatalysts has the potential to overcome the limitations of OD-Cu catalysts and contribute to the efforts in developing advanced electrocatalysts for efficient and sustainable CO_2 conversion. By leveraging the unique properties of copper selenide, we aim to address the challenges associated with the stability and selectivity of Cu-based catalysts and explore new avenues for the electrochemical valorization of CO_2.

6.2. Experimental

6.2.1. Synthesis of electrocatalyst

Copper selenide (Cu_2Se) nanoparticles were synthesized using a colloidal approach adapted from previous studies. The synthesis process involved the dissolution of elemental selenium in a sodium hydroxide solution, followed by the addition of a copper chloride solution and the reduction of the resulting mixture with hydrazine hydrate. Specifically, 5 mmol of elemental selenium powder was dispersed in a sodium hydroxide solution prepared by dissolving 10 mmol of NaOH in 50 mL of deionized water. The mixture was stirred vigorously until the selenium powder completely dissolved, resulting in an orange-red solution. This step led to the formation of sodium selenide (Na_2Se), which served as the selenium precursor for the synthesis of copper selenide nanoparticles.

In a separate beaker, a copper chloride solution was prepared by dissolving 10 mmol of copper (II) chloride dihydrate ($CuCl_2 \cdot 2H_2O$) in 50 mL of deionized water. The copper chloride solution was then added dropwise to the sodium selenide solution under rapid stirring. Upon mixing, the color of the solution immediately changed from orange-red to dark brown, indicating the formation of copper selenide nanoparticles. To ensure complete reduction of the copper ions and promote the growth of uniform nanoparticles, 3 mL of hydrazine hydrate ($N_2H_4 \cdot H_2O$) was injected into the reaction mixture. Hydrazine hydrate acted as a strong reducing agent, facilitating the reduction of Cu^{2+} to Cu^{+} and the subsequent formation of Cu_2Se nanoparticles. The reaction mixture was then subjected to stirring and heating at 80 °C for 3 hours to allow for the growth and crystallization of the nanoparticles.

After the reaction was complete, the black precipitate of Cu_2Se nanoparticles was collected by centrifugation at 8000 rpm for 10 minutes. The nanoparticles were then washed several times

with deionized water and ethanol to remove any unreacted precursors and impurities. The washing step was repeated until the supernatant became clear, ensuring the purity of the synthesized nanoparticles. Finally, the washed Cu_2Se nanoparticles were dried in a vacuum oven at 150 °C for 24 hours to remove any residual moisture and solvents. The high drying temperature and prolonged drying time were essential to ensure the complete removal of water and to promote the formation of a stable, crystalline structure. The resulting Cu_2Se nanoparticles were stored in an airtight container until further use. This colloidal synthesis approach allowed for the preparation of high-quality Cu_2Se nanoparticles with controlled size and composition, which were subsequently employed as electrocatalysts for the electrochemical reduction of carbon dioxide.

6.2.2. Characterization

A comprehensive characterization of the Cu_2Se electrocatalyst was performed using a combination of advanced analytical techniques. X-ray photoelectron spectroscopy (XPS) was employed to investigate the surface chemical states and elemental composition using a ScientaOmicron XPS system. By analyzing the binding energies and peak intensities of the Cu 2p and Se 3d core levels, the oxidation states and relative abundances of Cu and Se on the surface were determined. The XPS results provide valuable insights into the electronic structure of the Cu_2Se nanoparticles and the nature of the Cu-Se interactions at the surface. Scanning Electron Microscopy (SEM) coupled with Energy Dispersive X-ray Spectroscopy (EDS) was utilized to examine the morphology, microstructure, and elemental distribution using a ThermoFisher PFIBSEM system. SEM micrographs provide information about the size, shape, and surface features of the Cu_2Se nanoparticles, while EDS allows for the mapping of the elemental composition across the sample surface, providing insights into the homogeneity of the Cu_2Se composition.

To determine the bulk composition and crystal structure, X-ray diffraction (XRD) and inductively coupled plasma optical emission spectrometry (ICP-OES) were employed. XRD analysis was performed using a PANalytical X'Pert Pro diffractometer with Cu Kα radiation, collecting patterns over a 2θ range of 20-80°. The obtained XRD patterns were compared with standard reference patterns to identify the crystal structure and phase purity of the Cu2Se nanoparticles, providing information about lattice parameters, crystallite size, and potential impurities. ICP-OES analysis was performed using an Agilent 720ES spectrometer, after acid digestion of the electrocatalyst sample. By comparing the intensities of the emitted light to calibration standards, the concentrations of Cu and Se in the bulk were accurately quantified, providing a precise determination of the Cu:Se ratio and verifying the stoichiometry of the Cu_2Se phase. The combination of XRD and ICP-OES analyses provides a comprehensive understanding of the crystal structure and composition of the Cu_2Se electrocatalyst.

6.2.3. Electrode preparation

The preparation of the cathode electrode for the Cu_2Se electrocatalyst was carried out using a spray-coating technique. First, an electrocatalyst slurry was prepared by mixing approximately 100 mg of the synthesized Cu_2Se nanoparticles, 5 mg of Vulcan Carbon, and 5.53 mg of polyvinylidene fluoride (PVDF) powder in 20 mL of a 1:1 H_2O-isopropanol solution. The addition of Vulcan Carbon serves to improve the electrical conductivity of the electrode, while PVDF acts as a binder to ensure adhesion of the electrocatalyst to the gas diffusion layer. The slurry was then subjected to sonication for 1 hour to achieve a homogeneous dispersion of the components, resulting in a stable and well-mixed electrocatalyst ink. After sonication, the electrocatalyst ink was sprayed onto a 50 cm2 microporous hydrophobic side of a gas diffusion carbon paper (Sigracet 39BB) using a spray gun. The spraying process was performed in a controlled manner to ensure

uniform coverage of the electrocatalyst on the carbon paper surface. The loading of the Cu_2Se electrocatalyst on the cathode was precisely monitored using a balance, and the spraying process was continued until a loading of 1 mg cm-2 was achieved. This optimized loading ensures sufficient catalytic activity while maintaining good gas diffusion properties of the electrode.

For the preparation of the anode electrode, a dip-coating method followed by thermal decomposition was employed to deposit an iridium oxide (IrO_2) catalyst layer on a titanium felt substrate. The titanium felt, with a geometrical area of 6.64 cm^2, was first subjected to an etching treatment to improve its surface roughness and adhesion properties. The etching process involved immersing the titanium felt in a boiling 0.5 M oxalic acid solution for 30 minutes. This step helps to remove any surface impurities and creates a more porous and reactive surface for the subsequent catalyst deposition. After etching, the titanium felt was thoroughly rinsed with deionized water to remove any residual oxalic acid. The etched titanium felt was then dip-coated in a solution containing 75 mg of iridium (IV) chloride hydrate ($IrCl_4 \cdot xH_2O$) dissolved in a mixture of 6.76 mL of 37% hydrochloric acid (HCl) and 18.24 mL of isopropanol. The dip-coating process ensures a uniform distribution of the iridium precursor on the surface of the titanium felt. After the dip-coating step, the titanium felt coated with $IrCl_4$ was dried in an oven at 100 °C for 20 minutes to remove any residual solvents. Subsequently, the dried electrode was subjected to a calcination treatment at 500 °C for 20 minutes in air. During the calcination process, the $IrCl_4$ precursor undergoes thermal decomposition, resulting in the formation of a highly active and stable IrO_2 catalyst layer on the surface of the titanium felt. To achieve the desired catalyst loading of 3 mg cm^{-2}, the dip-coating and calcination process was repeated multiple times. The loading of the IrO_2 catalyst was carefully controlled to optimize the anode performance while maintaining the porous structure of the titanium felt for efficient gas and liquid transport. The resulting IrO_2-coated

titanium felt anode possesses high catalytic activity and stability for the oxygen evolution reaction (OER), which is crucial for the overall performance of the electrochemical CO_2 reduction system.

Prior to assembling the membrane electrode assembly (MEA) electrolyzer cell, the prepared Cu_2Se cathode and IrO_2 anode electrodes were subjected to a conditioning step to ensure optimal performance. The spray-coated Sigracet 39BB cathode was left overnight at room temperature (20 °C) to allow for complete drying of the electrocatalyst layer. This extended drying period ensures the removal of any residual solvent and the formation of a stable and well-adhered Cu_2Se catalyst layer on the gas diffusion electrode (GDE) surface. Similarly, the IrO_2-coated titanium felt anode was allowed to cool down to room temperature after the final calcination step. This cooling period helps to stabilize the IrO_2 catalyst layer and prevent any potential thermal stresses during the assembly process. Once the electrodes were thoroughly dried and conditioned, they were carefully assembled into the custom-made MEA electrolyzer cell. Precise alignment and proper contact between the electrodes and the ion exchange membrane were ensured to maximize the performance and minimize any potential gas leakage. The MEA electrolyzer cell was sealed using an adjustable clamping pressure feature, which allows for the optimization of the membrane-electrode stack sealing without the need for additional gaskets. The adjustable clamping pressure enables uniform compression of the MEA components, promoting excellent electrical contact and minimizing ohmic losses. The well-sealed and properly conditioned MEA electrolyzer cell, featuring the Cu_2Se cathode and IrO_2 anode, was then ready for electrochemical CO_2 reduction experiments.

6.3. Results

6.3.1. Electrocatalyst characterization

6.3.1.1. Scanning Electron Microscope (SEM)

Scanning electron microscopy (SEM) SEM analysis was employed to investigate the morphology and size distribution of the synthesized Cu_2Se electrocatalyst. Figure 5.2(a) presents an SEM image revealing uniformly sized nanoparticles with a spherical morphology and an average diameter of approximately 50 nm. The narrow size distribution and well-defined spherical morphology can be attributed to the precise control over the reaction conditions during the colloidal synthesis approach. The SEM analysis confirms the successful synthesis of Cu_2Se nanoparticles with desirable morphological characteristics, essential for their application as electrocatalysts in CO_2 reduction.

EDS elemental mapping was conducted to investigate the elemental composition and distribution within the Cu_2Se nanoparticles. Figure 5.2(b) and 5.2(c) present the EDS elemental maps of copper and selenium, respectively, revealing a uniform distribution of both elements throughout the nanoparticles. The absence of selenium-rich regions or segregation suggests the formation of a single-phase Cu_2Se compound, with selenium atoms evenly distributed within the copper matrix. The homogeneous distribution of selenium is crucial for achieving the desired electronic and structural properties of the Cu_2Se electrocatalyst, ensuring a consistent modification of the catalytic sites throughout the material. The SEM and EDS characterization results provide valuable insights into the morphology, size, and elemental distribution of the Cu_2Se electrocatalyst, laying the foundation for understanding its enhanced performance in the electrochemical reduction of CO_2.

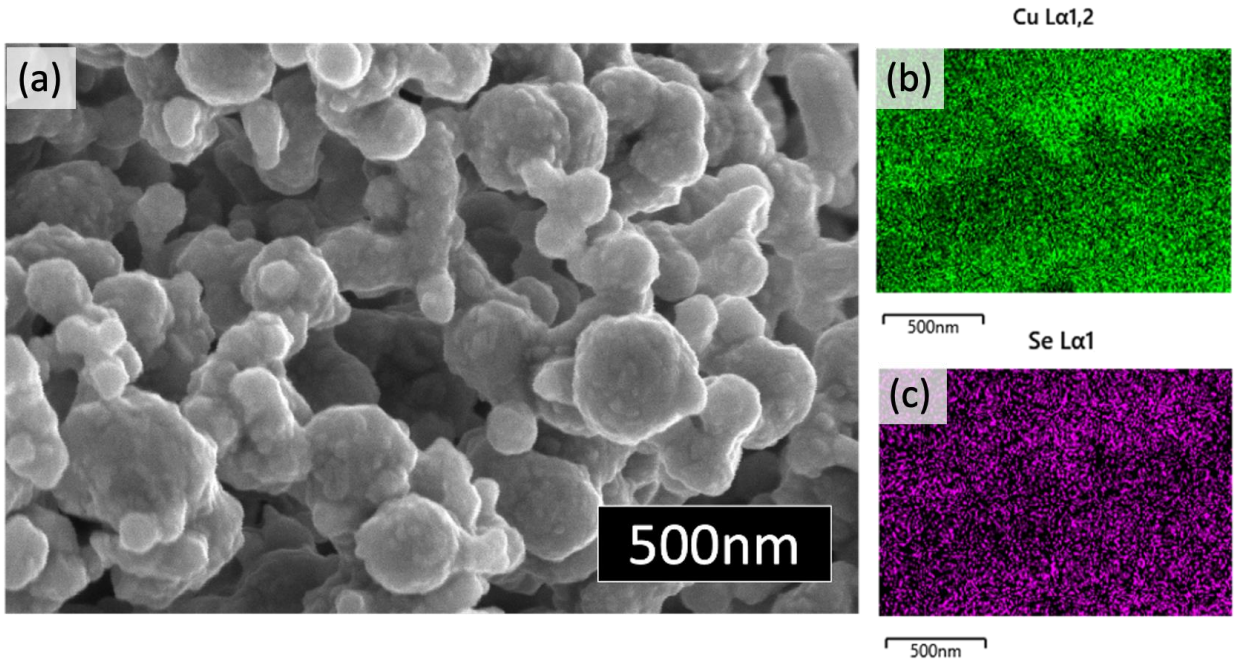

Figure 6.1. (a) Scanning electron microscopy (SEM) image of the synthesized Cu_2Se nanoparticles. (b) Energy dispersive X-ray spectroscopy (EDS) elemental mapping of copper. (c) Energy dispersive X-ray spectroscopy (EDS) elemental mapping of selenium.

6.3.1.2. X-ray diffraction (XRD) Analysis

X-ray diffraction (XRD) is a powerful technique for investigating the crystal structure, phase composition, and lattice parameters of materials. In this study, XRD analyses were conducted to examine the structural phases of the Cu_2Se electrocatalyst before and after its use in the electrochemical reduction of CO_2. Figure 6.2(a) presents the XRD patterns of the synthesized Cu_2Se nanoparticles, revealing the crystalline nature and phase purity of the material. The XRD pattern exhibits sharp and well-defined diffraction peaks, indicating the high crystallinity of the Cu_2Se nanoparticles. The observed diffraction peaks can be indexed to the cubic phase of $Cu_{2-x}Se$ (JCPDS no. 06-0680), confirming the successful formation of the desired Cu_2Se phase during the colloidal synthesis process. The absence of any additional peaks corresponding to impurities or secondary phases demonstrates the phase purity of the synthesized Cu_2Se nanoparticles.

The XRD analysis also provides insights into the stability and structural integrity of the Cu_2Se electrocatalyst under the electrochemical CO_2 reduction conditions. Figure 5.3(b) presents a comparison of the XRD patterns of the Cu_2Se electrocatalyst before and after its use in the CO2 reduction reaction. The XRD pattern of the post-reaction Cu_2Se electrocatalyst closely resembles that of the as-synthesized nanoparticles, indicating the retention of the cubic $Cu_{2-x}Se$ phase and the absence of any significant structural changes or phase transformations during the electrochemical process. The preservation of the crystal structure and phase purity of the Cu_2Se electrocatalyst highlights its stability under the reducing conditions encountered during CO_2 reduction. This stability is crucial for maintaining the catalytic performance and ensuring the long-term durability of the electrocatalyst. The XRD results, as shown in Figure 5.3, provide valuable information about the crystal structure, phase composition, and stability of the Cu_2Se electrocatalyst, laying the foundation for understanding its enhanced catalytic properties in the electrochemical reduction of CO_2.

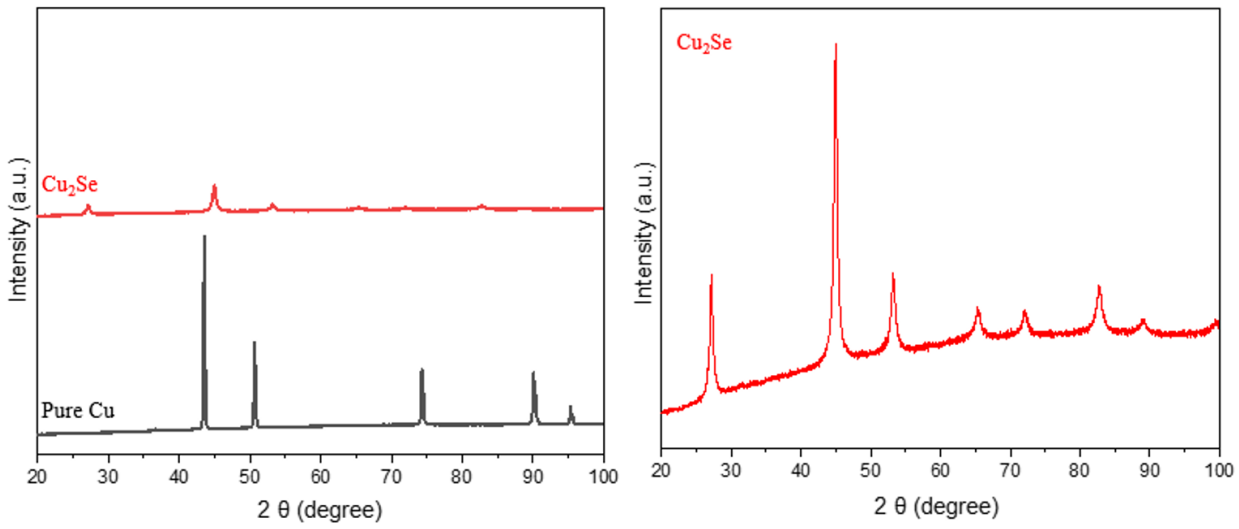

Figure 6.2. (a) X-ray diffraction (XRD) pattern of the synthesized Cu_2Se nanoparticles, confirming the cubic $Cu_{2-x}Se$ phase. (b) Comparison of the XRD patterns of the Cu_2Se electrocatalyst before and after its use in the electrochemical reduction of CO_2, demonstrating the structural stability of the material.

6.3.1.3. X-ray Photoelectron Spectroscopy (XPS) Analysis

X-ray photoelectron spectroscopy (XPS) was employed to investigate the electronic properties and oxidation states of the Cu_2Se electrocatalyst. The XPS survey spectrum (Figure 5.4(a)) confirms the presence of Cu and Se as the main components, along with O and C, which may arise from surface adsorption, or the capping agent used during synthesis. The absence of additional peaks demonstrates the purity of the synthesized Cu_2Se nanoparticles. High-resolution XPS spectra of the Cu 2p region (Figure 5.4(b)) reveal two main peaks at ~932 eV (Cu 2p3/2) and ~952 eV (Cu 2p1/2), characteristic of the Cu oxidation states. The Cu 2p3/2 core level was deconvoluted into two components: Cu^+ at ~932 eV (dominant) and Cu^{2+} at ~934 eV (surface oxidation). The Cu Auger spectrum confirms that before electroreduction, the Cu_2Se electrocatalyst comprises mostly Cu^+ species, in agreement with the expected oxidation state of Cu in Cu_2Se.

High-resolution XPS spectra of the Se 3d region (Figure 5.4(c)) show two prominent peaks at ~54 eV (Se 3d5/2) and ~55 eV (Se 3d3/2), consistent with the Se^{2-} oxidation state in Cu_2Se. The absence of additional peaks or shoulders confirms the phase purity of the synthesized Cu_2Se nanoparticles. The XPS results provide valuable information about the initial electronic structure and oxidation states of the Cu_2Se electrocatalyst, highlighting the predominance of Cu^+ and Se^{2-} species before electroreduction. The successful incorporation of Se into the Cu lattice is crucial for the enhanced catalytic properties of the Cu_2Se electrocatalyst in the electrochemical reduction of CO_2. However, oxidation states may evolve during electroreduction, and in situ characterization

techniques can provide more detailed information about dynamic changes in the electronic structure.

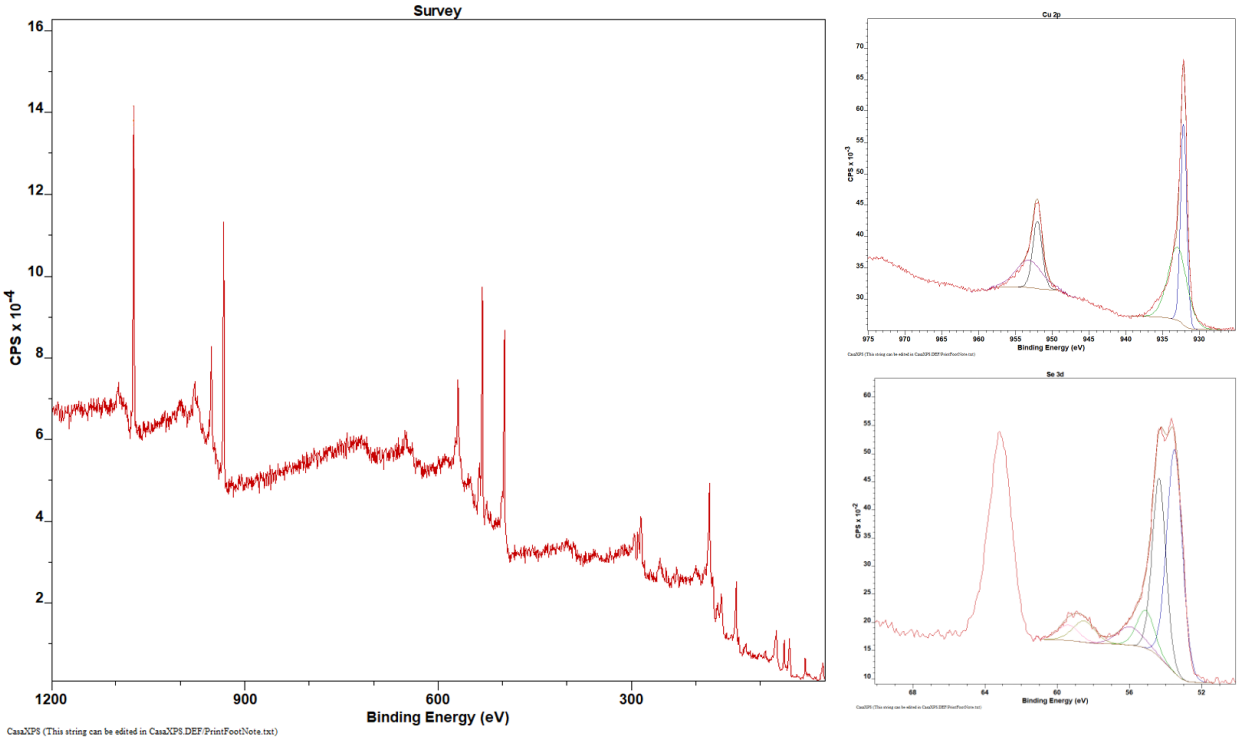

Figure 6.3. (a) XPS survey spectrum of the synthesized Cu_2Se nanoparticles. (b) High-resolution XPS spectrum of the Cu 2p region, showing the predominance of Cu^+ species. (c) High-resolution XPS spectrum of the Se 3d region, confirming the presence of Se^{2-} species in the Cu_2Se electrocatalyst.

6.3.1.4. Inductively Coupled Plasma Optical emission spectrometry (ICP-OES)

To determine the bulk composition of the Cu_2Se electrocatalyst, a combination of etching and ion analysis using Inductively Coupled Plasma Optical Emission Spectrometry (ICP-OES) was employed. The electrocatalyst sample was subjected to an etching process to remove surface layers and expose the bulk material, followed by dissolution in an appropriate acid solution. The resulting solution was introduced into the ICP-OES instrument, where the sample was atomized and ionized in a high-temperature argon plasma. By comparing the measured intensities of emitted light to calibration standards, the concentrations of copper and selenium in the bulk of the Cu_2Se electrocatalyst were accurately quantified. The ICP-OES results revealed a Cu:Se ratio of 1:0.206,

confirming the desired composition of the Cu_2Se electrocatalyst. This bulk composition analysis provides valuable information about the overall stoichiometry of the Cu_2Se electrocatalyst, complementing the surface-sensitive techniques such as XPS and EDS.

Table 5.2 presents the composition analysis results of the synthesized Cu_2Se electrocatalyst nanoparticles obtained by ICP-OES and XPS techniques, comparing the elemental composition of the undoped Cu electrocatalyst and the Cu_2Se electrocatalyst. The ICP-OES results show a Cu concentration of 56.25 ppm for the undoped Cu electrocatalyst, with no detectable Se, consistent with the XPS results. For the Cu_2Se electrocatalyst, the ICP-OES analysis reveals a Cu concentration of 31.76 ppm and a Se concentration of 6.53 ppm, resulting in a $CuSe_x$ (x) ratio of 0.206, in close agreement with the intended Cu:Se ratio of 2:1 for the Cu_2Se phase. The XPS results for the Cu_2Se electrocatalyst show an atomic percentage of 26.91% for Cu and 3.84% for Se, corresponding to a $CuSe_x$ (x) ratio of 0.143. The difference between the bulk composition (ICP-OES) and the surface composition (XPS) can be attributed to the surface sensitivity of the XPS technique, probing only the topmost atomic layers. The ICP-OES and XPS results confirm the successful incorporation of selenium into the copper lattice and the formation of the desired Cu_2Se phase, providing a comprehensive understanding of the elemental distribution and stoichiometry of the Cu_2Se electrocatalyst.

Table 6.1. Composition analysis results of synthesized Cu-Se electrocatalyst nanoparticles obtained by ICP-OES and XPS techniques.

	ICP-OES			XPS		
Electrocatalyst	Cu concentration (μM)	Se concentration (μM)	$CuSe_x$ (x)	Cu (%)	Se (%)	$CuSe_x$ (x)
Cu	56.25	-	-	100	-	-
Cu_2Se	31.76	6.53	0.206	26.91	3.84	0.143

6.3.2. Electrochemical performance

6.3.2.1. Comparison of electrochemical CO_2 reduction performance: Cu_2Se vs. pure Cu electrode

The comparison between the pure copper electrode (resistivity ~ 2.30 μΩ cm) and the Cu_2Se electrocatalyst (resistivity ~ 98.62 μΩ cm) highlights significant differences in their electrochemical performance for CO_2 reduction at a cell potential of 4 V. The pure copper electrode demonstrated a higher overall catalytic activity, with a current density of 188 mA cm^{-2}. However, the product distribution on the pure copper electrode was relatively diverse, with ethylene (C_2H_4) being the primary product at 37% Faradaic efficiency, followed by carbon monoxide (CO) at 13%, hydrogen (H_2) at 17%, and ethanol at 11%. The total faradaic efficiency for C_{2+} products (ethylene, ethanol, and acetate) on the pure copper electrode was 53%, showcasing its ability to promote C-C coupling and generate multi-carbon products. This diverse product distribution can be attributed to the complex reaction pathways and the competing nature of the various reduction processes on the pure copper surface.

In contrast, the Cu_2Se electrocatalyst exhibited a lower current density of 148 mA cm^{-2}, indicating a slightly reduced overall catalytic activity compared to the pure copper electrode. However, the Cu_2Se electrocatalyst demonstrated a remarkable shift in product selectivity towards

oxygenated products, achieving an impressive faradaic efficiency of 69% for C_{2+} products. The product distribution was skewed towards oxygenated species, with ethanol (19%) and acetate (35%) being the dominant products, while the ethylene contribution was reduced to 15%. This shift in selectivity can be attributed to the presence of selenium in the Cu_2Se electrocatalyst, which modifies the electronic structure and surface properties of the catalyst, favoring the formation of oxygenated species over ethylene. The selenium atoms may stabilize key reaction intermediates, such as *COOH or *CO, leading to the preferential formation of ethanol and acetate. The Cu_2Se electrocatalyst's lower propensity for generating undesirable side products, such as hydrogen and carbon monoxide, further highlights its potential for efficient and targeted CO_2 reduction. These findings underscore the potential of the Cu_2Se electrocatalyst as a promising candidate for the efficient and selective conversion of CO_2 into valuable chemicals and fuels.

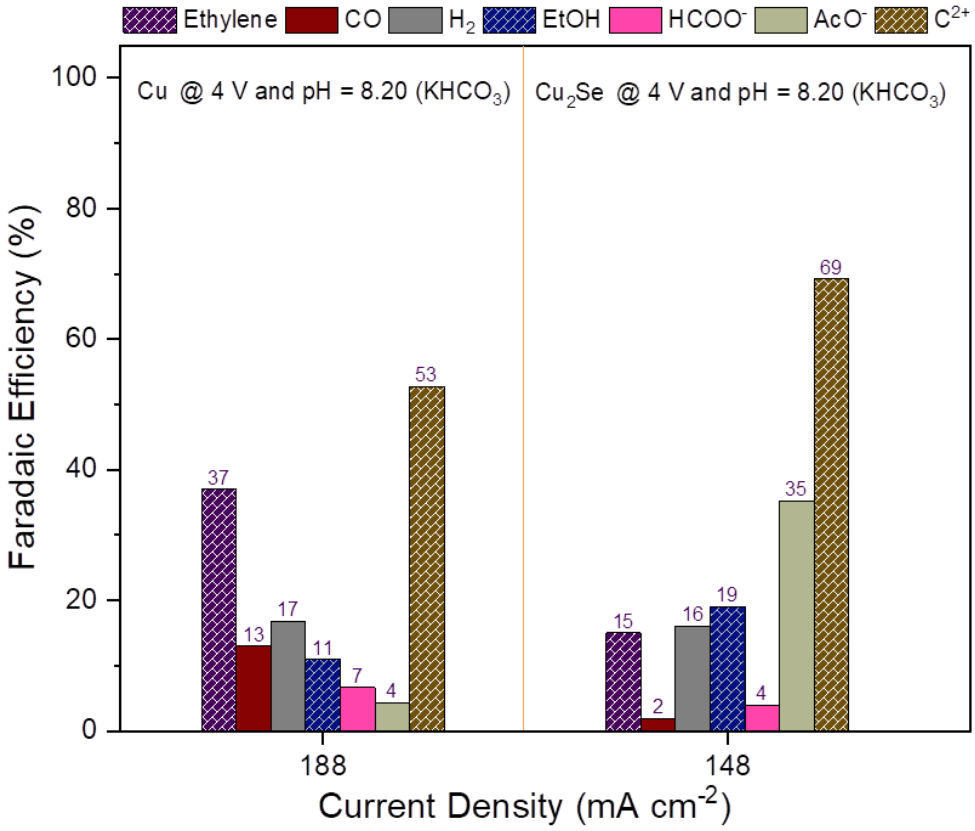

Figure 6.4. Faradaic efficiencies of CO_2 reduction products and current density at a constant cell potential of 4.0 V (Left) Pure Cu and (Right) Cu_2Se

6.3.2.2. Impact of pH

The impact of pH on the electrochemical CO_2 reduction performance of Cu_2Se electrocatalysts can be explored by comparing the results obtained in different electrolytes, namely 0.1 M $KHCO_3$ (pH = 8.20) and 1 M KOH (pH = 14.05), at a constant cell potential of 4.0 V. In the mildly alkaline electrolyte (0.1 M $KHCO_3$), the Cu_2Se electrocatalyst exhibited a current density of 148 mA cm^{-2}. The product distribution showed a remarkable selectivity towards C_{2+} products, with a total faradaic efficiency of 69%. Ethanol (19%) and acetate (35%) were the dominant products, while ethylene (15%), methane (5%), CO (2%), and formate (4%) were also observed. Hydrogen evolution, a competing reaction, accounted for 16% of the faradaic efficiency.

The high selectivity towards oxygenated products like ethanol and acetate in this mildly alkaline environment can be attributed to the stabilization of key reaction intermediates, such as *COOH or *CO, on the Cu_2Se surface.

When the pH was increased to 14.05 using 1 M KOH as the electrolyte, significant changes in the electrochemical CO_2 reduction performance were observed. The current density substantially increased to 350 mA cm^{-2}, indicating enhanced catalytic activity in the highly alkaline environment. However, the product distribution shifted notably, with a decrease in the selectivity towards ethylene (3%) and an increase in the selectivity towards ethanol (37%) and acetate (40%). The total faradaic efficiency for C_{2+} products remained high at 84%. Methane (4%), CO (1%), and formate (2%) were also produced, while hydrogen evolution accounted for 12% of the faradaic efficiency. The increased selectivity towards ethanol and acetate in the highly alkaline medium suggests that the reaction pathways favoring the formation of these oxygenated products are more favorable under these conditions. The suppression of ethylene formation can be attributed to the altered adsorption and binding energies of the reaction intermediates on the Cu2Se surface in the presence of a high concentration of hydroxide ions.

The impact of pH on the electrochemical CO_2 reduction performance of Cu_2Se electrocatalysts is evident from the data presented. Increasing the pH from 8.20 (0.1 M $KHCO_3$) to 14.05 (1 M KOH) led to a significant enhancement in the catalytic activity, as indicated by the higher current density. Moreover, the selectivity towards ethanol and acetate increased remarkably in the highly alkaline environment, while the selectivity towards ethylene decreased. These observations can be explained by the influence of pH on the reaction mechanisms and the adsorption behavior of the reaction intermediates on the Cu_2Se surface. The highly alkaline conditions appear to favor the formation of oxygenated products, particularly ethanol and acetate,

over hydrocarbons like ethylene. The suppression of hydrogen evolution in the highly alkaline medium is also noteworthy, as it allows for a more efficient utilization of the applied potential for CO_2 reduction. These findings highlight the importance of electrolyte pH in tuning the electrochemical CO_2 reduction performance of Cu_2Se electrocatalysts and provide valuable insights for optimizing the process towards the selective production of desired products.

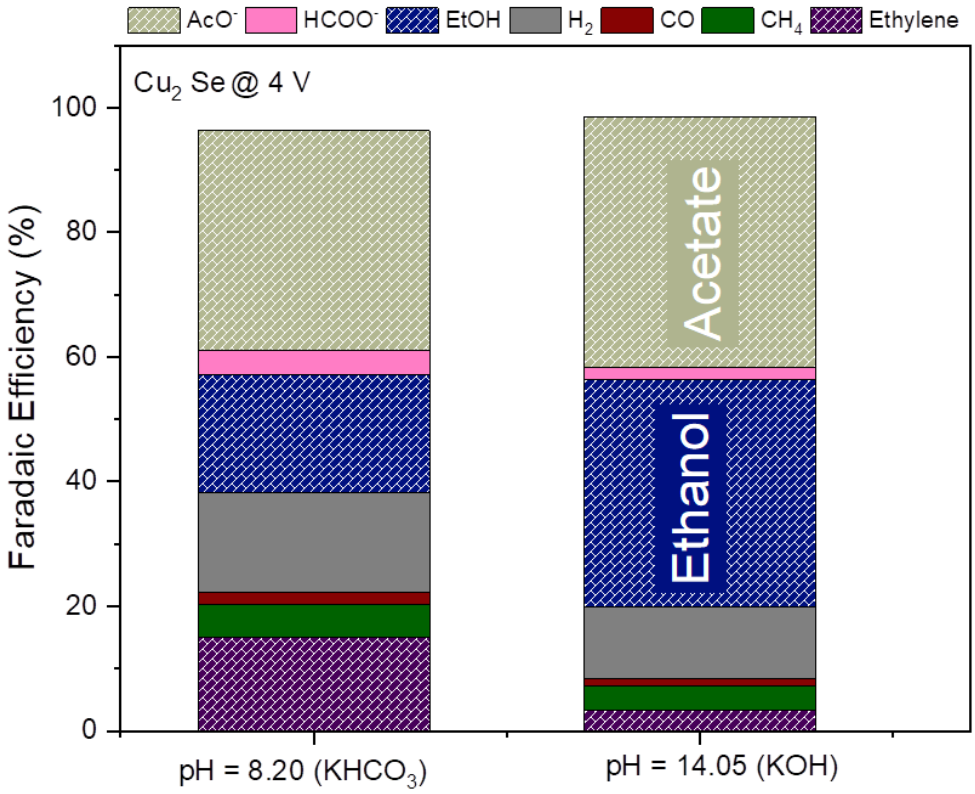

Figure 6.5. Faradaic efficiencies of CO_2 reduction products on Cu_2Se electrocatalysts at a constant cell potential of 4.0 V (Left) 0.1 M $KHCO_3$ (pH = 8.20) and (Right) 1 M KOH (pH = 14.05).

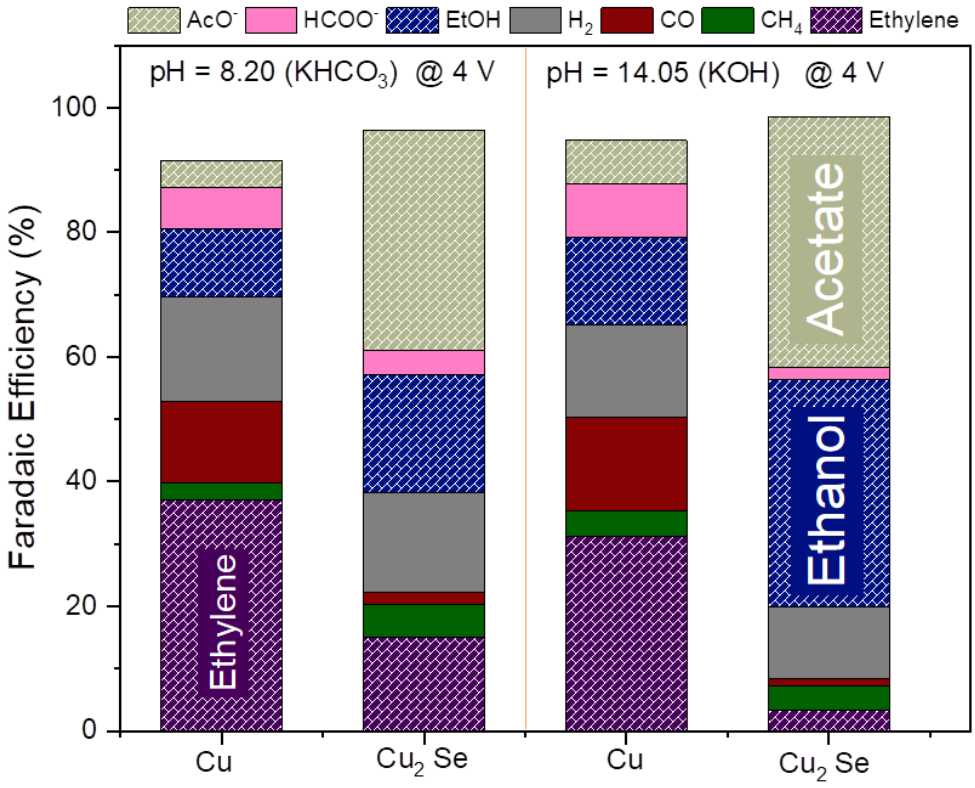

Figure 6.6. Comparison of Faradaic efficiencies of CO_2 reduction products at pure Cu and Cu_2Se

6.3.2.3. Impact of Potential

The impact of cell potential on the electrochemical CO_2 reduction performance of Cu_2Se electrocatalysts can be analyzed by examining the faradaic efficiencies of various products and the current density at different potentials, ranging from 3.6 V to 4.6 V. As shown in Figure 4, the Cu_2Se electrocatalyst demonstrates a clear dependence of product distribution and catalytic activity on the applied cell potential. At lower potentials, such as 3.6 V, the current density is relatively low, indicating a lower overall catalytic activity. However, as the potential increases, the current density gradually rises, reaching values of 138 mA cm^{-2}, 148 mA cm^{-2}, and 150 mA cm^{-2}

at 3.6 V, 4.0 V, and 5.0 V, respectively. This trend suggests that higher potentials favor increased electron transfer and enhance the overall CO_2 reduction reaction rate on the Cu_2Se surface.

Interestingly, the faradaic efficiencies of the various CO_2 reduction products also exhibit notable changes with increasing cell potential. Ethylene (C_2H_4) and methane (CH_4) show a slight decrease in faradaic efficiency as the potential increases from 4.0 V to 5.0 V, with ethylene decreasing from 15% to 12% and methane decreasing from 5% to 5%. On the other hand, the faradaic efficiency of ethanol experiences a modest increase from 19% to 23% over the same potential range. Acetate maintains a relatively stable Faradaic efficiency, ranging from 35% to 37%. The faradaic efficiencies of CO and formate remain low, below 5%, across the studied potential range. Hydrogen evolution, a competing reaction, accounts for 15-17% of the faradaic efficiency.

The observed trends in product distribution can be attributed to the influence of cell potential on the reaction pathways and the adsorption behavior of key intermediates on the Cu_2Se surface. At higher potentials, the increased availability of electrons and the altered adsorption energies of reaction intermediates may favor the formation of ethanol over ethylene and methane. The stability of acetate faradaic efficiency suggests that the reaction pathway leading to its formation is less sensitive to potential changes within the studied range. The low faradaic efficiencies of CO and formate indicate that the Cu_2Se electrocatalyst has a lower selectivity towards these products, regardless of the applied potential.

These findings highlight the importance of tuning the cell potential to optimize the electrochemical CO_2 reduction performance of Cu_2Se electrocatalysts. By carefully selecting the appropriate potential, it is possible to enhance the catalytic activity and steer the product distribution towards desired products, such as ethanol. The potential-dependent behavior of the

Cu_2Se electrocatalyst provides valuable insights into the underlying reaction mechanisms and the role of potential in controlling the selectivity and efficiency of the CO_2 reduction process. Further studies focusing on a wider potential range and detailed mechanistic investigations can help elucidate the complex interplay between potential, surface properties, and reaction pathways, ultimately guiding the design of more efficient and selective Cu_2Se-based electrocatalysts for CO_2 reduction.

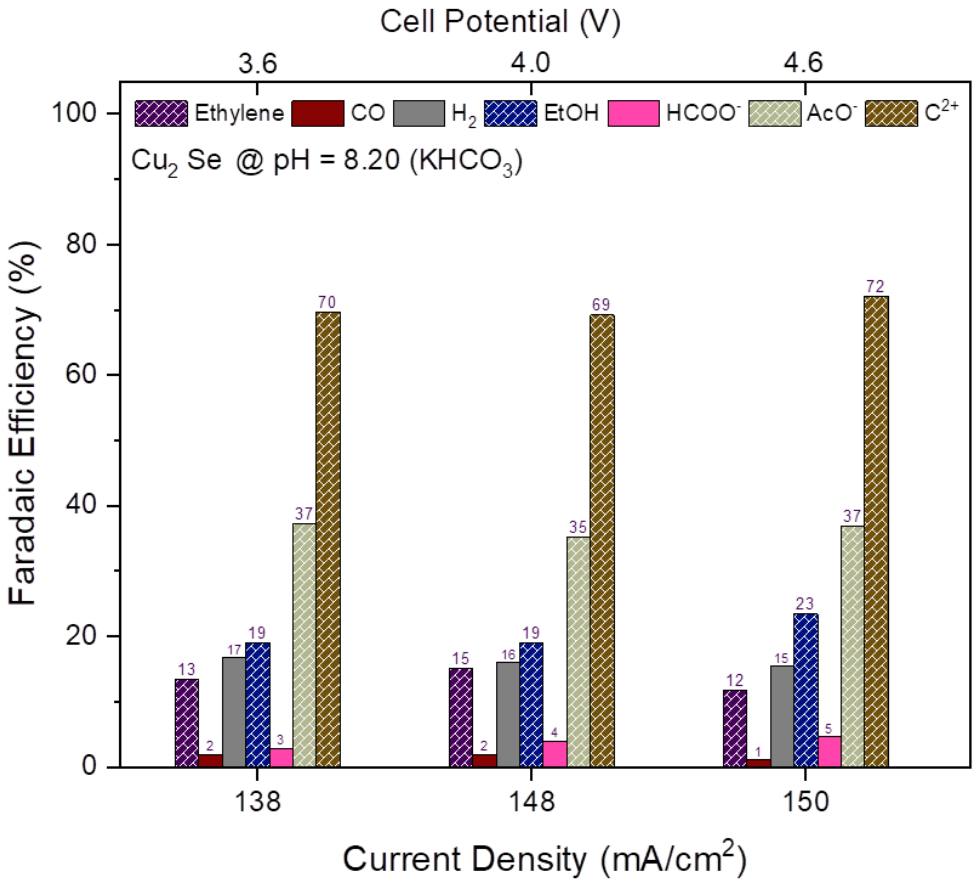

Figure 6.7. Faradaic efficiencies of CO_2 reduction products and current density at varied cell potentials from 3.6 V to 4.6 V for Cu_2Se

6.3.2.4. Comparison of Cu_2Se with Previously Reported Cu-SE Electrocatalysts

The comparison of the Cu_2Se electrocatalyst with previously reported Cu-Se catalysts highlights the significant advancements made in the field of electrochemical CO_2 reduction. The Cu_2Se electrocatalyst developed in this work demonstrates remarkable performance in terms of faradaic efficiency (FE) and current density, surpassing the results of earlier studies. In a previous report, a Cu_2Se electrocatalyst achieved an impressive 84% FE for ethanol and 15% FE for acetate at a current density of 50 mA cm^{-2}. This showcases the potential of Cu_2Se-based catalysts to selectively produce valuable oxygenated products from CO_2 reduction. Another study on K11.2%-Cu_2Se catalyst reported a peak faradaic efficiency of 70.3% for ethanol at -0.8 V, corresponding to a current density of 36 mA cm^{-2}. These findings highlight the ability of Cu-Se catalysts to effectively reduce CO_2 to ethanol with high selectivity and efficiency.

However, the Cu_2Se electrocatalyst developed in this work sets a new benchmark in terms of performance. At a current density of 150 mA cm^{-2}, this Cu_2Se catalyst achieves a remarkable 37% FE for acetate. This represents a significant improvement over the previously reported Cu-Se catalysts, demonstrating the enhanced selectivity and activity of the current Cu_2Se electrocatalyst. Furthermore, when the current density is increased to 350 mA cm^{-2}, the FE for acetate reaches an impressive 47%. This indicates that the Cu_2Se electrocatalyst maintains its selectivity towards acetate even at higher current densities, which is crucial for practical applications and scale-up processes.

The superior performance of the Cu_2Se electrocatalyst developed in this work can be attributed to several factors. The unique structure and composition of the catalyst likely play a crucial role in its enhanced activity and selectivity. The presence of Se in the Cu_2Se catalyst may modify the electronic structure and surface properties, favoring the formation of oxygenated

products like acetate. Additionally, the optimization of synthesis methods and reaction conditions could have contributed to the improved performance. The high current densities achieved by this Cu_2Se electrocatalyst are particularly noteworthy, as they demonstrate the potential for efficient and high-throughput CO_2 reduction, which is essential for practical applications.

In summary, the Cu_2Se electrocatalyst developed in this work outperforms previously reported Cu-Se catalysts in terms of faradaic efficiency and current density for the electrochemical reduction of CO_2. The achievement of 37% FE for acetate at 150 mA cm^{-2} and 47% FE for acetate at 350 mA cm^{-2} represents a significant advancement in the field. These results highlight the potential of this Cu_2Se electrocatalyst as a promising candidate for efficient and selective CO_2 reduction, paving the way for the development of sustainable technologies for the production of valuable chemicals and fuels from CO_2.

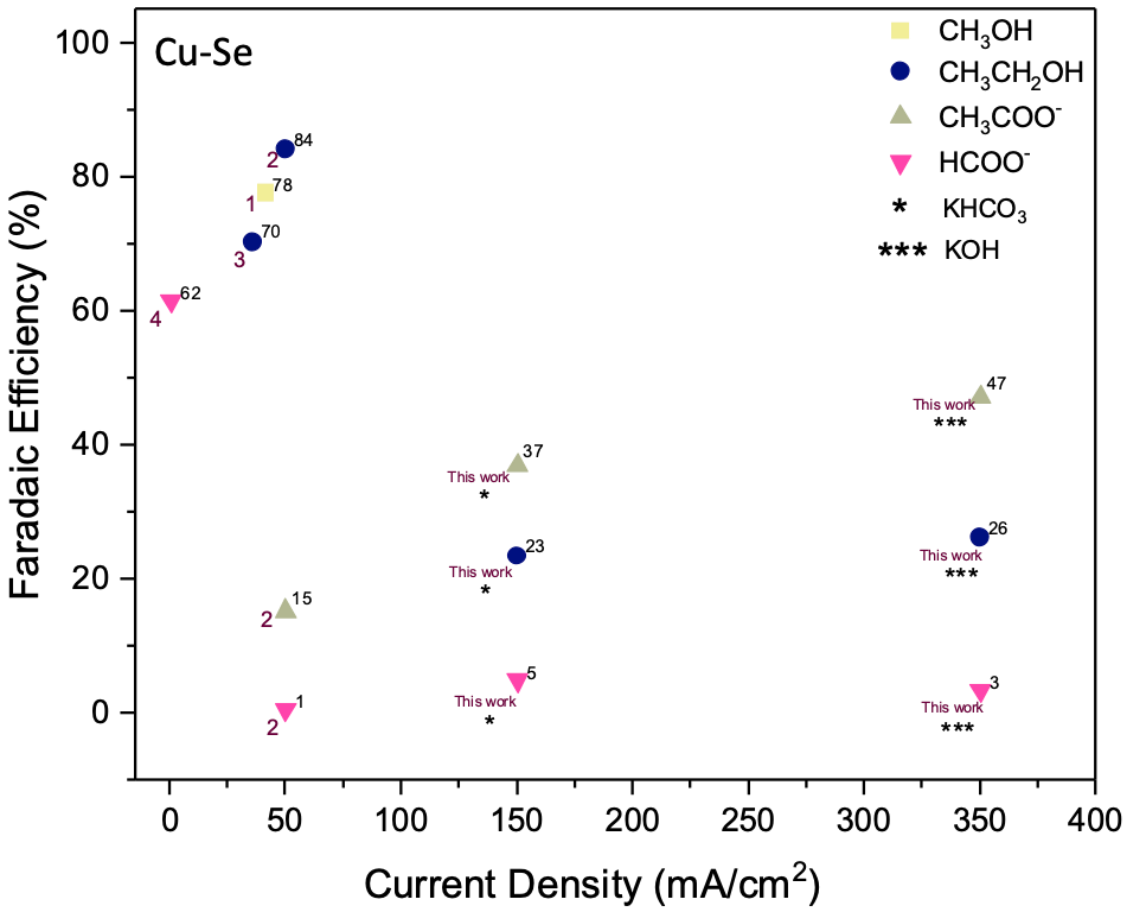

Figure 6.8. Comparison of Cu_2Se with previously reported Cu_2Se catalysts. (1) The Cu_2Se electrocatalyst demonstrated 84 % FE of ethanol and 15 % FE of acetate at 50 mA cm^{-2} .(Saxena et al., 2021) (2) The $K_{11.2\%}$-Cu_2Se catalyst demonstrates a peak faradaic efficiency (FE) of 70.3% for ethanol at -0.8 V (36 mA cm^{-2}). (Ding et al., 2022)

6.4. Discussion

The Cu_2Se electrocatalyst developed in this work has demonstrated remarkable performance in the selective electrochemical reduction of CO_2 to oxygenated products, particularly ethanol and acetate. The comprehensive characterization of the Cu_2Se electrocatalyst using advanced techniques such as SEM, EDS, XRD, XPS, and ICP-OES has provided valuable insights into its morphology, composition, crystal structure, and electronic properties. The SEM and EDS analyses revealed the uniform size, spherical shape, and homogeneous distribution of Cu and Se in the Cu_2Se nanoparticles. The XRD results confirmed the formation of the cubic $Cu_{2-x}Se$ phase

and its stability under CO_2 reduction conditions. The XPS and ICP-OES studies elucidated the oxidation states of Cu and Se and the bulk composition of the Cu_2Se electrocatalyst, verifying the successful synthesis of the desired Cu_2Se phase.

The electrochemical performance of the Cu_2Se electrocatalyst was evaluated and compared to that of the pure Cu electrode, highlighting the impact of Se incorporation on the catalytic activity and selectivity. The Cu_2Se electrocatalyst exhibited a remarkable shift in product distribution towards oxygenated products, with high faradaic efficiencies for ethanol and acetate. The enhanced selectivity was attributed to the modification of the electronic structure and the stabilization of key reaction intermediates by the presence of Se in the Cu_2Se catalyst. The impact of electrolyte pH on the Cu_2Se electrocatalyst's performance was also investigated, revealing a significant enhancement in catalytic activity and selectivity towards ethanol and acetate in highly alkaline conditions. The suppression of ethylene formation and the reduced hydrogen evolution in the alkaline medium further demonstrated the advantageous properties of the Cu_2Se electrocatalyst.

The comparison of the Cu_2Se electrocatalyst with previously reported Cu-Se catalysts underscored the significant advancements achieved in this work. The Cu_2Se electrocatalyst developed here outperformed earlier Cu-Se catalysts in terms of faradaic efficiency and current density, setting new benchmarks for the selective production of oxygenated products from CO_2 reduction. The superior performance of the Cu_2Se electrocatalyst can be attributed to its unique composition, optimized synthesis method, and favorable reaction conditions. The high current densities achieved by this Cu_2Se electrocatalyst demonstrate its potential for efficient and scalable CO_2 reduction, which is crucial for practical applications in the production of valuable chemicals and fuels from CO_2.

6.5. Conclusion

In conclusion, this work presents the development and comprehensive characterization of a novel Cu_2Se electrocatalyst for the selective electrochemical reduction of CO_2 to oxygenated products, particularly ethanol and acetate. The Cu_2Se electrocatalyst, synthesized through a colloidal approach, exhibits uniform size, spherical morphology, and a homogeneous distribution of Cu and Se. The formation of the cubic $Cu_{2-x}Se$ phase and its stability under CO_2 reduction conditions were confirmed by XRD analysis. The electrochemical performance of the Cu2Se electrocatalyst surpasses that of the pure Cu electrode and previously reported Cu-Se catalysts, achieving remarkable faradaic efficiencies of 37% for acetate at 150 mA cm^{-2} and 47% for acetate at 350 mA cm^{-2} in a highly alkaline electrolyte.

The enhanced selectivity towards oxygenated products on the Cu2Se electrocatalyst is attributed to the modification of the electronic structure and the stabilization of key reaction intermediates by the incorporation of Se. The impact of electrolyte pH on the Cu_2Se electrocatalyst's performance highlights the importance of alkaline conditions in promoting the selective formation of ethanol and acetate while suppressing ethylene production and hydrogen evolution. The superior performance of the Cu2Se electrocatalyst compared to previously reported Cu-Se catalysts demonstrates the significant advancements achieved in this work, setting new benchmarks for the efficient and selective electrochemical reduction of CO_2.

This work underscores the potential of the Cu_2Se electrocatalyst as a promising candidate for the sustainable production of valuable oxygenated chemicals and fuels from CO_2. The insights gained from the comprehensive characterization and electrochemical studies provide a solid foundation for further optimization and scale-up of the Cu_2Se electrocatalyst. Future research directions may include investigating the long-term stability of the catalyst, exploring the effect of

nanoparticle size and morphology on the catalytic performance, and conducting mechanistic studies to elucidate the reaction pathways and the role of Se in the selective formation of oxygenated products. The development of efficient and selective electrocatalysts like Cu_2Se is crucial for the realization of practical CO_2 reduction technologies and the transition towards a sustainable carbon economy.

CHAPTER 7. DURABILITY TESTING OF CU-P, CU-SN, AND CU_2SE ELECTROLYSIS ELECTROCATALYSTS

7.1. Introduction

The electrochemical reduction of CO_2 has emerged as a promising approach to address the global challenge of increasing atmospheric CO_2 levels while simultaneously producing valuable fuels and chemicals. Among the various products that can be generated from CO_2 reduction, multi-carbon compounds such as ethylene, ethanol, and propanol have attracted significant attention due to their higher energy density, versatility, and potential as drop-in replacements for fossil-derived fuels and chemicals. However, the commercial viability and widespread adoption of CO_2 reduction technology rely heavily on the development of efficient, selective, and, most importantly, durable electrocatalysts. (Chen et al., 2021; Liu et al., 2017; Nitopi et al., 2019; J. Zhang et al., 2023)

Electrocatalyst stability is a critical factor in the practical implementation of CO_2 reduction systems, as it directly impacts the long-term performance, cost-effectiveness, and scalability of the technology. Electrocatalysts that can maintain their activity and selectivity over extended periods of operation are essential for industrial-scale applications. Unfortunately, many of the current state-of-the-art electrocatalysts for CO_2 reduction, particularly those based on Cu, suffer from limited durability due to various degradation mechanisms such as poisoning, restructuring, and chemical instability. The need for comprehensive stability studies for multi-carbon product generation from CO_2 reduction cannot be overstated. While numerous studies have focused on developing novel electrocatalysts with improved activity and selectivity, the long-term durability of these materials under realistic operating conditions has often been overlooked. Systematic investigations into the stability of electrocatalysts over extended time scales (hundreds to thousands of hours) are crucial to identify the underlying degradation mechanisms, develop mitigation strategies, and design robust catalytic systems.

Durability studies provide valuable insights into the complex interplay between the electrocatalyst, electrolyte, and reaction intermediates during CO_2 reduction. By monitoring the performance of electrocatalysts over time, researchers can identify the onset and progression of degradation, elucidate the underlying causes, and develop rational strategies to enhance catalyst stability. This information is essential for guiding the design of next generation electrocatalysts with improved durability and for optimizing the operating conditions to minimize degradation. Furthermore, stability studies are vital for bridging the gap between fundamental research and practical applications. While many electrocatalysts have shown promising performance in short-term laboratory-scale experiments, their ability to maintain this performance over extended periods under industrially relevant conditions is often unknown. Conducting long-term durability tests in flow electrolyzers and membrane electrode assembly (MEA) systems, which closely mimic real-world operating conditions, is crucial for assessing the true potential of electrocatalysts and identifying the challenges that need to be addressed for successful commercialization.

In this chapter, we will focus on the durability testing of three promising electrocatalyst systems for multi-carbon product generation from CO_2 reduction: copper-phosphide (Cu-P), copper-tin (Cu-Sn), and copper selenide (Cu_2Se). These materials have shown excellent activity and selectivity towards the formation of valuable products such as ethylene, ethanol, and acetate. However, their long-term stability remains a critical question that needs to be addressed. We will present a comprehensive study on the durability of these electrocatalysts under various operating conditions, discuss the observed degradation mechanisms, and propose strategies for enhancing their stability. The insights gained from this study will contribute to the development of robust and durable electrocatalysts for efficient and sustainable CO_2 reduction, paving the way for the practical implementation of this technology.

7.2. Experimental Setup for Durability Testing of Cu-P, Cu-Sn, and Cu_2Se Electrolysis Electrocatalysts

The durability testing of Cu-P, Cu-Sn, and Cu_2Se electrocatalysts for the electrochemical reduction of CO_2 was conducted using a custom-designed zero-gap membrane electrode assembly (MEA) cell. The MEA cell configuration minimizes the distance between the cathode and anode, reducing ohmic losses and enhancing mass transport. The cathode flow field was fabricated from 2205 stainless steel and featured a serpentine flow channel to facilitate efficient CO_2 transport across the gas diffusion electrode (GDE). The serpentine design maximizes the contact area between the gaseous CO_2 and the electrocatalyst layer, promoting increased CO2 utilization and improved reaction kinetics. The anode flow field, on the other hand, was milled from grade 2 titanium and also incorporated a serpentine flow channel to ensure optimal distribution and flow of the anolyte solution.

The reactant gases and electrolyte solutions were precisely regulated and monitored throughout the durability tests. CO_2 was supplied to the cathode side of the MEA cell at a constant flow rate of 20 standard cubic centimeters per minute (sccm) using a mass flow controller (Alicat MC-500SCCM). The CO_2 flow rate was carefully selected to maintain a sufficient concentration gradient across the GDE, driving the CO_2 reduction reaction forward. On the anode side, an aqueous 0.1 M KHCO3 solution was employed as the electrolyte and circulated at a flow rate of 10 mL min^{-1} using a peristaltic pump (CHEM-TECH). The $KHCO_3$ electrolyte serves as a proton source and helps to maintain a stable pH environment for the oxidation reaction. The cathode and anode flow rates were precisely controlled using dedicated mass flow controllers and monitored in real-time using Flow Vision 2.0 software, ensuring consistent and reliable operation throughout the extended durability tests.

To evaluate the performance and stability of the Cu-$P_{0.065}$, Cu-$Sn_{0.03}$, and Cu_2Se electrocatalysts, the MEA cells were operated at a constant current density of 150 mA cm^{-2} for over 200 hours. This current density was selected to mimic industrially relevant operating conditions and assess the long-term durability of the electrocatalysts under practical CO_2 reduction scenarios. During the durability tests, the Faradaic efficiencies (FEs) of the CO_2 reduction products were determined by analyzing the outlet gas and liquid streams. The gaseous products were quantified using a calibrated gas chromatograph (GC), while the liquid products were characterized using nuclear magnetic resonance (NMR) spectroscopy. The combination of GC and NMR analyses provided a comprehensive understanding of the product distribution and the selectivity of the electrocatalysts over time. The FEs were calculated based on the outlet flow rates and the measured product concentrations, allowing for the assessment of the electrocatalysts' performance and stability. The durability tests were intentionally stopped after surpassing the 200-hour mark to conduct post-mortem analyses of the electrocatalysts and investigate any changes in their morphology, composition, or surface properties that may have occurred during the prolonged operation.

The experimental setup described above enables the systematic evaluation of the durability and performance of Cu-P, Cu-Sn, and Cu_2Se electrocatalysts for the electrochemical reduction of CO_2 under realistic operating conditions. The zero-gap MEA cell configuration, coupled with precise control over the reactant flows and electrolyte composition, provides a robust platform for assessing the long-term stability of these electrocatalysts. The extended durability tests, spanning over 200 hours at a constant current density, offer valuable insights into the practical applicability and potential commercialization of these Cu-based electrocatalysts for CO_2 reduction. The comprehensive product analysis using GC and NMR techniques allows for the accurate

determination of the Faradaic efficiencies and selectivity trends over time, shedding light on the underlying mechanisms and the impact of the electrocatalyst composition on the CO_2 reduction performance. The post-mortem characterization of the electrocatalysts after the durability tests provides further understanding of the structural and compositional changes that may influence their long-term stability and activity.

7.3. Stability Measurement

7.3.1. Electrochemical performance

The durability testing of Cu-$P_{0.065}$, Cu-$Sn_{0.03}$, and Cu_2Se electrocatalysts revealed notable changes in their Faradaic efficiencies (FEs) and product selectivity over the course of 220 hours of continuous operation at a current density of 150 mA cm^{-2}. For the Cu-$P_{0.065}$ electrocatalyst, the FE for ethylene, which was initially the primary product, decreased from 52% to 43% over the 220-hour period. Similarly, the FE for ethanol dropped from 22% to 18% during the same timeframe. Conversely, the FE for hydrogen (H_2) increased from 14% to 19%, indicating a shift in selectivity towards the competing hydrogen evolution reaction (HER). The cell potential for the Cu-$P_{0.065}$ electrocatalyst increased at a rate of 2 mV h^{-1}, suggesting a gradual increase in the overpotential required to maintain the desired current density.

The Cu-$Sn_{0.03}$ electrocatalyst, which initially favored the formation of ethanol, experienced a decrease in ethanol FE from 24% to 18% over the 220-hour durability test. The FE for ethylene also declined from 13% to 10% during the same period. Similar to the Cu-$P_{0.065}$ electrocatalyst, the Cu-$Sn_{0.03}$ electrocatalyst showed an increase in hydrogen FE, rising from 10% to 17%. This shift towards HER suggests a loss of selectivity for CO_2 reduction and an increased preference for the competing HER pathway. The cell potential for the Cu-$Sn_{0.03}$ electrocatalyst increased at a rate of 1 mV h^{-1}, indicating a relatively stable performance compared to the Cu-$P_{0.065}$ electrocatalyst.

The Cu_2Se electrocatalyst, which exhibited a unique selectivity towards acetate production, also experienced changes in its product distribution over the 220-hour durability test. The FE for acetate decreased from 35% to 30%, while the FE for ethanol dropped from 27% to 20%. Consistent with the trends observed for the Cu-$P_{0.065}$ and Cu-$Sn_{0.03}$ electrocatalysts, the Cu_2Se electrocatalyst showed an increase in hydrogen FE, rising from 17% to 26%. This shift towards HER indicates a gradual loss of selectivity for CO_2 reduction and an increased preference for the competing HER pathway. The cell potential for the Cu_2Se electrocatalyst increased at a rate of 1 mV h^{-1}, similar to the Cu-$Sn_{0.03}$ electrocatalyst, suggesting a relatively stable performance.

The durability testing results highlight the challenges associated with maintaining the selectivity and activity of Cu-based electrocatalysts for CO_2 reduction over extended periods of operation. The observed changes in Faradaic efficiencies and the increase in hydrogen evolution indicate a gradual loss of selectivity for the desired CO_2 reduction products and an increased preference for the competing HER pathway. These changes can be attributed to various factors, such as the loss of heteroatom dopants (e.g., P, Sn, or Se), surface reconstruction, or the accumulation of carbonaceous species on the electrocatalyst surface. The increase in cell potential over time suggests a gradual increase in the overpotential required to maintain the desired current density, which could be related to the changes in the electrocatalyst surface or the build-up of resistive layers.

Despite the observed changes in product selectivity and the increase in cell potential, the Cu-$P_{0.065}$, Cu-$Sn_{0.03}$, and Cu_2Se electrocatalysts demonstrated reasonable stability over the 220-hour durability test. The gradual nature of the changes in Faradaic efficiencies and the relatively low rates of cell potential increase suggest that these electrocatalysts have the potential for long-term operation with further optimization. Strategies to mitigate the loss of selectivity and activity

could include the development of more robust heteroatom doping techniques, the use of protective layers to prevent surface reconstruction, or the incorporation of regeneration steps to remove accumulated carbonaceous species. Additionally, investigating the underlying mechanisms of the observed changes through advanced characterization techniques and computational studies could provide valuable insights for the rational design of more stable and selective Cu-based electrocatalysts for CO_2 reduction.

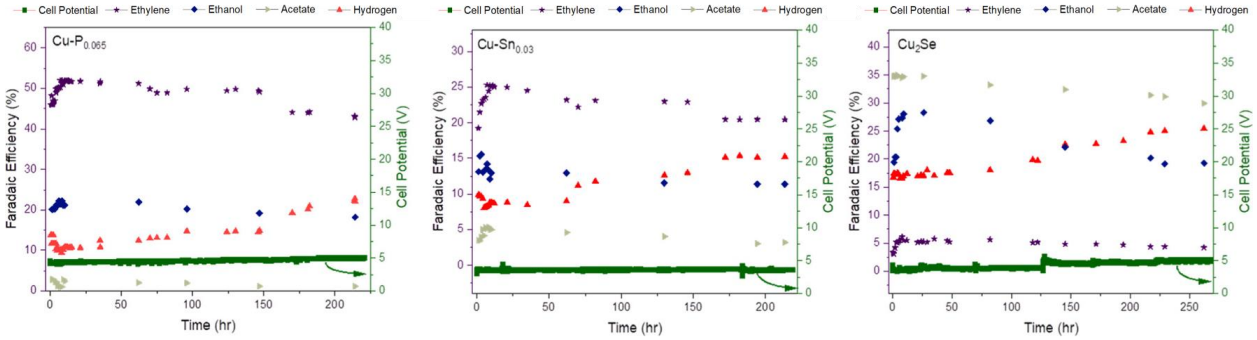

Figure 7.1. Durability tests on MEA cells with Cu-$P_{0.065}$, Cu-$Sn_{0.03}$, and Cu_2Se electrocatalysts, operated at 150 mA cm^{-2} for over 200 hours, revealed gradual declines in product selectivity.

7.3.2. Scanning Electron Microscope (SEM)

The morphological stability and structural integrity of electrocatalysts during prolonged electrochemical operations are paramount factors that significantly influence their catalytic performance, durability, and practical viability. The scanning electron microscopy (SEM) analyses illustrated in Figure 6 offer valuable insights into the morphological transformations exhibited by three distinct copper-based electrocatalysts, namely Cu-P, Cu-Sn, and Cu-Se, subjected to extended CO_2 electrolysis at an appreciable current density of 150 mA cm^{-2}. The electrolysis was conducted in an aqueous potassium bicarbonate ($KHCO_3$) solution, a commonly employed electrolyte for CO_2 reduction reactions. The SEM images provide a comparative visualization of the catalysts' morphologies before and after this rigorous electrochemical treatment, enabling a comprehensive evaluation of their structural resilience under operational conditions.

Prior to the electrolysis, all three electrocatalysts displayed a densely packed architecture comprising spherical copper-based nanoparticles supported on gas diffusion electrodes (GDEs). These GDEs incorporated polyvinylidene fluoride (PVDF) as a binder material and Vulcan carbon as a conductive support, ensuring efficient charge transport and catalyst dispersion. However, upon subjecting these catalysts to prolonged CO_2 electrolysis, distinct morphological changes became apparent. Both the Cu-P and Cu-Sn electrocatalysts exhibited significant agglomeration, wherein the initially spherical nanoparticles coalesced and restructured into larger cubic morphologies. This transformation suggests that the Cu-P and Cu-Sn nanoparticles were susceptible to sintering and restructuring processes under the applied electrochemical conditions, which could potentially compromise their catalytic activity and long-term stability.

In contrast, the Cu-Se electrocatalyst demonstrated remarkable structural stability, with its nanoparticles remaining relatively intact and retaining their original morphology even after the prolonged CO_2 electrolysis. This exceptional resilience is attributed to the strong Cu-Se interactions within the nanoparticles, which effectively mitigated the agglomeration and sintering processes that were observed in the Cu-P and Cu-Sn systems. The robust nature of the Cu-Se electrocatalyst implies that it may offer superior durability and maintain its catalytic performance over extended periods of operation, making it a promising candidate for practical applications in CO_2 reduction reactions. This stability advantage of the Cu-Se electrocatalyst could be a crucial factor in its potential for large-scale deployment and commercial viability, as it addresses the critical challenge of catalyst deactivation often encountered in electrocatalytic processes.

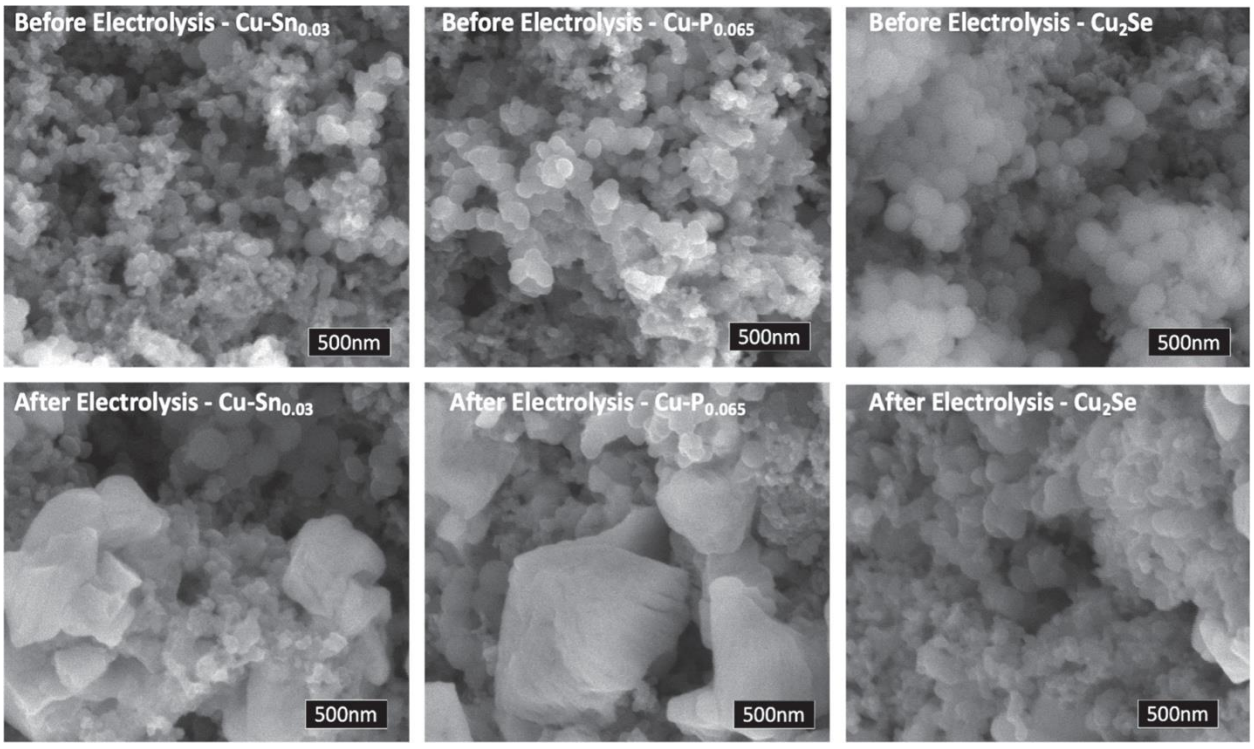

Figure 7.2. SEM images of Cu-$Sn_{0.03}$, Cu-$P_{0.065}$, and Cu_2Se electrocatalysts on GDE with PVDF and Vulcan carbon support before and after prolonged CO_2 electrolysis at 150 mA cm^{-2} in $KHCO_3$, showing a transformation from densely packed spherical Cu-based nanoparticles to larger cubic shapes

7.3.3. X-ray Photoelectron Spectroscopy (XPS) Analysis

Ex-situ XPS analyses were conducted on the Cu-Sn, Cu-P, and Cu_2Se electrocatalysts after subjecting them to extended CO_2 electrolysis at a current density of 150 mA cm^{-2} for over 200 hours. These analyses aimed to investigate the relative surface concentrations of the different copper oxidation states, particularly the metallic Cu^0 and the oxidized Cu^+ species, which are known to play crucial roles in the catalytic activity and selectivity for CO_2 reduction reactions. The XPS results, as depicted in Figure 6, revealed a consistent trend across all three electrocatalysts: an increase in the relative surface concentration of the metallic Cu^0 species after the prolonged electrolysis. Specifically, for the Cu-Sn electrocatalyst, the Cu^0 concentration increased from 53.2% to 85.4%, accompanied by a corresponding decrease in the Cu^+

concentration from 47.0% to 14.6%. Similarly, the Cu-P electrocatalyst exhibited an increase in Cu^0 from 56.4% to 92.8%, with a concurrent decrease in Cu^+ from 43.6% to 7.2%. The Cu2Se electrocatalyst followed a similar trend, with Cu^0increasing from 39.4% to 53.3% and Cu^+ decreasing from 60.6% to 46.7%. These ex-situ XPS results provide a relative sense of the changes in the copper oxidation states during the electrolysis process. However, it is important to note that the electrocatalysts were evaluated several hours after the electrolysis, potentially subjecting them to oxidation in air before the XPS analysis. This limitation implies that the observed increase in Cu^0concentration may be an underestimation, as some re-oxidation of the metallic copper could have occurred during the time elapsed between electrolysis and analysis.

While the ex-situ XPS analyses offer valuable insights, their interpretation is constrained by the inherent limitations associated with post-electrolysis measurements. To gain a more accurate understanding of the dynamic redox behavior and oxidation state changes occurring during the CO_2 reduction process, operando techniques such as time-resolved X-ray absorption spectroscopy (XAS) and in-situ Raman spectroscopy are crucial.

In summary, the ex-situ XPS analyses provided valuable insights into the relative changes in copper oxidation states after prolonged CO_2 electrolysis, revealing an increase in the metallic Cu^0 concentration across all three electrocatalysts. However, the interpretation of these results is limited by potential re-oxidation during the time elapsed between electrolysis and analysis. To gain a more comprehensive understanding of the dynamic redox behavior and oxidation state changes during the CO_2 reduction process, operando techniques such as time-resolved XAS and in-situ Raman spectroscopy are essential. These techniques, coupled with thermodynamic considerations and complementary characterization methods, can elucidate the intricate interplay

between electrocatalyst composition, oxidation states, and structural transformations, ultimately guiding the design of more active and stable electrocatalysts for CO_2 reduction applications.

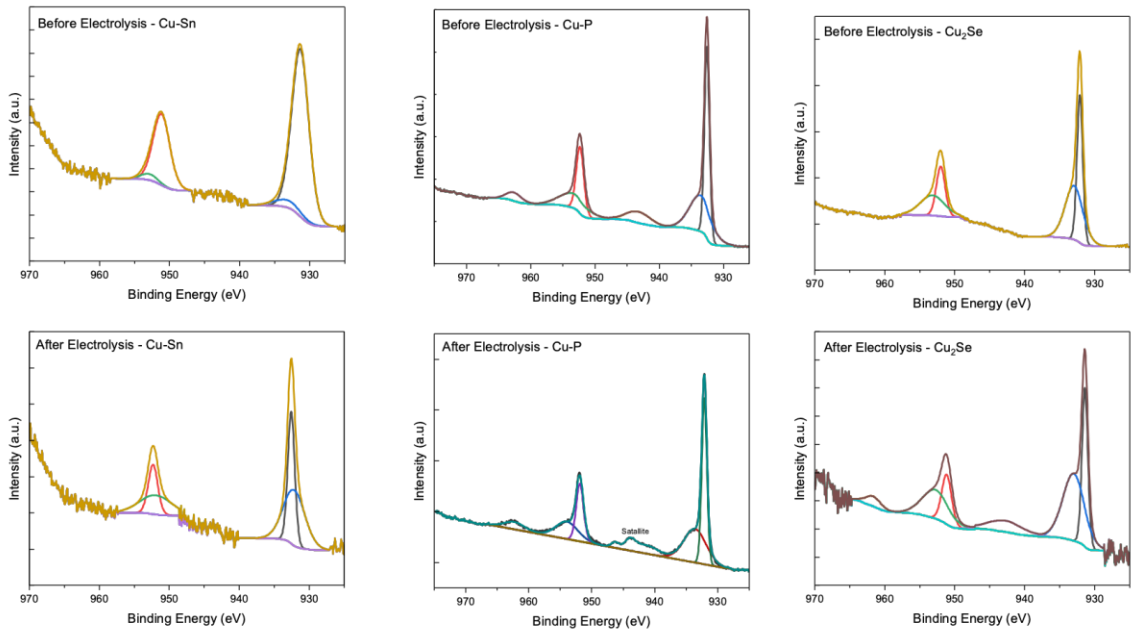

Figure 7.3. X-ray photoelectron spectroscopy (XPS) of the Cu electrocatalysts before and after CO_2 electrolysis. Upper row: Spectra before electrolysis for (Left) Cu-$Sn_{0.03}$, (Middle) Cu-$P_{0.065}$, and (Right) Cu_2Se. Lower row: Spectra for the same samples after electrolysis (over 200 h at 150 mA cm^{-2})

7.4. Thermodynamic Consideration

The thermodynamic stability of electrocatalysts plays a pivotal role in their behavior and performance during CO_2 reduction reactions. Pourbaix diagrams, which depict the stability regions of different phases as a function of pH and applied potential, offer valuable insights into the thermodynamic considerations governing the stability of copper-based electrocatalysts. Figures 9-10 and Figure 7 present the Pourbaix diagrams for copper and copper-selenium systems at 25°C, highlighting the reduction potentials of various copper species and their implications for CO_2 reduction. In the case of pure copper systems (Figure 9), the reduction of copper(I) oxide (Cu_2O) to metallic copper occurs at a potential of +0.58 V versus the Reversible Hydrogen Electrode

(RHE). However, the reduction of CO_2 to carbon monoxide (CO), a crucial intermediate in CO_2 reduction reactions, occurs at a more negative potential of -0.11 V versus RHE. This potential gap suggests that the conditions required for CO_2 reduction will simultaneously reduce Cu_2O to metallic copper, leading to potential instability and restructuring of the electrocatalyst surface

Interestingly, the Pourbaix diagram for the copper-selenium system (Figure 7) reveals a markedly different behavior. In this case, the reduction of copper (I) selenide (Cu_2Se) to metallic copper and hydrogen selenide (HSe^-) occurs at a potential of -0.58 V versus RHE. This reduction potential is significantly more negative than the potential required for CO_2 reduction to CO (-0.11 V vs. RHE). As a result, the Cu_2Se electrocatalyst exhibits a stable overpotential window for CO_2 reduction without compromising the oxidation state of the $Cu^{\delta+}$ species. This thermodynamic stability of the Cu_2Se electrocatalyst under CO_2 reduction conditions could potentially contribute to its superior structural integrity observed in the scanning electron microscopy (SEM) analyses. Unlike the Cu-P and Cu-Sn electrocatalysts, which exhibited significant agglomeration and reshaping after prolonged electrolysis, the Cu_2Se nanoparticles remained relatively intact, suggesting enhanced stability against sintering, and restructuring processes.

The contrasting behavior observed between pure copper systems and the copper-selenium system can be attributed to the influence of the electronegative selenium dopant. As depicted in Figure S10, the reduction potential for Cu_2Se is significantly lower than that of Cu_2O, suggesting that electronegative doping with elements like selenium can stabilize the Cu^+ species and potentially lead to enhanced CO^2 reduction performance compared to pure copper systems. This thermodynamic consideration highlights the potential benefits of incorporating electronegative dopants, such as selenium, phosphorus, or tin, into copper-based electrocatalysts. By modulating the reduction potentials and stabilizing the desired oxidation states, these dopants could potentially

mitigate the dynamic oxidation of copper under cathodic potentials, a phenomenon often attributed to factors like oxygen crossover and chemical oxidation of electrically disconnected copper particles at the cathode.

The thermodynamic stability of electrocatalysts, as illustrated by the Pourbaix diagrams, plays a crucial role in their behavior and performance during CO_2 reduction reactions. The copper-selenium system, with its stable overpotential window for CO_2 reduction without compromising the oxidation state of the $Cu^{\delta+}$ species, showcases the potential benefits of incorporating electronegative dopants. By tuning the reduction potentials and stabilizing the desired oxidation states, these doped electrocatalysts could potentially enhance structural stability, mitigate undesired restructuring, and ultimately improve catalytic activity and selectivity for CO_2 reduction applications.

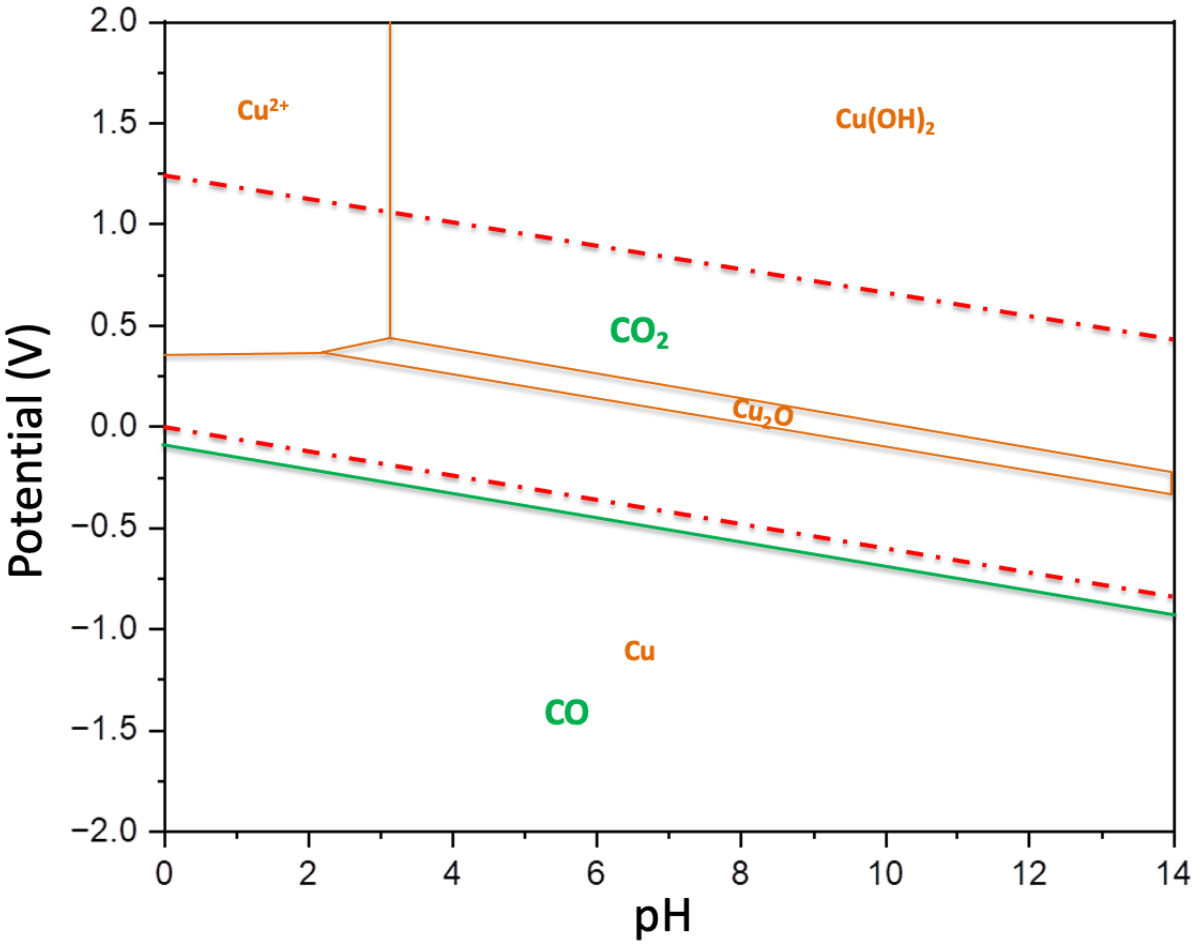

Figure 7.4. Pourbaix diagrams for copper and carbon systems at 25 °C. Cu_2O reduction occurs at +0.58 V vs RHE while CO_2 reduction to CO occurs at -0.1 V vs RHE. This was calculated using the HSC Chemistry 10.0 software package.(Roine, 2023) The potential required to reduce CO_2 to CO will simultaneously reduce Cu_2O to Cu. This unusual dynamic oxidation of Cu under cathodic potentials could be related to O_2 crossover and chemical oxidation of electrically disconnected Cu particles at the cathode.

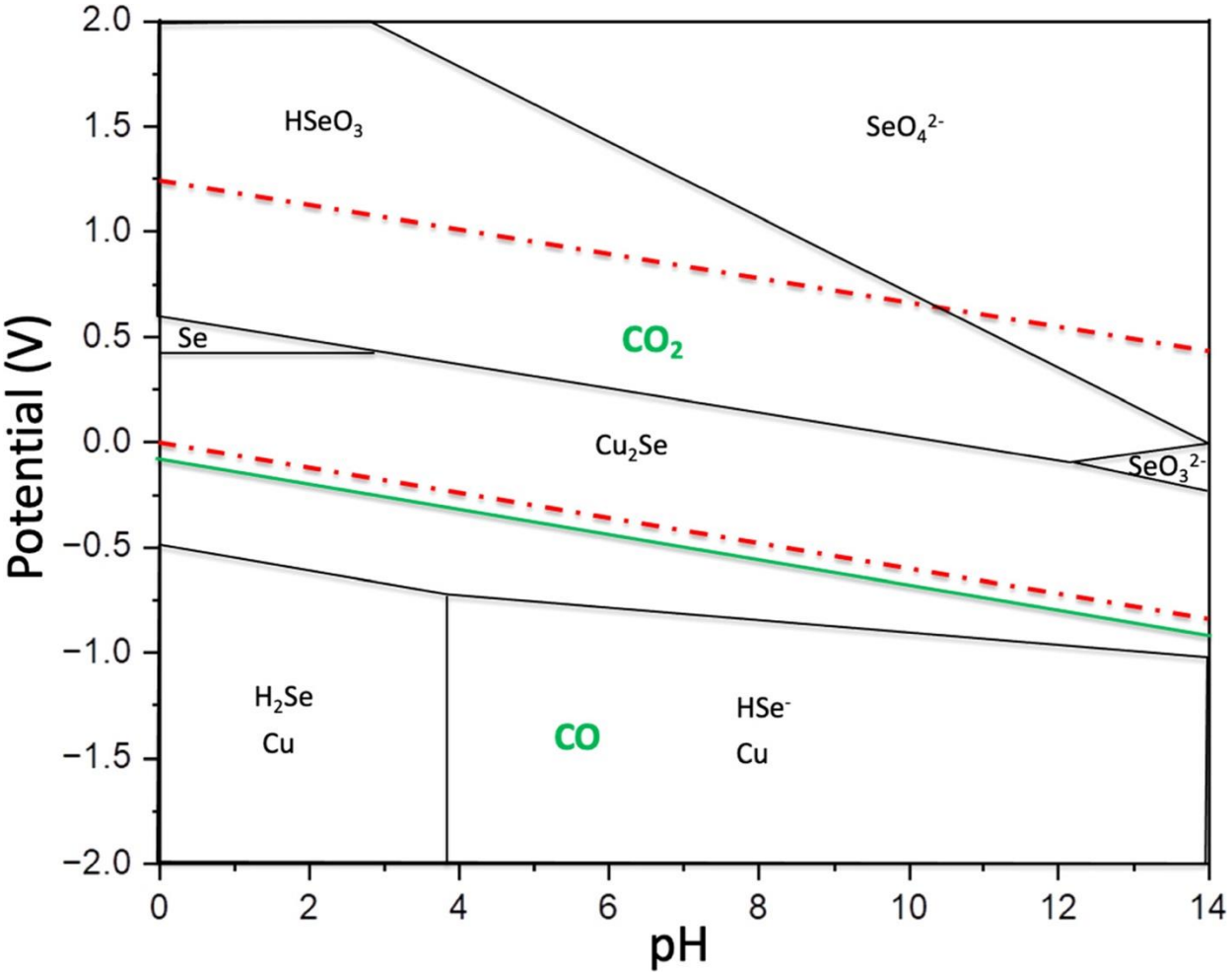

Figure 7.5. Pourbaix diagram for Cu-Se including the CO_2 to CO reaction at 25 °C. Cu_2Se reduction occurs at -0.58 V vs RHE and provides a stabile alkaline window for CO_2 reduction. Calculated using the HSC Chemistry 10.0 software package.(Roine, 2023)

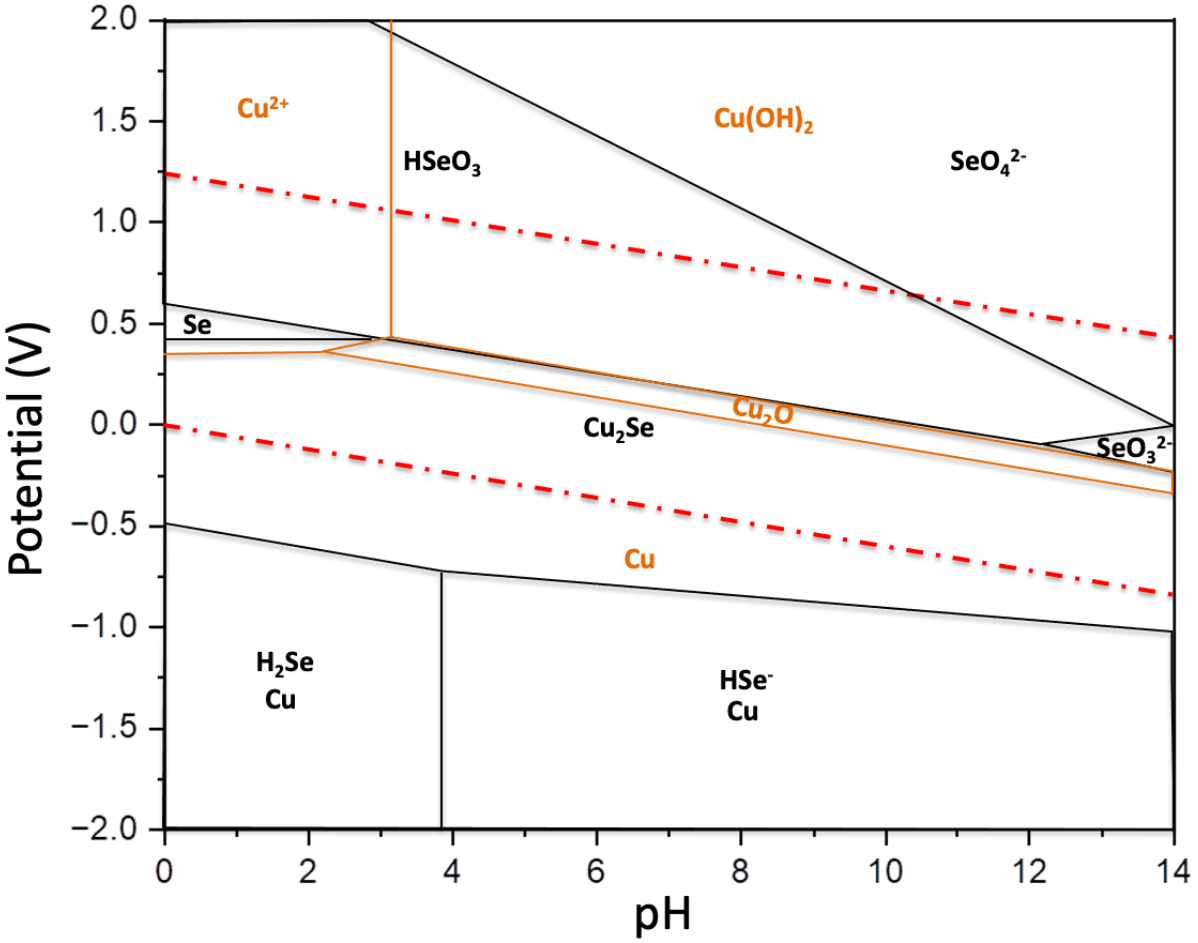

Figure 7.6. Pourbaix diagrams for copper and copper-selenium systems at 25 °C. Cu_2O reduction occurs at +0.58 V vs RHE and CO_2 reduction to CO occurs at -0.1 V vs RHE. This was calculated using the HSC Chemistry 10.0 software package.(Roine, 2023) The much lower reduction potential for Cu_2Se compared to Cu_2O suggests that electronegative selenium doping may enable relatively more active and stable Cu^+ species to form. Therefore, selenium or other electronegative dopants could potentially stabilize Cu^+ and lead to enhanced CO_2 reduction performance compared to pure copper systems.

7.5. Discussion

The durability testing of Cu-$P_{0.065}$, Cu-$Sn_{0.03}$, and Cu_2Se electrocatalysts for the electrochemical reduction of CO_2 has provided valuable insights into the long-term stability and performance of these materials under realistic operating conditions. The results highlight the challenges associated with maintaining the selectivity and activity of Cu-based electrocatalysts over extended periods of operation, as evidenced by the gradual changes in Faradaic efficiencies

and the increase in hydrogen evolution observed for all three electrocatalysts. The decline in selectivity towards the desired C_2 products, such as ethylene, ethanol, and acetate, and the concomitant increase in hydrogen evolution suggest a loss of catalytic specificity and an increased preference for the competing hydrogen evolution reaction (HER) pathway. These changes can be attributed to various factors, including the loss of heteroatom dopants, surface reconstruction, and the accumulation of carbonaceous species on the electrocatalyst surface.

The scanning electron microscopy (SEM) analyses provided valuable insights into the morphological transformations experienced by the electrocatalysts during the prolonged CO_2 electrolysis. The Cu-P and Cu-Sn electrocatalysts exhibited significant agglomeration and restructuring, with the initially spherical nanoparticles coalescing into larger cubic morphologies. This transformation suggests a susceptibility to sintering and restructuring processes under the applied electrochemical conditions, which could potentially compromise their catalytic activity and long-term stability. In contrast, the Cu-Se electrocatalyst demonstrated remarkable structural stability, with its nanoparticles remaining relatively intact and retaining their original morphology. This exceptional resilience is attributed to the strong Cu-Se interactions within the nanoparticles, highlighting the potential of the Cu-Se electrocatalyst for superior durability and sustained catalytic performance over extended periods of operation.

The ex-situ X-ray photoelectron spectroscopy (XPS) analyses revealed a consistent trend across all three electrocatalysts: an increase in the relative surface concentration of the metallic Cu0 species after prolonged electrolysis. While these results provide valuable insights into the changes in copper oxidation states, their interpretation is limited by potential re-oxidation during the time elapsed between electrolysis and analysis. To gain a more comprehensive understanding of the dynamic redox behavior and oxidation state changes during the CO_2 reduction process,

operando techniques such as time-resolved X-ray absorption spectroscopy (XAS) and in-situ Raman spectroscopy are essential. These techniques, coupled with thermodynamic considerations and complementary characterization methods, can elucidate the intricate interplay between electrocatalyst composition, oxidation states, and structural transformations, ultimately guiding the design of more active and stable electrocatalysts for CO_2 reduction applications.

The thermodynamic stability of electrocatalysts, as illustrated by the Pourbaix diagrams, plays a crucial role in their behavior and performance during CO_2 reduction reactions. The copper-selenium system, with its stable overpotential window for CO_2 reduction without compromising the oxidation state of the $Cu^{\delta+}$ species, showcases the potential benefits of incorporating electronegative dopants. The contrasting behavior observed between pure copper systems and the copper-selenium system highlights the influence of electronegative doping on stabilizing the desired oxidation states and potentially enhancing CO_2 reduction performance. By tuning the reduction potentials and stabilizing the desired oxidation states, these doped electrocatalysts could potentially mitigate undesired restructuring and improve catalytic activity and selectivity for CO_2 reduction applications.

7.6. Conclusion

In conclusion, the durability testing of Cu-$P_{0.065}$, Cu-$Sn_{0.03}$, and Cu_2Se electrocatalysts for the electrochemical reduction of CO_2 has provided valuable insights into the long-term stability and performance of these materials under realistic operating conditions. The gradual changes in Faradaic efficiencies and the increase in hydrogen evolution observed for all three electrocatalysts highlight the challenges associated with maintaining the selectivity and activity of Cu-based electrocatalysts over extended periods of operation. The morphological transformations revealed by SEM analyses, particularly the agglomeration and restructuring of the Cu-P and Cu-Sn

electrocatalysts, emphasize the importance of structural stability for sustained catalytic performance.

The ex-situ XPS analyses, while providing insights into the changes in copper oxidation states, underscore the need for operando techniques to gain a more comprehensive understanding of the dynamic redox behavior and oxidation state changes during the CO_2 reduction process. The thermodynamic stability considerations, as illustrated by the Pourbaix diagrams, highlight the potential benefits of incorporating electronegative dopants, such as selenium, into copper-based electrocatalysts. By tuning the reduction potentials and stabilizing the desired oxidation states, these doped electrocatalysts could potentially enhance structural stability, mitigate undesired restructuring, and ultimately improve catalytic activity and selectivity for CO_2 reduction applications.

Despite the challenges identified in this study, the Cu-$P_{0.065}$, Cu-$Sn_{0.03}$, and Cu_2Se electrocatalysts have demonstrated reasonable stability over the 220-hour durability test, indicating their potential for long-term operation with further optimization. Strategies to mitigate the loss of selectivity and activity, such as the development of more robust heteroatom doping techniques, the use of protective layers, and the incorporation of regeneration steps, could significantly enhance the durability and performance of these electrocatalysts. Furthermore, the insights gained from this study provide valuable guidance for the rational design and optimization of Cu-based electrocatalysts for efficient and selective CO_2 reduction.

In summary, this study highlights the importance of comprehensive durability testing under realistic operating conditions to assess the long-term stability and performance of Cu-based electrocatalysts for CO_2 reduction. The findings emphasize the need for a multifaceted approach, combining advanced characterization techniques, operando studies, and computational methods,

to unravel the complex interplay between electrocatalyst composition, structure, and performance. By addressing the identified challenges and leveraging the insights gained from this study, the development of highly active, selective, and durable Cu-based electrocatalysts for CO_2 reduction can be accelerated, paving the way for the practical implementation of this promising technology in the sustainable production of valuable chemicals and fuels.

REFERENCES

Albo, J., Alvarez-Guerra, M., Castaño, P., & Irabien, A. (2015). Towards the electrochemical conversion of carbon dioxide into methanol [10.1039/C4GC02453B]. Green Chemistry, 17(4), 2304-2324. https://doi.org/10.1039/C4GC02453B

Alerte, T., Edwards, J. P., Gabardo, C. M., O'Brien, C. P., Gaona, A., Wicks, J., Obradović, A., Sarkar, A., Jaffer, S. A., MacLean, H. L., Sinton, D., & Sargent, E. H. (2021). Downstream of the CO2 Electrolyzer: Assessing the Energy Intensity of Product Separation. ACS Energy Letters, 6(12), 4405-4412. https://doi.org/10.1021/acsenergylett.1c02263

Álvarez-Gómez, J. M., & Varela, A. S. (2023). Review on Long-Term Stability of Electrochemical CO2 Reduction. Energy & Fuels, 37(20), 15283-15308. https://doi.org/10.1021/acs.energyfuels.3c01847

Andrews, E., Ren, M., Wang, F., Zhang, Z., Sprunger, P., Kurtz, R., & Flake, J. (2013). Electrochemical Reduction of CO2 at Cu Nanocluster / (100) ZnO Electrodes. Journal of The Electrochemical Society, 160(11), H841. https://doi.org/10.1149/2.105311jes

Barcelos, M. M., Vasconcellos, M. d. L. S., & Ribeiro, J. (2024). Recent Progress in Electrochemical CO2 Reduction at Different Electrocatalyst Materials. Processes, 12(2), 303.

Baumgartner, L. M., Koopman, C. I., Forner-Cuenca, A., & Vermaas, D. A. (2022). Narrow Pressure Stability Window of Gas Diffusion Electrodes Limits the Scale-Up of CO2 Electrolyzers. ACS Sustainable Chemistry & Engineering, 10(14), 4683-4693. https://doi.org/10.1021/acssuschemeng.2c00195

Boetcher, S. K. S., Perskin, J. B., Maidenberg, Y., Traum, M. J., & von Hippel, T. (2023). Direct atmospheric cryogenic carbon capture in cold climates. Carbon Capture Science & Technology, 8, 100127. https://doi.org/https://doi.org/10.1016/j.ccst.2023.100127

Carroll, J. J., Slupsky, J. D., & Mather, A. E. (1991). The Solubility of Carbon Dioxide in Water at Low Pressure. Journal of Physical and Chemical Reference Data, 20(6), 1201-1209. https://doi.org/10.1063/1.555900

Chang, F., Xiao, M., Miao, R., Liu, Y., Ren, M., Jia, Z., Han, D., Yuan, Y., Bai, Z., & Yang, L. (2022). Copper-Based Catalysts for Electrochemical Carbon Dioxide Reduction to Multicarbon Products. Electrochemical Energy Reviews, 5(3), 4. https://doi.org/10.1007/s41918-022-00139-5

Chen, C., Sun, X., Lu, L., Yang, D., Ma, J., Zhu, Q., Qian, Q., & Han, B. (2018). Efficient electroreduction of CO2 to C2 products over B-doped oxide-derived copper. Green Chemistry, 20(20), 4579-4583. https://doi.org/10.1039/C8GC02389A

Chen, H., Wang, Z., Wei, X., Liu, S., Guo, P., Han, P., Wang, H., Zhang, J., Lu, X., & Wei, B. (2021). Promotion of electrochemical CO2 reduction to ethylene on phosphorus-doped

copper nanocrystals with stable Cuδ+ sites. Applied Surface Science, 544, 148965. https://doi.org/10.1016/j.apsusc.2021.148965

Chen, H., Zeng, J., Li, Y., Kang, C., Ding, C., Li, Y., Li, C., & He, J. (2023). Coupling electrochemical CO2 reduction to syngas with chloride-mediated dye degradation to CO2 in a one-compartment cell [10.1039/D3SE00709J]. Sustainable Energy & Fuels, 7(18), 4533-4539. https://doi.org/10.1039/D3SE00709J

Chen, X., Henckel, D. A., Nwabara, U. O., Li, Y., Frenkel, A. I., Fister, T. T., Kenis, P. J. A., & Gewirth, A. A. (2020). Controlling Speciation during CO2 Reduction on Cu-Alloy Electrodes. ACS Catalysis, 10(1), 672-682. https://doi.org/10.1021/acscatal.9b04368

Consortium*†, T. C. C. P. I. P., Hönisch, B., Royer, D. L., Breecker, D. O., Polissar, P. J., Bowen, G. J., Henehan, M. J., Cui, Y., Steinthorsdottir, M., McElwain, J. C., Kohn, M. J., Pearson, A., Phelps, S. R., Uno, K. T., Ridgwell, A., Anagnostou, E., Austermann, J., Badger, M. P. S., Barclay, R. S., . . . Zhang, L. (2023). Toward a Cenozoic history of atmospheric CO₂. Science, 382(6675), eadi5177. https://doi.org/doi:10.1126/science.adi5177

Costentin, C., Robert, M., & Savéant, J.-M. (2013). Catalysis of the electrochemical reduction of carbon dioxide [10.1039/C2CS35360A]. Chemical Society Reviews, 42(6), 2423-2436. https://doi.org/10.1039/C2CS35360A

Dauda, M. O., Hendershot, J., Bello, M., Park, J., Loaiza Orduz, A., Lombardo, N., Kizilkaya, O., Sprunger, P., Engler, A., Plaisance, C., & Flake, J. (2024). Electrochemical Reduction of CO2: A Common Acetyl Path to Ethylene, Ethanol or Acetate. Journal of The Electrochemical Society. http://iopscience.iop.org/article/10.1149/1945-7111/ad2cc1

De Luna, P., Quintero-Bermudez, R., Dinh, C.-T., Ross, M. B., Bushuyev, O. S., Todorović, P., Regier, T., Kelley, S. O., Yang, P., & Sargent, E. H. (2018). Catalyst electro-redeposition controls morphology and oxidation state for selective carbon dioxide reduction. Nature Catalysis, 1(2), 103-110. https://doi.org/10.1038/s41929-017-0018-9

Deng, Y., Huang, Y., Ren, D., Handoko, A. D., Seh, Z. W., Hirunsit, P., & Yeo, B. S. (2018). On the Role of Sulfur for the Selective Electrochemical Reduction of CO2 to Formate on CuS x Catalysts. ACS Applied Materials & Interfaces, 10(34), 28572-28581. https://doi.org/10.1021/acsami.8b08428

Ding, L., Zhu, N., Hu, Y., Chen, Z., Song, P., Sheng, T., Wu, Z., & Xiong, Y. (2022). Over 70 % Faradaic Efficiency for CO2 Electroreduction to Ethanol Enabled by Potassium Dopant-Tuned Interaction between Copper Sites and Intermediates. Angewandte Chemie International Edition, 61(36), e202209268. https://doi.org/10.1002/anie.202209268

Ding, M., Chen, Z., Liu, C., Wang, Y., Li, C., Li, X., Zheng, T., Jiang, Q., & Xia, C. (2023). Electrochemical CO2 reduction: Progress and opportunity with alloying copper. Materials Reports: Energy, 3(1), 100175. https://doi.org/https://doi.org/10.1016/j.matre.2023.100175

Dinh, C.-T., Burdyny, T., Kibria, M. G., Seifitokaldani, A., Gabardo, C. M., García de Arquer, F. P., Kiani, A., Edwards, J. P., De Luna, P., Bushuyev, O. S., Zou, C., Quintero-Bermudez, R., Pang, Y., Sinton, D., & Sargent, E. H. (2018). CO₂ electroreduction to ethylene via hydroxide-mediated copper catalysis at an abrupt interface. Science, 360(6390), 783-787. https://doi.org/doi:10.1126/science.aas9100

Fang, M., Wang, M., Wang, Z., Zhang, Z., Zhou, H., Dai, L., Zhu, Y., & Jiang, L. (2023). Hydrophobic, Ultrastable Cuδ+ for Robust CO2 Electroreduction to C2 Products at Ampere-Current Levels. Journal of the American Chemical Society, 145(20), 11323-11332. https://doi.org/10.1021/jacs.3c02399

Feaster, J. T., Shi, C., Cave, E. R., Hatsukade, T., Abram, D. N., Kuhl, K. P., Hahn, C., Nørskov, J. K., & Jaramillo, T. F. (2017). Understanding Selectivity for the Electrochemical Reduction of Carbon Dioxide to Formic Acid and Carbon Monoxide on Metal Electrodes. ACS Catalysis, 7(7), 4822-4827. https://doi.org/10.1021/acscatal.7b00687

Fontela, M., Pérez, F. F., Carracedo, L. I., Padín, X. A., Velo, A., García-Ibañez, M. I., & Lherminier, P. (2020). The Northeast Atlantic is running out of excess carbonate in the horizon of cold-water corals communities. Scientific Reports, 10(1), 14714. https://doi.org/10.1038/s41598-020-71793-2

Gabardo, C. M., O'Brien, C. P., Edwards, J. P., McCallum, C., Xu, Y., Dinh, C.-T., Li, J., Sargent, E. H., & Sinton, D. (2019). Continuous Carbon Dioxide Electroreduction to Concentrated Multi-carbon Products Using a Membrane Electrode Assembly. Joule, 3(11), 2777-2791. https://doi.org/https://doi.org/10.1016/j.joule.2019.07.021

Gabrielli, P., Rosa, L., Gazzani, M., Meys, R., Bardow, A., Mazzotti, M., & Sansavini, G. (2023). Net-zero emissions chemical industry in a world of limited resources. One Earth, 6(6), 682-704. https://doi.org/10.1016/j.oneear.2023.05.006

Gao, D., Wei, P., Li, H., Lin, L., Wang, G., & Bao, X. (2021). Designing Electrolyzers for Electrocatalytic CO2 Reduction 用于二氧化碳电催化还原的电解器研究进展. Chinese Journal of Inorganic Chemistry, 37(5).

García de Arquer, F. P., Dinh, C.-T., Ozden, A., Wicks, J., McCallum, C., Kirmani, A. R., Nam, D.-H., Gabardo, C., Seifitokaldani, A., Wang, X., Li, Y. C., Li, F., Edwards, J., Richter, L. J., Thorpe, S. J., Sinton, D., & Sargent, E. H. (2020). CO₂ electrolysis to multicarbon products at activities greater than 1 A cm^{−2}. Science, 367(6478), 661-666. https://doi.org/doi:10.1126/science.aay4217

Gawel, A., Jaster, T., Siegmund, D., Holzmann, J., Lohmann, H., Klemm, E., & Apfel, U.-P. (2022). Electrochemical CO2 reduction - The macroscopic world of electrode design, reactor concepts & economic aspects. iScience, 25(4), 104011. https://doi.org/https://doi.org/10.1016/j.isci.2022.104011

Ge, L., Rabiee, H., Li, M., Subramanian, S., Zheng, Y., Lee, J. H., Burdyny, T., & Wang, H. (2022). Electrochemical CO2 reduction in membrane-electrode assemblies. Chem, 8(3), 663-692. https://doi.org/https://doi.org/10.1016/j.chempr.2021.12.002

Habibzadeh, F., Mardle, P., Zhao, N., Riley, H. D., Salvatore, D. A., Berlinguette, C. P., Holdcroft, S., & Shi, Z. (2023). Ion Exchange Membranes in Electrochemical CO2 Reduction Processes. Electrochemical Energy Reviews, 6(1), 26. https://doi.org/10.1007/s41918-023-00183-9

Hasa, B., Cherniack, L., Xia, R., Tian, D., Ko, B. H., Overa, S., Dimitrakellis, P., Bae, C., & Jiao, F. (2023). Benchmarking anion-exchange membranes for electrocatalytic carbon monoxide reduction. Chem Catalysis, 3(1).

Higgins, D., Hahn, C., Xiang, C., Jaramillo, T. F., & Weber, A. Z. (2019). Gas-Diffusion Electrodes for Carbon Dioxide Reduction: A New Paradigm. ACS Energy Letters, 4(1), 317-324. https://doi.org/10.1021/acsenergylett.8b02035

Hori, Y. (2008). Electrochemical CO2 Reduction on Metal Electrodes. In C. G. Vayenas, R. E. White, & M. E. Gamboa-Aldeco (Eds.), Modern Aspects of Electrochemistry (pp. 89-189). Springer. https://doi.org/10.1007/978-0-387-49489-0_3

Hori, Y., Kikuchi, K., & Suzuki, S. (1985). PRODUCTION OF CO AND CH4 IN ELECTROCHEMICAL REDUCTION OF CO2 AT METAL ELECTRODES IN AQUEOUS HYDROGENCARBONATE SOLUTION. Chemistry Letters, 14(11), 1695-1698. https://doi.org/10.1246/cl.1985.1695

Hori, Y., Murata, A., & Takahashi, R. (1989). Formation of hydrocarbons in the electrochemical reduction of carbon dioxide at a copper electrode in aqueous solution [10.1039/F19898502309]. Journal of the Chemical Society, Faraday Transactions 1: Physical Chemistry in Condensed Phases, 85(8), 2309-2326. https://doi.org/10.1039/F19898502309

Hori, Y., Murata, A., Takahashi, R., & Suzuki, S. (1987). Electroreduction of carbon monoxide to methane and ethylene at a copper electrode in aqueous solutions at ambient temperature and pressure. Journal of the American Chemical Society, 109(16), 5022-5023. https://doi.org/10.1021/ja00250a044

Hori, Y., Takahashi, I., Koga, O., & Hoshi, N. (2003). Electrochemical reduction of carbon dioxide at various series of copper single crystal electrodes. Journal of Molecular Catalysis A: Chemical, 199(1), 39-47. https://doi.org/https://doi.org/10.1016/S1381-1169(03)00016-5

Huang, J. E., Li, F., Ozden, A., Sedighian Rasouli, A., García de Arquer, F. P., Liu, S., Zhang, S., Luo, M., Wang, X., Lum, Y., Xu, Y., Bertens, K., Miao, R. K., Dinh, C. T., Sinton, D., & Sargent, E. H. (2021). CO(2) electrolysis to multicarbon products in strong acid. Science, 372(6546), 1074-1078. https://doi.org/10.1126/science.abg6582

Jeng, E., Qi, Z., Kashi, A. R., Hunegnaw, S., Huo, Z., Miller, J. S., Bayu Aji, L. B., Ko, B. H., Shin, H., Ma, S., Kuhl, K. P., Jiao, F., & Biener, J. (2022). Scalable Gas Diffusion Electrode Fabrication for Electrochemical CO2 Reduction Using Physical Vapor Deposition Methods. ACS Applied Materials & Interfaces, 14(6), 7731-7740. https://doi.org/10.1021/acsami.1c17860

Jia, Y., Li, F., Fan, K., & Sun, L. (2022). Cu-based bimetallic electrocatalysts for CO2 reduction. Advanced Powder Materials, 1(1), 100012. https://doi.org/https://doi.org/10.1016/j.apmate.2021.10.003

Jiang, K., Huang, Y., Zeng, G., Toma, F. M., Goddard III, W. A., & Bell, A. T. (2020). Effects of surface roughness on the electrochemical reduction of CO2 over Cu. ACS Energy Letters, 5(4), 1206-1214.

Jones, J.-P., Prakash, G. K. S., & Olah, G. A. (2014). Electrochemical CO2 Reduction: Recent Advances and Current Trends. Israel Journal of Chemistry, 54(10), 1451-1466. https://doi.org/https://doi.org/10.1002/ijch.201400081

Ju, W., Jiang, F., Ma, H., Pan, Z., Zhao, Y.-B., Pagani, F., Rentsch, D., Wang, J., & Battaglia, C. (2019). Electrocatalytic Reduction of Gaseous CO2 to CO on Sn/Cu-Nanofiber-Based Gas Diffusion Electrodes. Advanced Energy Materials, 9(32), 1901514. https://doi.org/https://doi.org/10.1002/aenm.201901514

Ju, W., Zeng, J., Bejtka, K., Ma, H., Rentsch, D., Castellino, M., Sacco, A., Pirri, C. F., & Battaglia, C. (2019). Sn-Decorated Cu for Selective Electrochemical CO2 to CO Conversion: Precision Architecture beyond Composition Design. ACS Applied Energy Materials, 2(1), 867-872. https://doi.org/10.1021/acsaem.8b01944

Karapinar, D., Huan, N. T., Ranjbar Sahraie, N., Li, J., Wakerley, D., Touati, N., Zanna, S., Taverna, D., Galvão Tizei, L. H., Zitolo, A., Jaouen, F., Mougel, V., & Fontecave, M. (2019). Electroreduction of CO2 on Single-Site Copper-Nitrogen-Doped Carbon Material: Selective Formation of Ethanol and Reversible Restructuration of the Metal Sites. Angewandte Chemie International Edition, 58(42), 15098-15103. https://doi.org/https://doi.org/10.1002/anie.201907994

Kim, B., Hillman, F., Ariyoshi, M., Fujikawa, S., & Kenis, P. J. A. (2016). Effects of composition of the micro porous layer and the substrate on performance in the electrochemical reduction of CO2 to CO. Journal of Power Sources, 312, 192-198. https://doi.org/https://doi.org/10.1016/j.jpowsour.2016.02.043

Kim, D., Lee, S., Ocon, J. D., Jeong, B., Lee, J. K., & Lee, J. (2015). Insights into an autonomously formed oxygen-evacuated Cu2O electrode for the selective production of C2H4 from CO2 [10.1039/C4CP03172E]. Physical Chemistry Chemical Physics, 17(2), 824-830. https://doi.org/10.1039/C4CP03172E

Kim, D., Resasco, J., Yu, Y., Asiri, A. M., & Yang, P. (2014). Synergistic geometric and electronic effects for electrochemical reduction of carbon dioxide using gold–copper bimetallic nanoparticles. Nature Communications, 5(1), 4948. https://doi.org/10.1038/ncomms5948

Kong, X., Wang, C., Zheng, H., Geng, Z., Bao, J., & Zeng, J. (2021). Enhance the activity of multi-carbon products for Cu via P doping towards CO2 reduction. Science China Chemistry, 64(7), 1096-1102. https://doi.org/10.1007/s11426-020-9934-0

Küngas, R. (2020). Review—Electrochemical CO2 Reduction for CO Production: Comparison of Low- and High-Temperature Electrolysis Technologies. Journal of The Electrochemical Society, 167(4), 044508. https://doi.org/10.1149/1945-7111/ab7099

Kutz, R. B., Chen, Q., Yang, H., Sajjad, S. D., Liu, Z., & Masel, I. R. (2017). Sustainion Imidazolium-Functionalized Polymers for Carbon Dioxide Electrolysis. Energy Technology, 5(6), 929-936. https://doi.org/https://doi.org/10.1002/ente.201600636

Le, M., Ren, M., Zhang, Z., Sprunger, P. T., Kurtz, R. L., & Flake, J. C. (2011). Electrochemical Reduction of CO2 to CH3OH at Copper Oxide Surfaces. Journal of The Electrochemical Society, 158(5), E45. https://doi.org/10.1149/1.3561636

Lee, S., Kim, D., & Lee, J. (2015). Electrocatalytic Production of C3-C4 Compounds by Conversion of CO2 on a Chloride-Induced Bi-Phasic Cu2O-Cu Catalyst. Angewandte Chemie International Edition, 54(49), 14701-14705. https://doi.org/https://doi.org/10.1002/anie.201505730

Lees, E. W., Mowbray, B. A. W., Parlane, F. G. L., & Berlinguette, C. P. (2022). Gas diffusion electrodes and membranes for CO2 reduction electrolysers. Nature Reviews Materials, 7(1), 55-64. https://doi.org/10.1038/s41578-021-00356-2

Li, H., Qin, X., Jiang, T., Ma, X.-Y., Jiang, K., & Cai, W.-B. (2019). Changing the Product Selectivity for Electrocatalysis of CO2 Reduction Reaction on Plated Cu Electrodes. ChemCatChem, 11(24), 6139-6146. https://doi.org/10.1002/cctc.201901748

Li, M., Song, N., Luo, W., Chen, J., Jiang, W., & Yang, J. (2023). Engineering Surface Oxophilicity of Copper for Electrochemical CO2 Reduction to Ethanol. Advanced Science, 10(2), 2204579. https://doi.org/10.1002/advs.202204579

Li, Y., Chen, Y., Chen, T., Shi, G., Zhu, L., Sun, Y., & Yu, M. (2023). Insight into the Electrochemical CO2-to-Ethanol Conversion Catalyzed by Cu2S Nanocrystal-Decorated Cu Nanosheets. ACS Applied Materials & Interfaces, 15(15), 18857-18866. https://doi.org/10.1021/acsami.3c00032

Li, Y. C., Yan, Z., Hitt, J., Wycisk, R., Pintauro, P. N., & Mallouk, T. E. (2018). Bipolar Membranes Inhibit Product Crossover in CO2 Electrolysis Cells. Advanced Sustainable Systems, 2(4), 1700187. https://doi.org/https://doi.org/10.1002/adsu.201700187

Liang, S., Altaf, N., Huang, L., Gao, Y., & Wang, Q. (2020). Electrolytic cell design for electrochemical CO2 reduction. Journal of CO2 Utilization, 35, 90-105. https://doi.org/10.1016/j.jcou.2019.09.007

Liang, Z.-Q., Zhuang, T.-T., Seifitokaldani, A., Li, J., Huang, C.-W., Tan, C.-S., Li, Y., De Luna, P., Dinh, C. T., Hu, Y., Xiao, Q., Hsieh, P.-L., Wang, Y., Li, F., Quintero-Bermudez, R., Zhou, Y., Chen, P., Pang, Y., Lo, S.-C., . . . Sargent, E. H. (2018). Copper-on-nitride enhances the stable electrosynthesis of multi-carbon products from CO2. Nature Communications, 9(1), 3828. https://doi.org/10.1038/s41467-018-06311-0

Lin, J., Zhang, Y., Xu, P., & Chen, L. (2023). CO2 electrolysis: Advances and challenges in electrocatalyst engineering and reactor design. Materials Reports: Energy, 3(2), 100194. https://doi.org/10.1016/j.matre.2023.100194 (CO2 Reductions to Fuels and Carbon Feedstocks (Part 2))

Liu, W., Li, H., Ou, P., Mao, J., Han, L., Song, J., Luo, J., & Xin, H. L. (2023). Isolated Cu-Sn diatomic sites for enhanced electroreduction of CO2 to CO. Nano Research, 16(7), 8729-8736. https://doi.org/10.1007/s12274-023-5513-5

Liu, X., Xiao, J., Peng, H., Hong, X., Chan, K., & Nørskov, J. K. (2017). Understanding trends in electrochemical carbon dioxide reduction rates. Nature Communications, 8(1), 15438. https://doi.org/10.1038/ncomms15438

Lu, X. K., Lu, B., Li, H., Lim, K., & Seitz, L. C. (2022). Stabilization of Undercoordinated Cu Sites in Strontium Copper Oxides for Enhanced Formation of C2+ Products in Electrochemical CO2 Reduction. ACS Catalysis, 12(11), 6663-6671. https://doi.org/10.1021/acscatal.2c01019

Lum, Y., Yue, B., Lobaccaro, P., Bell, A. T., & Ager, J. W. (2017). Optimizing C–C Coupling on Oxide-Derived Copper Catalysts for Electrochemical CO2 Reduction. The Journal of Physical Chemistry C, 121(26), 14191-14203. https://doi.org/10.1021/acs.jpcc.7b03673

Lüthi, D., Le Floch, M., Bereiter, B., Blunier, T., Barnola, J.-M., Siegenthaler, U., Raynaud, D., Jouzel, J., Fischer, H., Kawamura, K., & Stocker, T. F. (2008). High-resolution carbon dioxide concentration record 650,000–800,000 years before present. Nature, 453(7193), 379-382. https://doi.org/10.1038/nature06949

Ma, D., Jin, T., Xie, K., & Huang, H. (2021). An overview of flow cell architecture design and optimization for electrochemical CO2 reduction [10.1039/D1TA06101A]. Journal of Materials Chemistry A, 9(37), 20897-20918. https://doi.org/10.1039/D1TA06101A

Ma , S., Lan , Y., Perez, G. M. J., Moniri, S., & Kenis , P. J. A. (2014). Silver Supported on Titania as an Active Catalyst for Electrochemical Carbon Dioxide Reduction. ChemSusChem, 7(3), 866-874. https://doi.org/https://doi.org/10.1002/cssc.201300934

Ma, S., Luo, R., Moniri, S., Lan, Y., & Kenis, P. J. A. (2014). Efficient Electrochemical Flow System with Improved Anode for the Conversion of CO2 to CO. Journal of The Electrochemical Society, 161(10), F1124. https://doi.org/10.1149/2.1201410jes

Ma, S., Sadakiyo, M., Luo, R., Heima, M., Yamauchi, M., & Kenis, P. J. A. (2016). One-step electrosynthesis of ethylene and ethanol from CO2 in an alkaline electrolyzer. Journal of Power Sources, 301, 219-228. https://doi.org/https://doi.org/10.1016/j.jpowsour.2015.09.124

Mandal, L., Yang, K. R., Motapothula, M. R., Ren, D., Lobaccaro, P., Patra, A., Sherburne, M., Batista, V. S., Yeo, B. S., Ager, J. W., Martin, J., & Venkatesan, T. (2018). Investigating the Role of Copper Oxide in Electrochemical CO2 Reduction in Real Time. ACS Applied Materials & Interfaces, 10(10), 8574-8584. https://doi.org/10.1021/acsami.7b15418

McCallum, C., Gabardo, C. M., O'Brien, C. P., Edwards, J. P., Wicks, J., Xu, Y., Sargent, E. H., & Sinton, D. (2021). Reducing the crossover of carbonate and liquid products during carbon dioxide electroreduction. Cell Reports Physical Science, 2(8), 100522. https://doi.org/https://doi.org/10.1016/j.xcrp.2021.100522

Merino-Garcia, I., Albo, J., Solla-Gullón, J., Montiel, V., & Irabien, A. (2019). Cu oxide/ZnO-based surfaces for a selective ethylene production from gas-phase CO2 electroconversion. Journal of CO2 Utilization, 31, 135-142. https://doi.org/https://doi.org/10.1016/j.jcou.2019.03.002

Mistry, H., Varela, A. S., Bonifacio, C. S., Zegkinoglou, I., Sinev, I., Choi, Y.-W., Kisslinger, K., Stach, E. A., Yang, J. C., Strasser, P., & Cuenya, B. R. (2016). Highly selective plasma-activated copper catalysts for carbon dioxide reduction to ethylene. Nature Communications, 7(1), 12123. https://doi.org/10.1038/ncomms12123

Morimoto, M., Takatsuji, Y., Yamasaki, R., Hashimoto, H., Nakata, I., Sakakura, T., & Haruyama, T. (2018). Electrodeposited Cu-Sn Alloy for Electrochemical CO2 Reduction to CO/HCOO−. Electrocatalysis, 9(3), 323-332. https://doi.org/10.1007/s12678-017-0434-2

Neftel, A., Oeschger, H., Staffelbach, T., & Stauffer, B. (1988). CO2 record in the Byrd ice core 50,000–5,000 years bp. Nature, 331(6157), 609-611. https://doi.org/10.1038/331609a0

Ni, Z., Liang, H., Yi, Z., Guo, R., Liu, C., Liu, Y., Sun, H., & Liu, X. (2021). Research progress of electrochemical CO2 reduction for copper-based catalysts to multicarbon products. Coordination Chemistry Reviews, 441, 213983. https://doi.org/https://doi.org/10.1016/j.ccr.2021.213983

Nitopi, S., Bertheussen, E., Scott, S. B., Liu, X., Engstfeld, A. K., Horch, S., Seger, B., Stephens, I. E. L., Chan, K., Hahn, C., Nørskov, J. K., Jaramillo, T. F., & Chorkendorff, I. (2019). Progress and Perspectives of Electrochemical CO2 Reduction on Copper in Aqueous Electrolyte. Chemical Reviews, 119(12), 7610-7672. https://doi.org/10.1021/acs.chemrev.8b00705

Nwabara, U. O., Cofell, E. R., Verma, S., Negro, E., & Kenis, P. J. A. (2020). Durable Cathodes and Electrolyzers for the Efficient Aqueous Electrochemical Reduction of CO2. ChemSusChem, 13(5), 855-875. https://doi.org/10.1002/cssc.201902933

O'Brien, C. P., Miao, R. K., Liu, S., Xu, Y., Lee, G., Robb, A., Huang, J. E., Xie, K., Bertens, K., Gabardo, C. M., Edwards, J. P., Dinh, C.-T., Sargent, E. H., & Sinton, D. (2021). Single Pass CO2 Conversion Exceeding 85% in the Electrosynthesis of Multicarbon Products via Local CO2 Regeneration. ACS Energy Letters, 6(8), 2952-2959. https://doi.org/10.1021/acsenergylett.1c01122

Overa, S., Ko, B. H., Zhao, Y., & Jiao, F. (2022). Electrochemical Approaches for CO2 Conversion to Chemicals: A Journey toward Practical Applications. Accounts of Chemical Research, 55(5), 638-648. https://doi.org/10.1021/acs.accounts.1c00674

Pan, Y., Wu, M., Ye, Z., Tang, H., Hong, Z., & Zhi, M. (2023). Cu-Sn Aerogels for Electrochemical CO2 Reduction with High CO Selectivity. Molecules, 28(3), 1033. https://www.mdpi.com/1420-3049/28/3/1033

Park, S., Lee, J.-W., & Popov, B. N. (2012). A review of gas diffusion layer in PEM fuel cells: Materials and designs. International Journal of Hydrogen Energy, 37(7), 5850-5865. https://doi.org/10.1016/j.ijhydene.2011.12.148 (XII International Symposium on Polymer Electrolytes: New Materials for Application in Proton Exchange Membrane Fuel Cells)

Peterson, A. A., & Nørskov, J. K. (2012). Activity Descriptors for CO2 Electroreduction to Methane on Transition-Metal Catalysts. The Journal of Physical Chemistry Letters, 3(2), 251-258. https://doi.org/10.1021/jz201461p

Petrov, K. V., Bui, J. C., Baumgartner, L., Weng, L. C., Dischinger, S. M., Larson, D. M., Miller, D. J., Weber, A. Z., & Vermaas, D. A. (2022). Anion-exchange membranes with internal microchannels for water control in CO(2) electrolysis. Sustain Energy Fuels, 6(22), 5077-5088. https://doi.org/10.1039/d2se00858k

Phillips, K. R., Katayama, Y., Hwang, J., & Shao-Horn, Y. (2018). Sulfide-Derived Copper for Electrochemical Conversion of CO(2) to Formic Acid. J Phys Chem Lett, 9(15), 4407-4412. https://doi.org/10.1021/acs.jpclett.8b01601

Rabiee, H., Zhang, X., Ge, L., Hu, S., Li, M., Smart, S., Zhu, Z., & Yuan, Z. (2020). Tuning the Product Selectivity of the Cu Hollow Fiber Gas Diffusion Electrode for Efficient CO2 Reduction to Formate by Controlled Surface Sn Electrodeposition. ACS Applied Materials & Interfaces, 12(19), 21670-21681. https://doi.org/10.1021/acsami.0c03681

Roduner, E. (2014). Understanding catalysis. Chemical Society Reviews, 43(24), 8226-8239.

Roine, A. (2023). HSC Chemistry Database 10. Metso. http://www.metso.com/hsc

Romiluyi, O., Danilovic, N., Bell, A. T., & Weber, A. Z. (2023). Membrane-electrode assembly design parameters for optimal CO2 reduction. Electrochemical Science Advances, 3(1), e2100186. https://doi.org/https://doi.org/10.1002/elsa.202100186

Salvatore, D. A., Gabardo, C. M., Reyes, A., O'Brien, C. P., Holdcroft, S., Pintauro, P., Bahar, B., Hickner, M., Bae, C., Sinton, D., Sargent, E. H., & Berlinguette, C. P. (2021). Designing anion exchange membranes for CO2 electrolysers. Nature Energy, 6(4), 339-348. https://doi.org/10.1038/s41560-020-00761-x

Sarfraz, S., Garcia-Esparza, A. T., Jedidi, A., Cavallo, L., & Takanabe, K. (2016). Cu–Sn Bimetallic Catalyst for Selective Aqueous Electroreduction of CO2 to CO. ACS Catalysis, 6(5), 2842-2851. https://doi.org/10.1021/acscatal.6b00269

Sassenburg, M., Kelly, M., Subramanian, S., Smith, W. A., & Burdyny, T. (2023). Zero-Gap Electrochemical CO2 Reduction Cells: Challenges and Operational Strategies for Prevention of Salt Precipitation. ACS Energy Letters, 8(1), 321-331. https://doi.org/10.1021/acsenergylett.2c01885

Saxena, A., Liyanage, W., Masud, J., Kapila, S., & Nath, M. (2021). Selective electroreduction of CO2 to carbon-rich products with a simple binary copper selenide electrocatalyst. Journal of Materials Chemistry A, 9(11), 7150-7161. https://doi.org/10.1039/D0TA11518E

Schouten, K. J. P., Qin, Z., Pérez Gallent, E., & Koper, M. T. M. (2012). Two Pathways for the Formation of Ethylene in CO Reduction on Single-Crystal Copper Electrodes. Journal of the American Chemical Society, 134(24), 9864-9867. https://doi.org/10.1021/ja302668n

Shang, L., Lv, X., Zhong, L., Li, S., & Zheng, G. (2022). Efficient CO2 Electroreduction to Ethanol by Cu3Sn Catalyst. Small Methods, 6(2), 2101334. https://doi.org/10.1002/smtd.202101334

Sharifian, R., Wagterveld, R. M., Digdaya, I. A., Xiang, C., & Vermaas, D. A. (2021). Electrochemical carbon dioxide capture to close the carbon cycle [10.1039/D0EE03382K]. Energy & Environmental Science, 14(2), 781-814. https://doi.org/10.1039/D0EE03382K

Tamimi, A., Rinker, E. B., & Sandall, O. C. (1994). Diffusion coefficients for hydrogen sulfide, carbon dioxide, and nitrous oxide in water over the temperature range 293-368 K. Journal of Chemical and Engineering data, 39(2), 330-332.

Tan, Y. C., Lee, K. B., Song, H., & Oh, J. (2020). Modulating Local CO2 Concentration as a General Strategy for Enhancing C−C Coupling in CO2 Electroreduction. Joule, 4(5), 1104-1120. https://doi.org/https://doi.org/10.1016/j.joule.2020.03.013

Timoshenko, J., Bergmann, A., Rettenmaier, C., Herzog, A., Arán-Ais, R. M., Jeon, H. S., Haase, F. T., Hejral, U., Grosse, P., Kühl, S., Davis, E. M., Tian, J., Magnussen, O., & Roldan Cuenya, B. (2022). Steering the structure and selectivity of CO2 electroreduction catalysts by potential pulses. Nature Catalysis, 5(4), 259-267. https://doi.org/10.1038/s41929-022-00760-z

Tornow, C. E., Thorson, M. R., Ma, S., Gewirth, A. A., & Kenis, P. J. A. (2012). Nitrogen-Based Catalysts for the Electrochemical Reduction of CO2 to CO. Journal of the American Chemical Society, 134(48), 19520-19523. https://doi.org/10.1021/ja308217w

Us Department of Commerce, N. Global Monitoring Laboratory - Carbon Cycle Greenhouse Gases. https://gml.noaa.gov/ccgg/trends/files/1042/trends.html

Vasileff, A., Zhi, X., Xu, C., Ge, L., Jiao, Y., Zheng, Y., & Qiao, S.-Z. (2019). Selectivity Control for Electrochemical CO2 Reduction by Charge Redistribution on the Surface of Copper Alloys. ACS Catalysis, 9(10), 9411-9417. https://doi.org/10.1021/acscatal.9b02312

Vermaas, D. A., & Smith, W. A. (2016). Synergistic Electrochemical CO2 Reduction and Water Oxidation with a Bipolar Membrane. ACS Energy Letters, 1(6), 1143-1148. https://doi.org/10.1021/acsenergylett.6b00557

Wakerley, D., Lamaison, S., Wicks, J., Clemens, A., Feaster, J., Corral, D., Jaffer, S. A., Sarkar, A., Fontecave, M., Duoss, E. B., Baker, S., Sargent, E. H., Jaramillo, T. F., & Hahn, C.

(2022). Gas diffusion electrodes, reactor designs and key metrics of low-temperature CO2 electrolysers. Nature Energy, 7(2), 130-143. https://doi.org/10.1038/s41560-021-00973-9

Wang, H., Xue, J., Liu, C., Chen, Z., Li, C., Li, X., Zheng, T., Jiang, Q., & Xia, C. (2023). CO2 electrolysis toward acetate: A review. Current Opinion in Electrochemistry, 39, 101253. https://doi.org/https://doi.org/10.1016/j.coelec.2023.101253

Wang, J.-S., Zhao, G.-C., Qiu, Y.-Q., & Liu, C.-G. (2021). Strong Boron–Carbon Bonding Interaction Drives CO2 Reduction to Ethanol over the Boron-Doped Cu(111) Surface: An Insight from the First-Principles Calculations. The Journal of Physical Chemistry C, 125(1), 572-582. https://doi.org/10.1021/acs.jpcc.0c09661

Wang, J., Tan, H.-Y., Zhu, Y., Chu, H., & Chen, H. M. (2021). Linking the Dynamic Chemical State of Catalysts with the Product Profile of Electrocatalytic CO2 Reduction. Angewandte Chemie International Edition, 60(32), 17254-17267. https://doi.org/https://doi.org/10.1002/anie.202017181

Wang, X., Klingan, K., Klingenhof, M., Möller, T., Ferreira de Araújo, J., Martens, I., Bagger, A., Jiang, S., Rossmeisl, J., Dau, H., & Strasser, P. (2021). Morphology and mechanism of highly selective Cu(II) oxide nanosheet catalysts for carbon dioxide electroreduction. Nature Communications, 12(1), 794. https://doi.org/10.1038/s41467-021-20961-7

Wang, Y., Shen, H., Livi, K. J. T., Raciti, D., Zong, H., Gregg, J., Onadeko, M., Wan, Y., Watson, A., & Wang, C. (2019). Copper Nanocubes for CO(2) Reduction in Gas Diffusion Electrodes. Nano Lett, 19(12), 8461-8468. https://doi.org/10.1021/acs.nanolett.9b02748

Wang, Z., Zhou, Y., Qiu, P., Xia, C., Fang, W., Jin, J., Huang, L., Deng, P., Su, Y., Crespo-Otero, R., Tian, X., You, B., Guo, W., Di Tommaso, D., Pang, Y., Ding, S., & Xia, B. Y. (2023). Advanced Catalyst Design and Reactor Configuration Upgrade in Electrochemical Carbon Dioxide Conversion. Advanced Materials, 35(52), 2303052. https://doi.org/https://doi.org/10.1002/adma.202303052

Weekes, D. M., Salvatore, D. A., Reyes, A., Huang, A., & Berlinguette, C. P. (2018). Electrolytic CO2 Reduction in a Flow Cell. Accounts of Chemical Research, 51(4), 910-918. https://doi.org/10.1021/acs.accounts.8b00010

Wei, P., Li, H., Lin, L., Gao, D., Zhang, X., Gong, H., Qing, G., Cai, R., Wang, G., & Bao, X. (2020). CO2 electrolysis at industrial current densities using anion exchange membrane based electrolyzers. Science China Chemistry, 63(12), 1711-1715. https://doi.org/10.1007/s11426-020-9825-9

Weng, L.-C., Bell, A. T., & Weber, A. Z. (2019). Towards membrane-electrode assembly systems for CO2 reduction: a modeling study [10.1039/C9EE00909D]. Energy & Environmental Science, 12(6), 1950-1968. https://doi.org/10.1039/C9EE00909D

Whipple, D. T., Finke, E. C., & Kenis, P. J. A. (2010). Microfluidic Reactor for the Electrochemical Reduction of Carbon Dioxide: The Effect of pH. Electrochemical and Solid-State Letters, 13(9), B109. https://doi.org/10.1149/1.3456590

Wierzbicki, S., Douglin, J. C., Kostuch, A., Dekel, D. R., & Kruczała, K. (2020). Are Radicals Formed During Anion-Exchange Membrane Fuel Cell Operation? The Journal of Physical Chemistry Letters, 11(18), 7630-7636. https://doi.org/10.1021/acs.jpclett.0c02349

Wood, D., Davey, J., Atanassov, P., & Borup, R. (2006). PEMFC Component Characterization and Its Relationship to Mass-Transport Overpotentials during Long-Term Testing. ECS Transactions, 3(1), 753. https://doi.org/10.1149/1.2356195

Wu, H., Li, J., Qi, K., Zhang, Y., Petit, E., Wang, W., Flaud, V., Onofrio, N., Rebiere, B., Huang, L., Salameh, C., Lajaunie, L., Miele, P., & Voiry, D. (2021). Improved electrochemical conversion of CO2 to multicarbon products by using molecular doping. Nature Communications, 12(1), 7210. https://doi.org/10.1038/s41467-021-27456-5

Xia, W., Xie, Y., Jia, S., Han, S., Qi, R., Chen, T., Xing, X., Yao, T., Zhou, D., Dong, X., Zhai, J., Li, J., He, J., Jiang, D., Yamauchi, Y., He, M., Wu, H., & Han, B. (2023). Adjacent Copper Single Atoms Promote C–C Coupling in Electrochemical CO2 Reduction for the Efficient Conversion of Ethanol. Journal of the American Chemical Society, 145(31), 17253-17264. https://doi.org/10.1021/jacs.3c04612

Xiang, F., & Jin, B. (2023). Study on electrochemical reduction mechanism of p-nitrophenylacetic acid prepared by electrocarboxylation. Journal of Electroanalytical Chemistry, 937, 117408. https://doi.org/10.1016/j.jelechem.2023.117408

Xiang, H., Rasul, S., Scott, K., Portoles, J., Cumpson, P., & Yu, E. H. (2019). Enhanced selectivity of carbonaceous products from electrochemical reduction of CO2 in aqueous media. Journal of CO2 Utilization, 30, 214-221. https://doi.org/https://doi.org/10.1016/j.jcou.2019.02.007

Xie, K., Miao, R. K., Ozden, A., Liu, S., Chen, Z., Dinh, C.-T., Huang, J. E., Xu, Q., Gabardo, C. M., Lee, G., Edwards, J. P., O'Brien, C. P., Boettcher, S. W., Sinton, D., & Sargent, E. H. (2022). Bipolar membrane electrolyzers enable high single-pass CO2 electroreduction to multicarbon products. Nature Communications, 13(1), 3609. https://doi.org/10.1038/s41467-022-31295-3

Xuan, X., Cheng, J., Yang, X., & Zhou, J. (2020). Highly Selective Electrochemical Reduction of CO2 to CH4 over Vacancy–Metal–Nitrogen Sites in an Artificial Photosynthetic Cell. ACS Sustainable Chemistry & Engineering, 8(3), 1679-1686. https://doi.org/10.1021/acssuschemeng.9b07258

Yang, D., Zhu, Q., Chen, C., Liu, H., Liu, Z., Zhao, Z., Zhang, X., Liu, S., & Han, B. (2019). Selective electroreduction of carbon dioxide to methanol on copper selenide nanocatalysts. Nature Communications, 10(1), 677. https://doi.org/10.1038/s41467-019-08653-9

Yang, H., Chuai, H., Meng, Q., Wang, M., Zhang, S., & Ma, X. (2023). Copper-based bimetallic electrocatalysts for CO2 reduction: From mechanism understandings to product regulations. Materials Reports: Energy, 3(1), 100174. https://doi.org/https://doi.org/10.1016/j.matre.2022.100174

Yang, H., Wu, Y., Li, G., Lin, Q., Hu, Q., Zhang, Q., Liu, J., & He, C. (2019). Scalable production of efficient single-atom copper decorated carbon membranes for CO2 electroreduction to methanol. Journal of the American Chemical Society, 141(32), 12717-12723.

Yin, Z., Yu, C., Zhao, Z., Guo, X., Shen, M., Li, N., Muzzio, M., Li, J., Liu, H., Lin, H., Yin, J., Lu, G., Su, D., & Sun, S. (2019). Cu3N Nanocubes for Selective Electrochemical Reduction of CO2 to Ethylene. Nano Letters, 19(12), 8658-8663. https://doi.org/10.1021/acs.nanolett.9b03324

Yu, F., Wei, P., Yang, Y., Chen, Y., Guo, L., & Peng, Z. (2019). Material design at nano and atomic scale for electrocatalytic CO2 reduction. Nano Materials Science, 1(1), 60-69. https://doi.org/https://doi.org/10.1016/j.nanoms.2019.03.006

Zeng, J., Bejtka, K., Ju, W., Castellino, M., Chiodoni, A., Sacco, A., Farkhondehfal, M. A., Hernández, S., Rentsch, D., Battaglia, C., & Pirri, C. F. (2018). Advanced Cu-Sn foam for selectively converting CO2 to CO in aqueous solution. Applied Catalysis B: Environmental, 236, 475-482. https://doi.org/https://doi.org/10.1016/j.apcatb.2018.05.056

Zhang, J., Guo, C., Fang, S., Zhao, X., Li, L., Jiang, H., Liu, Z., Fan, Z., Xu, W., Xiao, J., & Zhong, M. (2023). Accelerating electrochemical CO2 reduction to multi-carbon products via asymmetric intermediate binding at confined nanointerfaces. Nature Communications, 14(1), 1298. https://doi.org/10.1038/s41467-023-36926-x

Zhang, J., Luo, W., & Züttel, A. (2019). Self-supported copper-based gas diffusion electrodes for CO2 electrochemical reduction [10.1039/C9TA06736A]. Journal of Materials Chemistry A, 7(46), 26285-26292. https://doi.org/10.1039/C9TA06736A

Zhang, W., Hu, Y., Ma, L., Zhu, G., Wang, Y., Xue, X., Chen, R., Yang, S., & Jin, Z. (2018). Progress and Perspective of Electrocatalytic CO2 Reduction for Renewable Carbonaceous Fuels and Chemicals. Advanced Science, 5(1), 1700275. https://doi.org/10.1002/advs.201700275

Zhang, W., Huang, C., Xiao, Q., Yu, L., Shuai, L., An, P., Zhang, J., Qiu, M., Ren, Z., & Yu, Y. (2020). Atypical Oxygen-Bearing Copper Boosts Ethylene Selectivity toward Electrocatalytic CO2 Reduction. Journal of the American Chemical Society, 142(26), 11417-11427. https://doi.org/10.1021/jacs.0c01562

Zhang, Z., Huang, X., Chen, Z., Zhu, J., Endrődi, B., Janáky, C., & Deng, D. Membrane Electrode Assembly for Electrocatalytic CO2 Reduction: Principle and Application. Angewandte Chemie, n/a(n/a), e202302789. https://doi.org/10.1002/ange.202302789

Zhang, Z., Huang, X., Chen, Z., Zhu, J., Endrődi, B., Janáky, C., & Deng, D. (2023). Membrane Electrode Assembly for Electrocatalytic CO2 Reduction: Principle and Application. Angewandte Chemie International Edition, 62(28), e202302789. https://doi.org/https://doi.org/10.1002/anie.202302789

Zheng, Y., Vasileff, A., Zhou, X., Jiao, Y., Jaroniec, M., & Qiao, S.-Z. (2019). Understanding the Roadmap for Electrochemical Reduction of CO2 to Multi-Carbon Oxygenates and

Hydrocarbons on Copper-Based Catalysts. Journal of the American Chemical Society, 141(19), 7646-7659. https://doi.org/10.1021/jacs.9b02124

Zhou, Y., Che, F., Liu, M., Zou, C., Liang, Z., De Luna, P., Yuan, H., Li, J., Wang, Z., Xie, H., Li, H., Chen, P., Bladt, E., Quintero-Bermudez, R., Sham, T.-K., Bals, S., Hofkens, J., Sinton, D., Chen, G., & Sargent, E. H. (2018). Dopant-induced electron localization drives CO2 reduction to C2 hydrocarbons. Nature Chemistry, 10(9), 974-980. https://doi.org/10.1038/s41557-018-0092-x

Zhuang, T.-T., Liang, Z.-Q., Seifitokaldani, A., Li, Y., De Luna, P., Burdyny, T., Che, F., Meng, F., Min, Y., Quintero-Bermudez, R., Dinh, C. T., Pang, Y., Zhong, M., Zhang, B., Li, J., Chen, P.-N., Zheng, X.-L., Liang, H., Ge, W.-N., . . . Sargent, E. H. (2018). Steering post-C–C coupling selectivity enables high efficiency electroreduction of carbon dioxide to multi-carbon alcohols. Nature Catalysis, 1(6), 421-428. https://doi.org/10.1038/s41929-018-0084-7

Ziv, N., Mustain, W. E., & Dekel, D. R. (2018). The Effect of Ambient Carbon Dioxide on Anion-Exchange Membrane Fuel Cells. ChemSusChem, 11(7), 1136-1150. https://doi.org/https://doi.org/10.1002/cssc.201702330

VITA

Monsuru Olatunji Dauda was born in Iwo, Osun State, Nigeria, and completed his primary education at Vico Hope Nursery and Primary School in 2008. He then proceeded to A1 Comprehensive Grammar School, also in Iwo, where he graduated in 2014 with distinction, earning the title of best student in Osun State in a competition organized by the Obafemi Awolowo University Student Union Government.

In 2014, Monsuru gained admission into Ladoke Akintola University of Technology (LAUTECH) Ogbomoso, the best state university in Nigeria, where he earned a Bachelor of Technology (B.Tech.) degree in Chemical Engineering with first-class honors. During his undergraduate studies, he acquired a wide range of skills, including gas and liquid phase adsorption, ultraviolet-visible spectroscopy, statistical analysis using SPSS, experimental design using Design-Expert, analytical chemistry techniques, proficiency in MATLAB and Aspen HYSYS and over two years of research experience in wastewater treatment. He was part of a cohort of 120 students and ranked among the top 1% of the class. In recognition of his leadership skills, exceptional academic record, and research contributions, he was named the most innovative leader in Nigeria by the Governor of Nasarawa, Engr. Abdullahi A. Sule, and the most resourceful student of the year by the department of chemical engineering.

Throughout his academic and professional journey, Monsuru has consistently demonstrated his leadership skills. He has held various positions, such as the Vice President of Africa Graduate Students Association, Secretary of the American Chemical Society (ACS), National President of the engineering students' association, and Governor of all interns at ADDAX Petroleum Nigeria Limited. He is also a member of several professional bodies, including ECS, AIChE, ACS, SPE, NSBE, NSE, NSChE, and NISaftyE.

In August 2022, Monsuru joined Louisiana State University (LSU) to pursue his Masters and PhD in Chemical Engineering. His research interests lie in Electrochemical Reduction, Energy Storage, and Electrocatalysis. In his current research, he has developed expertise in advanced characterization techniques such as electrochemical measurements, gas chromatography-mass spectrometry (GC-MS), X-ray diffraction (XRD), X-ray photoelectron spectroscopy (XPS), scanning electron microscopy (SEM), atomic force microscopy (AFM), Fourier-transform infrared spectroscopy (FTIR), Raman spectrometry, and four-point probe measurements. He expects to receive his Master's degree from LSU in August 2024 and PhD in August 2026.

Monsuru is highly organized and maintains a clean workspace and personal records. He is fascinated by the complexity and richness of nature and is passionate about contributing to society in meaningful ways. His guiding principle is to always do his best within the available resources and add value to humanity and any environment he finds himself in. He firmly believes that success is achieved through hard work and a passion for learning, which has earned him the nickname "No Magic in Success" (NMIS).